RMIT UNIVERSITY

Real-time Measurement Corrected Prediction of Soft Tissue Response for Medical Simulations

A thesis submitted in fulfilment of the requirements for the degree of Doctor of Philosophy

Mehran Yarahmadian

M.Sc. Engineering (Biomechanics), IUST

B.Sc. Mechanical Engineering, UT

School of Engineering

College of Science, Engineering and Health

RMIT University

December 2019

Declaration

I certify that except where due acknowledgement has been made, the work is that of the author alone; the work has not been submitted previously, in whole or in part, to qualify for any other academic award; the content of the thesis is the result of work which has been carried out since the official commencement date of the approved research program; any editorial work, paid or unpaid, carried out by a third party is acknowledged; and, ethics procedures and guidelines have been followed.

I acknowledge the support I have received for my research through the provision of an Australian Government Research Training Program Scholarship.

Mehran Yarahmadian

19 December 2019

Acknowledgements

Firstly, I would like to express my sincere gratitude to my supervisor Prof. Peter Dabnichki, for the continuous support of my PhD study and related research, for his patience, motivation, and immense knowledge. His guidance helped me in all the time of research and writing of this thesis. Completion of this work was genuinely impossible without his supervision.

Besides, I would like to thank Dr Toh Yen Pang for his insightful encouragement, and for the meeting discussions, which helped me to widen my research from various perspectives.

My heartfelt thanks also go to my fellow Dr Jaehyun Shin, for his positive attitude and hours spent together on questioning and discussing solutions for this work. Learning from his valuable programming skills besides the BBQs and all the fun we had together in the last four years was motivating enough to keep this work going.

And last but not the least, I would like to thank my siblings, Mahtab and Mehrdad, and my friends, especially Arash Ataee, Reza Omrani, Mona Alizadeh Osgouei, Arash Heidarali, Amir Baf, and Alireza Zabihi who heard me and supported me spiritually throughout my PhD study.

Dedication

For my father, who inspired me.
For my mother, who encouraged me,
and
to my wife, Saeedeh. She never gave up on me.

Table of Contents

DECLARATION II

ACKNOWLEDGEMENTS III

DEDICATION IV

TABLE OF CONTENTS V

LIST OF FIGURES X

LIST OF TABLES XII

LIST OF ABBREVIATIONS XIII

NOMENCLATURE XIV

ABSTRACT 1

1 INTRODUCTION 5

1.1 Medical Simulators 7

1.1.1 Significance 8

1.1.2 Rationale 9

1.2 Research Method 10

1.2.1 Deformation Estimation by KF-FEM 11

1.2.2 Experimental Validation 12

1.2.3 Filter Modification for Uncertain System Inputs 12

1.2.4 Large Nonlinear Deformations 12

2 LITERATURE REVIEW 15

2.1 Deformable Models 17

2.1.1 Heuristic Approach 18

2.1.1.1 Geometrically based models. 18

2.1.1.2 Mass-spring model. 19

2.1.1.3 Linked volumes. 19

2.1.2 Continuum Mechanics Approach 20

2.1.2.1 Finite element method. 20

2.1.2.2 Boundary element methods. 21

2.1.3 Further Modeling Approaches 22

2.1.3.1 Hybrid models. 22

2.1.3.2 Meshless continuum mechanics. 22

2.1.3.3 Machine learning models. 23

2.2 Realistic vs. Interactive Model Challenges 24

2.3 Lack of Real-time Corrective Response 28

2.4 Partially Defined System Inputs 29

2.5 Tissue's Nonlinear Behaviour 30

2.6 Kalman Filter 31

2.7 Aims and Objectives 33

3 DEFORMATION ESTIMATION BY KF-FEM 35

3.1 Method 37

3.1.1 System Equations 37

3.1.2 Finite Element Formulation 39

3.1.3 Implicit Time Integration 41

3.1.4 KF-FEM Algorithm 41

3.1.5 Real-time Approach 42

3.2 Code Structure 42

3.3 Soft tissue deformation estimation by spatio-temporal Kalman filter FE method 43

3.4 Performance Evaluation 43

3.4.1 Simulation Setup 44

3.4.2 Estimates Accuracy 45

3.4.3 Computational Speed 47

3.5 Conclusion 48

4 EXPERIMENTAL VALIDATION 51

4.1 Method 53

4.1.1 Specimen Preparation 54

4.1.2 Test Setup 55

4.2 Experiment Results 56

4.2.1 Computational Performance 58

4.2.2 Estimates Accuracy 59

4.3 Real-life Application 60

4.4 Conclusion 62

5 MODIFIED ALGORITHM FOR UNCERTAIN SYSTEM INPUTS 63

5.1 Method 66

5.2 Application in Soft Tissue Deformation 68

5.2.1 FEM Formulation for the UNC$_I$.KF-FEM 69

5.2.2 The Modified Algorithm 70

5.3 Performance Evaluation and Comparison 71

5.3.1 Initial Error Recognition 72

5.3.2 Simulation Results 73

5.3.2.1 Computation speed. 73

5.3.2.2 Deformation accuracy. 74

5.4 Conclusion 75

6 LARGE NONLINEAR DEFORMATIONS 77

6.1 Total Lagrangian Explicit Dynamics 79

6.1.1 Displacement-based Framework 80

6.1.2 Finite Element Solution 81

6.1.3 Time Integration 82

6.1.4 Element Nodal Forces 83

6.1.4.1 The strain-displacement matrix. 83

6.1.4.2 Stress tensor. 84

6.2 Modified Solver for Nonlinear Deformation 85

6.2.1 State Equations 85

6.2.2 Modified Algorithm 86

6.3 Performance Evaluation 86

6.3.1 Estimates Accuracy 88

6.3.2 Computational performance 90

6.4 Real-time Implementation 90

6.4.1 Geometry Structure 90

6.4.2 Arrays Structure 92

6.5 Conclusion 93

7 CONCLUSION 95

7.1 Computational Speed vs. Accuracy 97

7.2 Analytical Model Inaccuracy 98

7.3 System Input Uncertainty 98

7.4 Large Nonlinear Deformations 99

7.5 Contributions 99

7.6 Future Work 100

PUBLICATIONS 101

REFERENCES 102

APPENDIX A 109

APPENDIX B 110

APPENDIX C 119

List of Figures

FIGURE 1-1. INTERACTION OF THE THREE GENERATIONS OF MEDICAL SIMULATORS 8

FIGURE 1-2. A SCHEMATIC OF MEDICAL SIMULATION SYSTEMS 10

FIGURE 1-3. THE RESEARCH STRATEGY 11

FIGURE 1-4. THE SCOPE AND OUTLINE OF THE THESIS 13

FIGURE 2-1. GEOMETY-BASED MODELS: (A) A FREE-FORM DEFORMED VOLUME WITH CONTROL POINTS SEDERBERG AND PARRY (1986) (B) A DEFORMED SURFACE WITH DEFORMED SPLINES COVER ET AL. (1993) 18

FIGURE 2-2. ITERATIVE PROCESS OF CALCULATING GRAVITY FORCES EXERTED ON MESH SPRINGS (MSM) (PATETE ET AL., 2013) 19

FIGURE 2-3. LINKED VOLUMES: (A) A DEFORMED OBJECT WITH BASIC LINKED VOLUMES (JANSSON & VERGEEST, 2002) (B) CHAINMAIL PROCESS (JINAO ET AL., 2018) 20

FIGURE 2-4. TRIANGULAR MESH USED FOR COLLISION DETECTION IN CARDIOVASCULAR NAVIGATION (TALBOT ET AL., 2017) 21

FIGURE 2-5. KALMAN FILTER RECURSIVE ALGORITHM 32

FIGURE 3-1. THE KF-FEM ALGORITHM 43

FIGURE 3-2. THE PROPOSED KF-FEM CODE STRUCTURE 44

FIGURE 3-3. BOUNDARY CONDITIONS – MESH 2 (FIXED NODES ARE MARKED WITH BLUE) 45

FIGURE 3-4. DISPLACEMENT AT THE OBSERVATION POINT FROM KF-FEM VS. FEM (LEFT), AND THE NORMALIZED ERROR PERCENTAGE OF ESTIMATES COMPARED TO THE MEASUREMENT (RIGHT) – MESH 2 46

FIGURE 3-5. THE REDUCED ERROR FROM MEASUREMENTS (PERCENT) WITH KF-FEM – MESH 2 46

FIGURE 3-6. THE ABSOLUTE ERROR OF KF-FEM ESTIMATES VS. MEASUREMENTS – MESH 2 47

FIGURE 3-7. DEFORMED LIVER MODEL FROM THE FEM (ABAQUS, LEFT) AND THE KF-FEM (MATLAB, RIGHT) – MESH 2 48

FIGURE 4-1. FORCE-DISPLACEMENT MEASUREMENTS FROM THE INDENTATION TEST ON TEN SILICONE SAMPLES . 55

FIGURE 4-2. THE KF-FEM VS. FEM RESPONSE IN COMPARISON WITH THE MEASUREMENTS (SAMPLES 1 AND 2) . 56

FIGURE 4-3. THE KF-FEM VS. FEM RESPONSE IN COMPARISON WITH THE MEASUREMENTS (SAMPLES 3 AND 4) . 57

FIGURE 4-4. THE KF-FEM VS. FEM RESPONSE IN COMPARISON WITH THE MEASUREMENTS (SAMPLES 5 AND 6) . 57

FIGURE 4-5. THE KF-FEM VS. FEM RESPONSE IN COMPARISON WITH THE MEASUREMENTS (SAMPLES 7 AND 8) . 57

FIGURE 4-6. THE KF-FEM VS. FEM RESPONSE IN COMPARISON WITH THE MEASUREMENTS (SAMPLES 9 AND 10) 58

FIGURE 4-7. THE UNC_M.KF-FEM VS. MEASUREMENT MEDIAN DISPLACEMENT FROM TEN SAMPLES IN COMPARISON WITH THE FE MODEL 60
FIGURE 4-8. DISPLACEMENT FROM THE UNCERTAIN FEM AND KF-FEM AGAINST EXPERIMENTS 61
FIGURE 5-1. THE UNC_I.KF-FEM ALGORITHM VS. THE KF-FEM 66
FIGURE 5-2. THE UNC_I.KF-FEM OFFLINE STAGE 71
FIGURE 5-3. THE UNC_I.KF-FEM REAL-TIME STAGE 72
FIGURE 5-4. INITIALISATION OF THE MEASUREMENT ERROR COVARIANCE 73
FIGURE 5-5. COMPARING DISPLACEMENT VALUES FROM THE DEVELOPED KF-FEM AND ITS MODIFIED ALGORITHM WITH THE FEM 74
FIGURE 6-1. THE NL_{TL}.KF-FEM FOR LARGE NONLINEAR DEFORMATIONS 86
FIGURE 6-2. DISPLACEMENT MEASUREMENT AT THE OBSERVATION POINT 87
FIGURE 6-3. THE SIMULATED MODEL; (A) UNDEFORMED, (B) DEFORMED 88
FIGURE 6-4. THE NL_{TL}.KF-FEM ESTIMATES VS. THE REFERENCE FEM AND MEASUREMENTS AT THE OBSERVATION POINT 88
FIGURE 6-5. THE NL KF-FEM ESTIMATES VS. THE REFERENCE FEM IN A RANDOM POINT 89
FIGURE 6-6. SAMPLES FROM THE MESH NODES COORDINATES AND THE ELEMENTS CONNECTIVITY LIST 90
FIGURE 6-7. SAMPLES FROM THE NODES MAPPING ARRAY 91
FIGURE 6-8. MESH MAPPING STRUCTURE 91
FIGURE 6-9. A SCHEMATIC OF THE STRUCTURE DEVELOPED FOR PARALLEL CALCULATION OF ELEMENTS NODAL FORCES 92
FIGURE A-1. THE BINARY MEASUREMENT MATRIX ADDRESSING OBSERVATION POINTS IN THE STATE VECTOR .. 109

List of Tables

TABLE 2-1. THE PARAMETERS GOVERNING BIOLOGICAL ORGANS DEFORMATION 17

TABLE 2-2. COMPARISON OF DEFORMABLE MODELS 24

TABLE 2-3. COMPUTATIONAL PERFORMANCE OF DEFORMABLE MODELS 28

TABLE 3-1. THE LIVER MODEL MESH PROPERTIES 45

TABLE 3-2. THE COMPUTATIONAL CPU TIME AND THE UPDATE FREQUENCY 47

TABLE 4-1. COMPUTATIONAL PERFORMANCE OF THE UNC_M.KF-FEM VS. THE FEM 59

TABLE 4-2. RMSE (MM) OF KF-FEM VS. FEM AGAINST MEASUREMENTS AT THE INDENTER'S TIP 59

TABLE 4-3. RMSE (MM) OF THE UNC_M.KF-FEM AND FEM WITH WRONG ELASTICITY AGAINST MEASUREMENTS 61

TABLE 5-1. THE MODELS NORMALIZED ERROR [%] STANDARD DEVIATION 75

TABLE 6-1. THE ESTIMATES MAE IN COMPARISON WITH THE FEM 89

List of Abbreviations

2D	2-Dimensional
3D	3-Dimensional
ANN	Artificial Neural Network
BEM	Boundary Element Method
CPU	Central Processing Unit
CT	Computerized Tomography
DVF	Deformation Vector Field
FE	Finite Element
FEM	Finite Element Method
FFD	Free-Form Deformation
GPU	Graphics Processing Unit
I/O	Input/Output
KF	Kalman Filter
KF-FEM	Kalman Filter Finite Element Method
LMM	Lump Mass Matrix
MAE	Mean Absolute Error
MJED	Multiplicative Jacobian Energy Decomposition
ML	Machine Learning
MRI	Magnetic Resonance Imaging
MSE	Mean-Square Error
MSM	Mass-Spring Model
MTLED	Meshless Total Lagrangian Explicit Dynamics
NL_{TL}.KF-FEM	Nonlinear Total Lagrangian KF-FEM
PC	Personal Computer
PCISPH	Predictive-Corrective Incompressible SPH
PCMFS	Point-collocation-based Method of Finite Spheres
PDE	Partial Differential Equation
PDMS	Polydimethylsiloxane
PTCD	Percutaneous Transhepatic Cholangio-Drainage
RMSE	Root-Mean-Square Error
RPIM	Radial Point Interpolation Method
SEDF	Strain Energy Density Function
SPH	Smoothed Particle Hydrodynamics
STS	Soft Tissue Sarcoma
SVR	Support Vector Regression
TLED	Total Lagrangian Explicit Dynamics
TMM	Tensor Mass Model
TURP	Transurethral Resection of the Prostate
UNC_I.KF-FEM	Uncertain Input KF-FEM
UNC_M.KF-FEM	Uncertain Model KF-FEM

Nomenclature

Latin:

Δt	Time increment
Δt_{cr}	Critical time increment
Ω	Geometrical body domain
β	Newmark coefficient
δ_{ij}	Kronecker delta function
λ	Newmark coefficient / Lamé constant
μ	Lamé constant
ν	Poisson's ratio
ρ	Mass density
${}^{0}\partial H_x$	Element shape function spatial derivatives matrix
$\boldsymbol{\sigma}$	Cauchy stress tensor

English:

$\boldsymbol{A}_k^{kf}$	UNC_I model modified state transition matrix
$\boldsymbol{B}$	Strain-displacement matrix
$\boldsymbol{B}_k^{kf}$	UNC_I model modified input matrix
$\boldsymbol{C}$	Rayleigh damping matrix
$\boldsymbol{C}_k^{kf}$	UNC_I model optimal state matrix
${}_0^t\boldsymbol{C}$	Right Cauchy-Green deformation tensor
$\boldsymbol{D}$	Material matrix
$\boldsymbol{D}_k^{kf}$	UNC_I model optimal state input matrix
E	Elasticity modulus
$\boldsymbol{F}$	State transition matrix
${}^{t}\boldsymbol{F}^{(e)}$	Global nodal force in element e
$\boldsymbol{G}$	System input matrix
$\boldsymbol{H}$	Measurement matrix
$\boldsymbol{I}$	Identity tensor
J	Jacobian determinant
$\boldsymbol{K}$	Stiffness matrix
$\boldsymbol{K}_k$	Kalman gain
L_e	Mesh element smallest characteristic length
$\boldsymbol{M}$	Mass matrix
N_a	Mesh element's shape function at node a
P_k^-, P_k^+	*priori* and *posteriori* estimation error covariance
$\boldsymbol{Q}$	System error covariance matrix
$\boldsymbol{R}$	Measurement error covariance matrix
$\boldsymbol{S}$	System/Measurement joint error covariance matrix
${}_0^t\boldsymbol{S}$	Second Piola-Kirchhoff stress tensor
V	Mesh element's volume

$V_{\tilde{y}}$	UNC_I model measurement error covariance matrix
$V_{\tilde{z}}$	UNC_I model input error covariance matrix
${}^{t}_{0}\boldsymbol{X}_{ij}$	Deformation gradient tensor
$\boldsymbol{b}$	Vector of body forces
c	Dilatational wave speed of the material
c_1, c_2	Rayleigh damping coefficients
d_{mi}	Displacement of node m along the axis i
e_N	Normalised error
$\boldsymbol{f}_a^e$	External force at node a of element e
h_a	Spatial derivative of element's shape function at node a
$\boldsymbol{r}$	Vector of external loads
t_k	Time at time point k
$\boldsymbol{u}$	Nodal displacement
$\dot{\boldsymbol{u}}$	Nodal velocity
$\ddot{\boldsymbol{u}}$	Nodal acceleration
${}^{t}\boldsymbol{u}$	Global displacement vector at time t
$\boldsymbol{v}$	Measurement error (noise)
v_1	UNC_I model system noise
v_2	UNC_I model measurement noise
w	System error
$\boldsymbol{w}_k^m$	UNC_I model modified input vector (measured)
x, y, z	Global coordinate axes
$\boldsymbol{x}_k$	System state vector (discrete-time dynamic target variable)
$\hat{\boldsymbol{x}}_k$	Optimal state estimate
$\hat{\boldsymbol{x}}_k^-, \hat{\boldsymbol{x}}_k^+$	State *priori* and *posteriori* estimate
${}^{t}x$	Global Cartesian point coordinate at time t
$\boldsymbol{y}_k$	Measurement vector (actual)
$\hat{\boldsymbol{y}}_k$	Optimal output estimate
$\tilde{y}_k$	UNC_I model measurement error
y_k^m	UNC_I model measurement (measured)
$\boldsymbol{z}_k$	System input vector (actual)
$\hat{\boldsymbol{z}}_k$	Optimal input estimate
$\tilde{z}_k$	UNC_I model input error
z_k^m	UNC_I model input (measured)

Script:

$\mathcal{m}_k$	UNC_I model optimal input coefficient
$\boldsymbol{\mathcal{p}}_k$	UNC_I model modified state
$\mathcal{s}_k$	UNC_I model optimal input coefficient

Double-struck:

$\mathbb{A}, \mathbb{B}, \mathbb{C}, \mathbb{D}$	UNC_I system coefficients

INTENTIONALLY LEFT BLANK

Abstract

Medical simulators, such as in palpation and disease diagnosis, require an efficient model of the biological soft tissue deformation. Hence, a computationally fast and accurate algorithm is required to support and enhance user interactions in near real-time simulations. The visual accuracy of such simulators is dependent on the user's reaction time. Static visual images that update at a rate of 25 Hz are perceived as real-time moving images. Hence, visualizing software requires fast algorithms to compute the deformation of soft tissue to facilitate a meaningful simulation. Furthermore, soft tissue behaviour should be modelled accurately while compatible with real-time computation.

This work proposes a fast solver for the linearized finite element method (FEM) and validates the proposed algorithm with experimental results. The novelty of the method lies in the utilization of real-time force/displacement measurements that are embedded in the solution via the Kalman filter.

A novel computational algorithm that utilizes the strength of the FEM in terms of accuracy and employs direct measurements from the manipulated tissue to overcome the slow computational process of the FEM is proposed in the first part of the thesis. As the behaviour of the mechanically loaded tissue can be regarded as linearly responding at each time step, a constant acceleration temporal discretization method, i.e., the Newmark-β is employed. In real-time applications, the accuracy of the target variable highly depends on the accuracy of the inputs while differentiating noise from the signal is hardly ever possible. To address this problem, a Kalman filter-based method is developed. The proposed algorithm not only filters the noise from the measurements but also adapts the filter gain to the estimates of the target variable, i.e., the resulting tissue deformation. For a simulated tension test of a cubic model, the proposed algorithm achieves the update frequency of 63.3 Hz. This rate is a significant improvement in computational speed compared to the 5.8 Hz update rate by the classic FEM.

Besides, this novel combination of the KF and the FEM makes it possible to expand the displacement estimates in the spatial domain when the measurements are only partially available at certain points.

The performance of the above method is validated experimentally through a comparison with indentation tests on artificial human tissue-like material and with the FEM result under identical simulation conditions. The test is repeated on several samples, and the displacement variation from the FEM outcome is considered as the model error. Simulation results show that the proposed method achieves the deformation update frequency of 145.7 Hz compared to the 2.7 Hz from the reference FEM. The proposed method shows the same predictive ability, only 0.47% difference from FEM on average. Experimental validation of the proposed KF-FEM confirms that by consideration of both the measurement noise and the model error, the proposed method is capable of achieving high-frequency response without sacrificing the accuracy. Further to this, the experiments confirmed the linearized model response is reliable within the applied displacement range and therefore proving that KF can be employed.

The developed KF-FEM was modified in the next study to address the problem resulting from inaccurate external loads measurements by the force sensors. In the modified version, both the external force, i.e., driving variable, and the displacement, i.e., driven variable, are taken as system states. It is considered that the uncertainty of the model input influences the accuracy of the system estimates. The modified model is calibrated to differentiate the system noise from the input noise. Numerical simulations were conducted on a liver shape geometrical model, and the simulation results demonstrate that more than 90% of the measurement noise is removed. The computational speed is also increased, delivering up to 89 Hz update rate. While the uncertainty of the external load is replicated in the displacements in

an FEM solution, the developed algorithm can differentiate the measurement noise, including the displacement and external forces, from the system error, i.e., the FE model error.

In the last study, the proposed model was developed to reflect the nonlinear behaviour of the manipulated tissue. The Central Difference time discretization method was used to model large deformations. A novel feature is that the Equation of motion is formulated within the element level rather than in the global spatial domain. This approach helped to improve the computational speed. Indentation with strains of slightly over 10% was simulated to assess the performance of the proposed model. The developed algorithm achieved the 33.85 Hz update frequency on a standard-issue PC and confirmed its suitability for real-time applications. Also, the proposed model achieved estimates with a maximum 5.75% mean absolute error (MAE) concerning the measurements while the classic FEM showed 6.20% MAE under identical simulation condition. Results confirm that deformation estimates for noisy boundary loads of the FEM can be improved with the help of direct measurements and yet be realistic in terms of real-time visual update.

This study proposed a novel computational algorithm that achieved update frequencies of higher than 25 Hz to be perceived as real-time in human's eyes. The developed KF-FEM model has also shown the potential of improving the FEM accuracy with the help of direct measurements. The proposed algorithm used partially available measurements and expanded its estimates in the spatial domain. The method was experimentally validated, and the model input uncertainty, as well as the nonlinear behaviour of the soft tissue, were assessed and verified.

INTENTIONALLY LEFT BLANK

CHAPTER 1

INTRODUCTION

INTENTIONALLY LEFT BLANK

1 Introduction

1.1 Medical Simulators

During the past three decades, the simulation of medical procedures has built an extreme interest between mechanical and computer science researchers. Satava (1996) categorized medical simulators into three generations. The first generation simulates the geometrical nature of the human tissues and organs and provides the three-dimensional environment to navigate and study the anatomy of target living beings. In spite of their imperfect user interfaces, the first-generation simulators have found their role enormously in many educational and training applications. The second generation addresses the physical interaction of body organs. For soft tissues, they are capable to simulate the deformation of tissues when interact with surgical tools and surrounding organs. For hard tissues, these simulators are capable to simulate the kinematics of the structures. The third generation of simulators studies physiology and functional nature of human organs. To exemplify, a physical phenomenon like cutting a vessel can affect the blood pressure and therefore, the function of other organs; or, a physiological fact such as the development of tumorous lesions may modify the tissue mechanical properties locally. Figure 1-1 shows the three generations of medical simulators and how the different levels of simulation in terms of anatomy, physics, and physiology interact with each other.

A medical simulator consists of input and output devices, and the core of the simulator. The input devices include a force-sensor-equipped device with which a user moves the surgery tools, and a mouse to have a good view of the operation zone. The core of the simulator is to create and analyse the geometrical, the physical, and the physiological model of living beings. Medical images are obtained from CT scans and MRIs, then converted to standard 3D graphics

formats to form the geometrical models. Physical and physiological models are tissue-specific and depend on the mechanical properties of the target tissue. The collision between surgical tools and soft tissue is detected, and the corresponding reaction forces on the instruments are calculated in the core of the simulator. The computed data is sent to the output devices, which consist of a screen and the haptic device. The haptic device transforms reaction forces and moments to the user and allows the user to have a sense and perception of virtual contact with the tissue (Niroomandi, Alfaro, Cueto, & Chinesta, 2012).

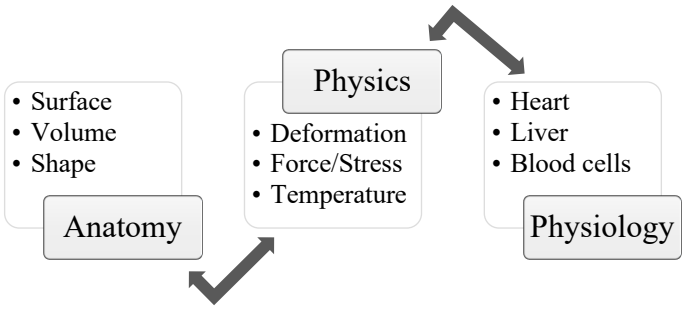

Figure 1-1. Interaction of the three generations of medical simulators

In spite of the rapid development in computer simulation technologies, achieving accurate soft tissue simulation remains challenging. Notably, medical applications require computationally fast and reliable models to adapt user interactions (Wen & Tao Ruan, 2014). It will be elaborated in this project that an efficient and accurate simulation of biological soft tissues is the crucial computational component in medical simulators.

1.1.1 Significance

There are four overall gained values by the use of medical simulators as a component of medical training: patient safety, ongoing training opportunities, enhanced educational experience, and cost-efficiency. Medical simulators provide a safe environment in which a physician can repeatedly practice a procedure without putting patient at risk. The simulator is generally available and easily accessible by the trainees so that trainees can use it whenever they have the time. The training procedures are, therefore, not dependent on the availability of

an actual patient, and trainees can practise on the simulator until they feel they have comprehended the essential operational skills (Kunkler, 2006).

1.1.2 Rationale

The visual accuracy of simulation-based training is dependent on the reaction time in the human sensory system. Static visual images that are updated at the rate of 25 Hz "appear" real. Therefore, the challenge is to develop computational algorithms that allow such rapid computations without improperly sacrificing computational accuracy (Courtecuisse et al., 2014; Lim & De, 2007). The development of such fast algorithms to compute the deformation in quasi real-time mode is likely to benefit numerous medical applications. More specifically, when considering requirements for realistic interactive simulations of medical procedures, several elements seem mandatory

- anatomical models and tissue properties need to be patient-specific and obtained without complicated additional process
- soft tissue response needs to be realistic and demonstrate a predictive capability, yet it should be compatible with real-time computation
- interactions with the surrounding anatomy and with medical devices need to involve advanced contact models that can be computed in real-time
- and finally, realistic visual and haptic feedback should be provided to create a higher level of reality, in particular, during training sessions (Courtecuisse et al., 2010).

In such a system, the users would be able to interact with the three-dimensional virtual models of organs using their sense of vision as well as manipulating them actively using their sense of touch through a haptic interface device. Figure 1-2 shows a schematic of the medical simulation systems.

A useful medical simulator must be able to reproduce the mechanical behaviour of organs. For this purpose, the modelling of tissue deformation is of considerable significance,

and several models of different approaches have been reported. There are two broad methods of studying soft tissue deformation. First, the nonphysical strategies, i.e. the strategies that do not follow physics laws, are fast in computations but less realistic (for instance, see (Patete et al., 2013)). Second, the physics-based ones, that are more realistic, but the computation is slow (see for example (Taylor, Cheng, & Ourselin, 2008; Wu, Westermann, & Dick, 2015)). However, the simulation of practical medical procedures requires the knowledge of the mechanical properties and physical behaviour of tissues and organs. In addition to that, to set up a real-time interactive digital environment, models of tissues and organs should be computed and updated in real-time. As a result, the simulation of soft tissue behaviours such as deformation requires specialized optimized algorithms which have to comply both with the accuracy of results and computation time. For these reasons, research in the field of real-time deformable tissues remains very open.

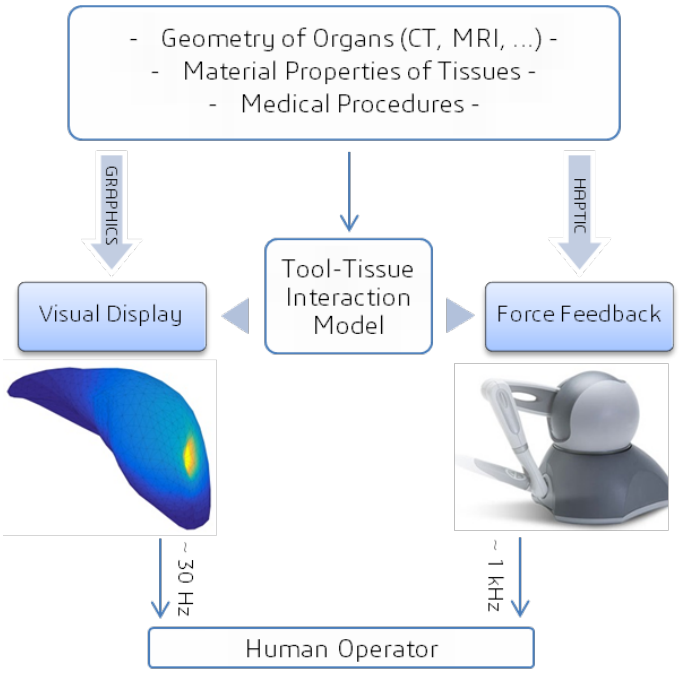

Figure 1-2. A schematic of medical simulation systems

1.2 Research Method

After thorough research and review of the significance of the soft tissue's deformation simulation in medical applications, and careful identification of the gaps in the current state of

the art, as further will be presented in chapter 2, the research strategy is prepared in four stages. Figure 1-3 shows a schematic of the steps taken in this work.

The project focuses firstly on Kalman filtering methods to gain an optimal state estimation of tissue behaviour in real-time. Secondly, on finite element methods which are shown to be a promising approach to extend the estimation accuracy in space directions. Experiments are conducted to validate the feasibility of the algorithm. The developed method is modified to address the uncertainties of the simulation inputs. Finally, large nonlinear deformations of the soft tissue are studied.

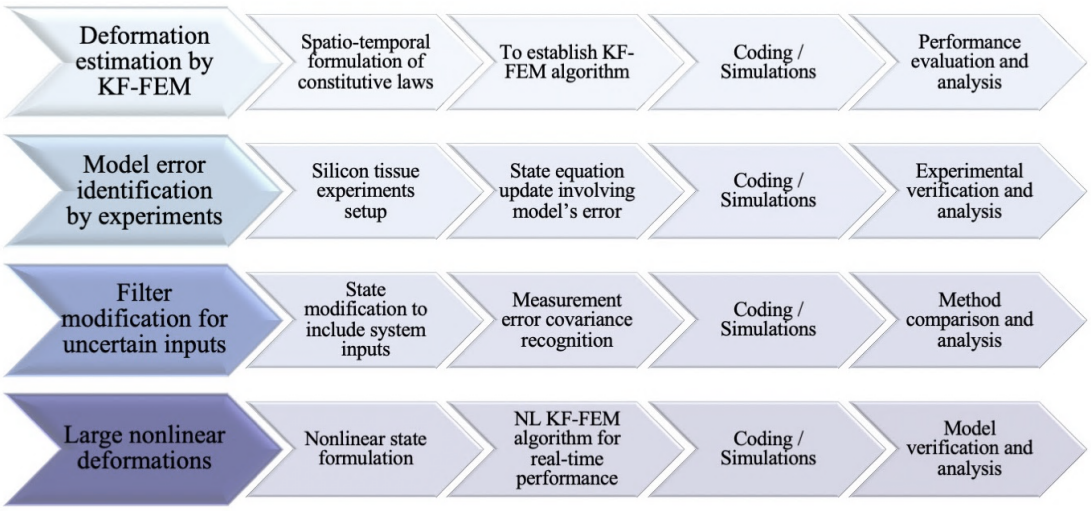

Figure 1-3. The research strategy

1.2.1 Deformation Estimation by KF-FEM

Different variations of finite element formulation such as different spatial and temporal discretisation and boundary conditions influence the speed of calculations and accuracy of outcomes. Besides, the solver (for instance, KF) hypothesis and scope of work can also affect the accuracy and computational performance of the physical model. Therefore, proper programming of the physical model is crucial for understanding the effect of our method on the performance of tissue real-time behaviour estimation. The steps below are taken into consideration in this work to achieve an optimised estimator for the soft tissue's deformation in a realistically and interactively.

- The spatio-temporal formulation of the algorithm to be developed
- The target tissue's geometry, material properties, and the simulation boundary conditions to be investigated and defined in the code
- The measurement data to be generated and employed by the algorithm
- The algorithm's real-time performance to be monitored and plotted
- The simulation's accuracy and computational speed to be assessed

1.2.2 Experimental Validation

Experiments on the Silicon tissue will be set up to validate the accuracy of the proposed method. The purpose is to verify that the linearized FEM is reliable within the range of applied displacement. Besides, the computational speed is monitored.

1.2.3 Filter Modification for Uncertain System Inputs

The measurement data contain variable noise levels due to various parameters, instruments' accuracy and data update frequency to name but two. Such random factors result in providing unknown noisy input for the system. This project modifies the developed algorithm to consider and eliminate measurement tools noise such as in force sensors. The proposed method is modified to differentiate the mathematical model error from the force-displacement measurement noise.

1.2.4 Large Nonlinear Deformations

Material and geometry nonlinearity of soft tissue is incorporated into the proposed method to obtain a high degree of realism. The performance of the algorithm is assessed in terms of accuracy and computational speed.

The scope and outline of the thesis is defined according to sections 1.2.1 to 1.2.4, and the thesis structure is illustrated in Figure 1-4.

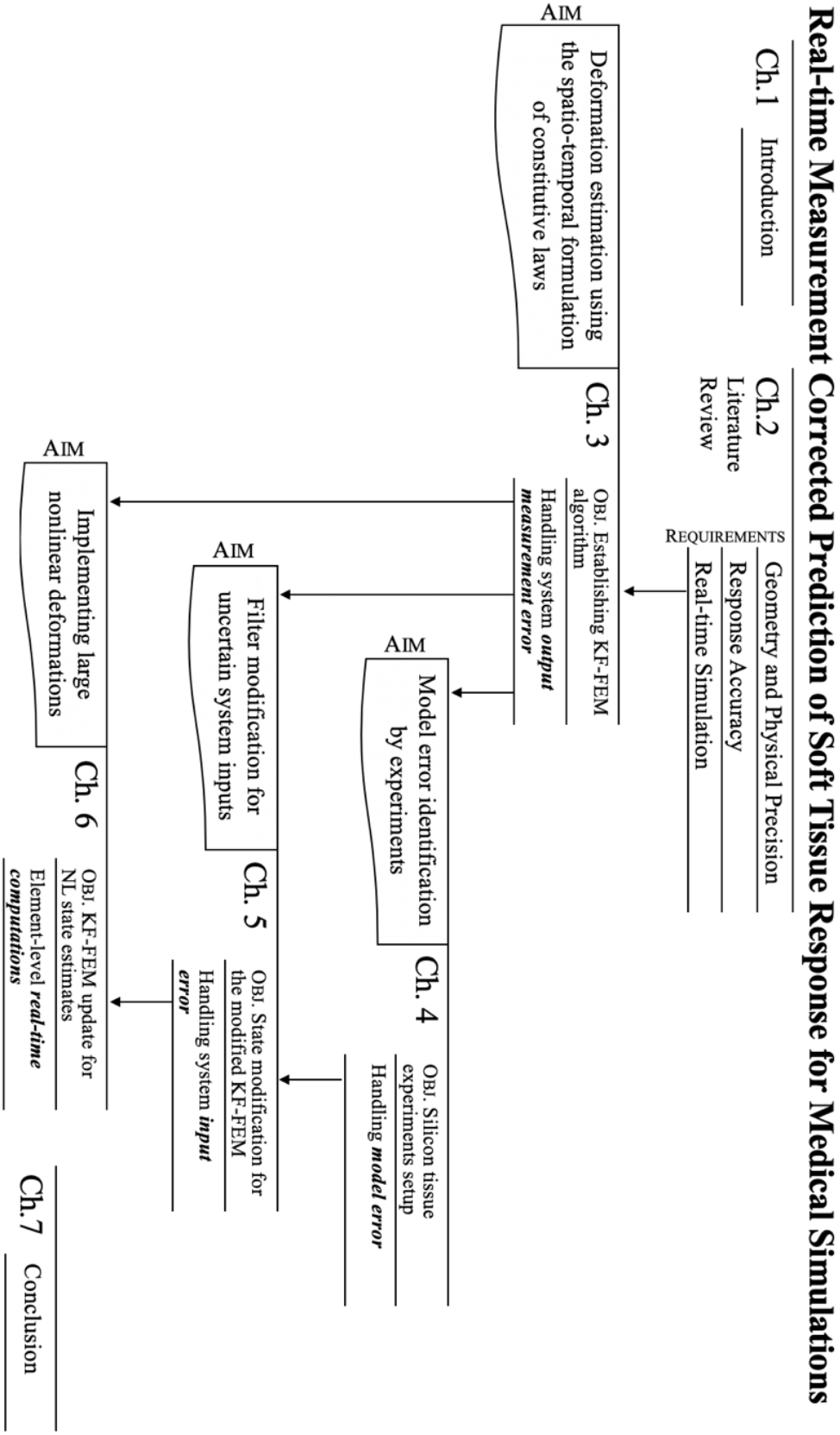

Figure 1-4. The scope and outline of the thesis

INTENTIONALLY LEFT BLANK

CHAPTER 2

LITERATURE REVIEW

INTENTIONALLY LEFT BLANK

2 Literature Review

The deformation of biological organs in interaction with manipulating and operational instrument is mainly governed by three factors

1. Organ geometry,
2. Tissue's constitutive laws, and
3. Boundary conditions due to the tissue's surrounding structure.

Modelling the above and obtaining reliable predictive results to meet the requirements of target application has been a longstanding challenge for the researcher. Table 2-1 shows some common factors discussed in the literature. Misra, Macura, Ramesh, and Okamura (2009) studied the effect of some combinations of the mentioned parameters in the fidelity and efficiency of medical simulators and planners.

Table 2-1. The parameters governing biological organs deformation

Geometry	Square	Circle
Material Properties	Linear elastic	Hyperelastic
Boundary Conditions	Fixed edge	Partially constrained

2.1 Deformable Models

The multidisciplinary field of modelling biological soft tissue's behaviour has been of strong interest for researchers from biomedical engineering, computational physics, and computer graphics. Novel methods have been proposed to address the difficulties of developing high fidelity simulation of deformable models in medical applications.

Deformable models are broadly classified into two categories: physics-based (Nealen, Müller, Keiser, Boxerman, & Carlson, 2006) and heuristic models. Physics-based models are primarily using continuum mechanics and solve the incurring partial differential equations

(PDEs) using numerical methods. Non-physical models use intuitive methods, and they are also known as heuristic models (Meier, López, Monserrat, Juan, & Alcañiz, 2005).

2.1.1 Heuristic Approach

Heuristic models are based on the hypothesis that the exact computational approach of continuum mechanics is far too sophisticated and complicated for realistic real-time performances.

2.1.1.1 Geometrically based models.

Since visual deformation and haptic feedbacks are limited to the surface, geometry-based models were developed to simulate the surface deformation more than three decades ago. Sederberg and Parry (1986) developed a free-form deformation (FFD) algorithm to deform the surface through the free manipulation of control points. Cover et al. (1993) employed deformable splines to study the manipulation of the gall bladder in laparoscopic surgery. Geometrically based models are often fast for illustrating interactive deformation, but they do not closely resemble the underlying physical behaviour of the soft tissue deformation. Figure 2-1 shows a deformed volume and surface obtained by FFD and deformable splines models respectively.

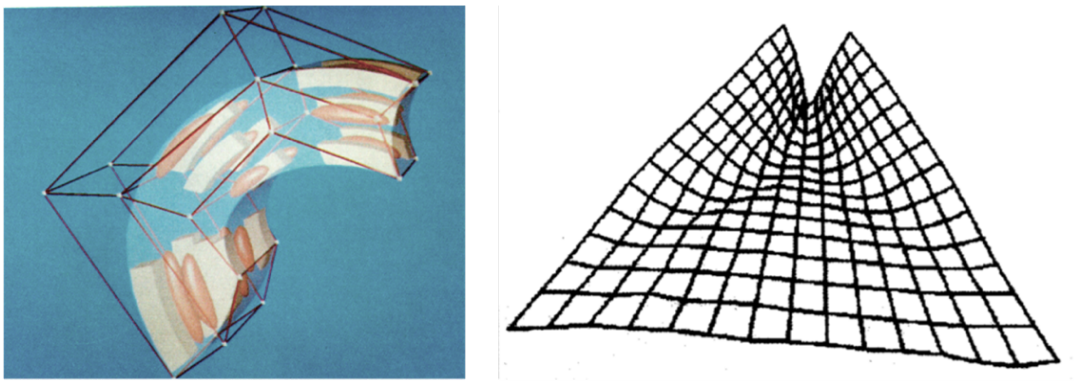

Figure 2-1. Geomety-based models: (a) A free-form deformed volume with control points Sederberg and Parry (1986) (b) A deformed surface with deformed splines Cover et al. (1993)

2.1.1.2 Mass-spring model.

The mass-spring model (MSM) is a widely applied method in modelling deformable objects, that is based on the principle of dynamics. Kühnapfel, Çakmak, and Maaß (2000) modelled an elastic 3D mesh of virtual mass points which were interconnected by virtual springs with damping elements in their endoscopic surgery training simulator. The MSM has been used in various kinds of training simulators such as in transurethral resection of the prostate (TURP) (Castaneda & Cosio, 2004) and heart valve repair procedure (Hammer, Sacks, Del Nido, & Howe, 2011). Figure 2-2 shows the iterative process of calculating forces exerted on masses attached to a mesh of springs.

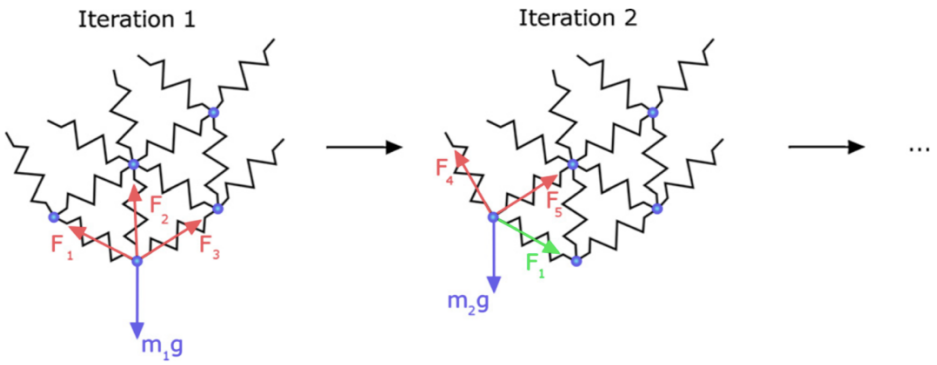

Figure 2-2. Iterative process of calculating gravity forces exerted on mesh springs (MSM) (Patete et al., 2013)

The MSM easy implementation has made them suitable for the dynamic simulation of complex behaviours, particularly in multi-organ systems. Topographical changes such as resection, cutting, and suturing are simply achievable during the simulation by adding or removing connections between vertices. With no specific requirements to high levels of code parallelization, the MSM model can compute high refresh rates for real-time applications (C. Li, Ding, Hong, Pan, & Liu, 2018; Patete et al., 2013).

2.1.1.3 *Linked volumes.*

The basic version of linked volume models is a 3D extension of MSM. The entire volume is discretized into cubic elements with virtual masses located at the centre of elements and connected to neighbouring elements through springs and dampers (Jansson & Vergeest,

2002). Similar to the basic linked volume, the ChainMail algorithm discretizes the geometrical domain into volumetric elements but connected through chain-like links rather than springs and dampers. The chain elements can move freely, within a certain limit, without influencing neighbouring elements. In the ChainMail model, forces are not associated to the element links, and displacements are obtained through minimizing the internal deformational energy iteratively until convergence is achieved (Rodríguez, León, & Arroyo, 2016; Villard et al., 2014). Figure 2-3 shows deformation with a basic and a ChainMail linked volume model.

In summary, heuristic deformable models are easy to implement, fast and flexible to topographical change but they do not offer a clear relationship between model parameters and material constitutive laws. The model's physical accuracy requires complex optimization techniques to suit the specific modelled geometry (Jinao, Yongmin, & Chengfan, 2018).

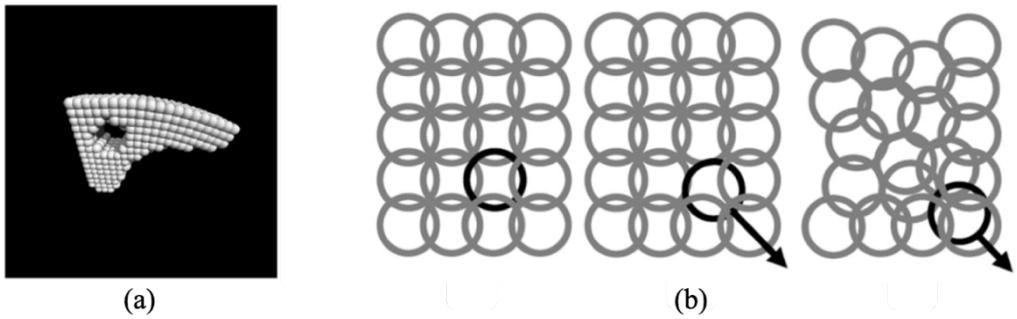

Figure 2-3. Linked volumes: (a) A deformed object with basic linked volumes (Jansson & Vergeest, 2002) (b) ChainMail process (Jinao et al., 2018)

2.1.2 Continuum Mechanics Approach

Opposite to the discrete models championed by the heuristic approaches, continuum mechanics approach considers the target domain as a continuous medium composed of connected volumes. The methods in this group employ constitutive laws to govern the loading response of a body.

2.1.2.1 Finite element method.

The finite element method (FEM) has been the preferred method in computational biomechanics due to its physical accuracy (Freutel, Schmidt, Dürselen, Ignatius, & Galbusera,

2014). The FEM has been used in a variety of biomechanical applications such as cardiac electrophysiology for training simulators (Talbot et al., 2017), development of patient-specific models for hepatic surgery (M. Li et al., 2015; Plantefeve, Peterlik, Haouchine, & Cotin, 2016), and high-speed brain deformations with haptic feedback (Joldes, Wittek, & Miller, 2009).

The FEM divides the analysed material domain into a finite number of elements, and the constitutive laws are approximated and satisfied at element level. By assembling all the mesh elements into a global formulation, the mechanical behaviour of the entire soft tissue is represented. A triangular surface mesh of the cardiovascular system is illustrated in Figure 2-4.

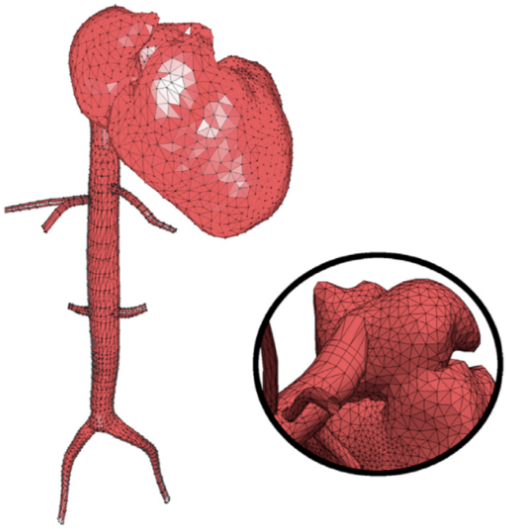

Figure 2-4. Triangular mesh used for collision detection in cardiovascular navigation (Talbot et al., 2017)

2.1.2.2 Boundary element methods.

BEM is a physics-based method that computes the deformation by numerically solving the integral boundary equation on a surface mesh. The computational efficiency of the BEM is high as the simulation is only on boundaries and no computation resource is wasted in updating the volume. BEM is also used in virtual surgery to model the deformation of organs. Kim, Choi, De, and Srinivasan (2007) developed a multi-resolution modelling technique with local surface mesh subdivision to enhance the accuracy of contact areas in surgical simulation without losing real-time interactivity. Wang et al. (2007) used BEM in the simulation of three main surgical applications of prodding, pinching, and cutting for which haptic and visual feedback are

required. Bo et al. (2008) used the BEM with a state machine algorithm to control the computation patterns of deformation efficiently and accurately.

2.1.3 Further Modeling Approaches

2.1.3.1 Hybrid models.

A hybrid model usually divides the geometry into two operational and non-operational regions. The operation area, in which the deformation accuracy matters is modelled with a higher degree of precision while for the non-operation zone simple integration and fast computational speed of non-physical models as well as the movement flexibility, such as nonlinear deformations and topological changes are employed. While the general properties of each model are preserved, the overall computational performance of the model is enhanced compared with the continuum mechanics approaches. W. Wu and P. A. Heng (2004) developed a hybrid condensed volumetric finite element model in the operation part combined with surface-only nodes in the non-operation parts. They took advantage of the Graphics Processing Unit (GPU) accelerated computations to achieve an interactive 3-dimensional simulation of surgical cutting. Zhu and Gu (2012) evaluated the efficiency and robustness of their developed hybrid deformable model with experimental tests. They used the BEM with coarse surface meshes to simulate the global deformation combined with the MSM to simulate the dynamic interaction of the tissue with the surgical instrument.

2.1.3.2 Meshless continuum mechanics.

A high-quality mesh is always required to guarantee the physical accuracy and numerical convergence of mesh-based continuum mechanics models. Due to the complicated geometry and patient-specific nature of biological organs, discretizing the body domain is usually time-consuming. Also, it is not always possible to generate quality meshes automatically. Some meshless approaches such as meshless total Lagrangian explicit dynamics

(MTLED) (Horton, Wittek, Joldes, & Miller, 2010; Zou & Liu, 2017) and smoothed particle hydrodynamics (SPH) models have been proposed to address mentioned issues.

As in the finite element based TLED, the MTLED pre-calculates all derivatives with respect to spatial coordinates and uses the deformation gradient to determine the full system status at each time step. However, the main challenge in MTLED is combining the meshless model with the finite element shape functions to enforce the necessary boundary conditions. Several solutions such as displacement corrections strategies and radial point interpolation methods (RPIM) for easy enforcement of essential boundary conditions have been proposed by researchers (Joldes, Chowdhury, Wittek, & Miller, 2017; Yanni, Liu, Qiangqiang, Pinhua, & Chunquan, 2017). In particle-based approaches such as SPH, particles target variables are interpolated over a distance from neighbouring particles by a Kernel function. Rausch, Karniadakis, and Humphrey (2017) employed a normalized total Lagrangian approach to simulate the material discontinuity of soft tissue damage. Palyanov, Khayrulin, and Larson (2016) proposed a predictive-corrective incompressible SPH (PCISPH) for biological soft tissue simulation.

2.1.3.3 Machine learning models.

Data-driven approaches widely used in machine learning (ML) algorithms have found their application in medical simulation procedures relatively recently (Deo, 2010). The ML method is usually conducted in offline and online phases. In the offline stage, the model is trained and its hyperparameters are optimised with hundreds of thousands of data points from the target application. The model's estimation error is minimised with the help of either an accurate biomechanical model such as FEM or pre-operation measurements such as MRI and CT scans. The trained model predicts the target variable status such as displacement in real time under unseen conditions. Tonutti, Gras, and Yang (2017) employed artificial neural network (ANN) and support vector regression (SVR) methods for tumour's deformation

estimation in image-guided neurosurgery. Lorente et al. (2017) used supervised ML regression methods such as random forests and decision trees for human's liver behaviour simulation during breathing. The performance of a ML model is highly dependent on the training data and the learning algorithm.

Due to the wide variety of deformable models, the selection of the desired approach depends on the application of the target medical simulator. As explained in section 2.1, some models promise the physical accuracy, whereas some others are highly interactive and can be used in real-time applications. A comparison between the performance of some commonly used deformable models in terms of speed and accuracy is presented in Table 2-2.

Table 2-2. Comparison of deformable models

Deformable model	Speed	Accuracy
Geometrically based	****	*
MSM	****	***
Linked volumes	*****	*
FEM	***	*****
Meshless methods	***	****
ML	****	****

*Key: ***** is the highest, and * is the lowest.*

2.2 Realistic vs. Interactive Model Challenges

First, in order to simulate the mechanical behaviours of soft tissues realistically, the geometry of anatomical models is obtained from the patient-specific medical images. This process is still not fully automated and requires significant manual image segmentation and mesh generation. Furthermore, the material properties of tissues need to be characterized. The patient-specific nature of such features makes the prediction of *in vivo* tissue behaviour difficult. In addition to that, most biological soft tissues exhibit anisotropic and heterogeneous stiffness and are nearly incompressible (Kenedi, Gibson, Evans, & Barbenel, 1975). Analytical solutions to such problems are computationally expensive and involve inaccuracy or even instability in simulation. Boundary conditions are also challenging to define due to the complex tissue

composition and interactions between organs. Challenges mentioned above necessitate a solution that could offer adaptive corrections with the help of real-time direct measurements.

Second, the challenge of interactive simulation requires fast solutions to deformable objects. The update frequency required for visual feedback is at least 25 Hz to achieve a real-time user interaction with virtual soft tissue models. Soft tissue response must be computed in a fraction of a second to achieve the required update rates of visual feedback that simulates motion of rendered graphics to be perceived as a smooth uninterrupted motion by the user. Due to the complex characteristics of the biological soft tissues, numerical solutions are often computationally expensive, and simplifications of the problem are required to achieve real-time performance, adversely affecting the simulation accuracy (Kerdok et al., 2003).

The principal drawback of MSMs, as one of the most promising non-physical approaches, is that they do not reproduce the constitutive laws to represent the mechanical parameters of the model (Niroomandi et al., 2012). The computation of such models is fast, but the iterative process of calculations is not robust. The modeler often needs to set the system parameters such as elasticity and damping coefficients, initial position, velocity of mass, and mass quality manually, from experience (Zhou, Luo, Li, & Deng, 2018). In order to increase the realism of a MSM, several complex techniques such as proposing angular springs for an anisotropic behaviour simulation (Liu, Shaoping, Hua, & Linyan, 2011), multilayer tissue simulation (Meehan, Teschner, & Girod, 2003), spring force direction dependency (Neumann, Sadler, & Gieser, 1998), non-constant stiffness (Picinbono, Lombardo, Delingette, & Ayache, 2002), and damping factors (Georgii & Westermann, 2005) have been developed.

In linked volume models, such as the basic approach and the ChainMail, the elements are rigid and indivisible, and local refinement techniques are required to improve the realism performance. Hence, the higher number of nodes and elements has led to possibly critical stability compared to MSM, although the volumetric behaviour of the model is improved

(Meier et al., 2005). However, the computational efficiency of the linked volume approaches afforded by the elements position adjustment techniques has made improvements in many medical applications such as percutaneous transhepatic cholangio-drainage (PTCD) simulation (Fortmeier, Mastmeyer, Schroder, & Handels, 2016). Medical applications with large volume deformations, in which millions of voxels are involved, can benefit from the simplicity of computations in linked volume models (Rodríguez et al., 2016; Rodríguez, León, Arroyo, & Mantas, 2015).

The FEM can achieve high accuracy in large scale models, but this is achieved at the cost of slow computational performance. To enhance the computational performance of the FEM, a variety of techniques have been proposed. In precomputation approaches, the equilibrium equations are precomputed, then superposition principle is applied to determine nodal target variables (Cotin, Delingette, & Ayache, 1999). The main disadvantage of the precomputation methods is that they are only valid for a precomputed stiffness matrix configuration. The matrix condensation method limits the computations to a new matrix system involving only the target variables at surface nodes (Lee, Popescu, Joshi, & Ourselin, 2006; Wen Wu & Pheng Ann Heng, 2004). The condensation method is not suited to moderate deformations and rotations. To address these limitations, some researchers (Comas et al., 2008; Miller, Joldes, Lance, & Wittek, 2007; Taylor et al., 2008) employ Total Lagrangian Explicit Dynamics (TLED) algorithm for nonlinear models. The TLED considers all variables in reference to the initial status of the model, leading to three main advantages.

1. Time derivatives with respect to the original configuration can be precomputed, leading to an enhanced computation.
2. Error accumulation does not occur as each variable is computed compared to the initial configuration and the error at each time step does not add up.

3. External and internal masses and forces are lumped to the nodes, and so, the mass and damping matrices are formed in block diagonal matrices. This makes computations possible at element level, leading to enhanced computational performance.

BEM benefits from the continuum mechanics accuracy but suffers from its scalability. The method is formed based on the assumption that the interior material is isotropic and homogeneous to limit the equilibrium integrals on surface. Hence, the BEM cannot accommodate the anisotropic and heterogeneous characteristic of soft tissue. Besides, the global matrix in the BEM is dense and asymmetric and needs to update at each timestep. Thanks to its enhanced computational performance compared to the FEM, BEM has found its application in many medical simulation procedures (Wang et al., 2007; Zhu & Gu, 2012). However, its application requires the derivation of complex fundamental solutions that proved to be impractical for non-research applications.

Similar to BEM, the hybrid approach has difficulties in finding the balance between computational performance and realistic response model. The preselection of sections and the criteria involved in defining two operation and non-operation zones are a big challenge and has to be carried out manually. Further to this, the interface between the two modelling zones is problematic as both operation and non-operation zones are required to perform identically in the models' interface (Meier et al., 2005).

Despite the advantage of meshless approaches in handling large deformation and discontinuities, the model's physical accuracy highly relies on the proper placement of the domain nodes (De, Kim, Lim, & Srinivasan, 2005). Besides, due to the complex procedure of employing FEM shape functions in meshless models, they usually have difficulty in handling sampled regions (Wittek, Grosland, Joldes, Magnotta, & Miller, 2016).

Overall, the realistic and interactive characteristics of medical simulations pose challenges to each other mutually, and performance improvement on one aspect is mainly achieved by the detriment of the other. Table 2-3 presents computational performance of some deformable models in the last decades.

Table 2-3. Computational performance of deformable models

Deformable model	Year	Properties	Frequency	Hardware
Data-driven FEM	2009	1691 tetrahedrons	10 Hz	not specified
MTLED	2010	4314 nodes	67 Hz	Intel P iv 3 GHz
MSM	2016	15946 tetrahedrons	30 Hz	Intel i7 3.4 GHz
PCISPH	2016	250305 particles	2 Hz	Intel i5 3.3 GHz
ML	2017	394000 nodes (appx.)	3 Hz	Intel i7 3.4 GHz

The performance of deformable models presented in Table 2-2 and Table 2-3 confirms the difficulty in achieving a real-time interactive response while not sacrificing the physical accuracy of the simulation. This project aims to address the mentioned challenge in medical simulations and develop a real-time solution for accurate continuum mechanics models.

2.3 Lack of Real-time Corrective Response

The biological soft tissue structure is complex and often consists of different tissues layers with ligaments and fascia. Hence, forming realistic models can be very challenging. A common approach is to use FEM with experimentally defined constants characterising the material behaviour (Famaey & Vander Sloten, 2008). Zhang et al. (2019) used an iterative solution that alternates between high-quality 2D CTs estimates and a FEM-guided 3D deformation vector field (DVF) for automatic tumour localisation.

However, the material properties of the soft tissue are highly patient-specific. Besides, soft tissue exhibits various behaviour under different external loading conditions. The elastic modulus of a healthy soft tissue such as muscle and liver ranges from 1 to 34 kPa, whereas the elastic modulus of some common types of cancerous tumours varies between 112 and 638 kPa (Guy Lamouche et al., 2012). The wide range of elasticity modulus makes it impossible to

develop a deformable model with high predictability solution that suits all deformation situations.

Peeken et al. (2018) developed pre- and post-therapeutic ML-based models to predict soft tissue sarcoma's (STS) death and progress at two years. In the feature importance analysis, patient's age appeared to be a discriminative parameter in both pre- and post-therapeutic models.

Hence, any deformable model with an accurate physics-based solution still suffers from the unpredictability of soft tissues *in vivo* behaviour in real-time applications. This project proposes a model that introduces the model error into the system equations. The error is validated through a set of experiments and is employed to correct the system estimates with the knowledge of the model's uncertainty compared to the direct measurements.

2.4 Partially Defined System Inputs

The accuracy of any deformable model is entirely dependent on the accuracy of the system inputs. In deformation simulation of biological soft tissues for medical applications, the system input is usually the external load. However, the applied force on the target tissue cannot be tightly controlled and is often measured with medical instrument such as force sensors that generates substantive noise. Hence, the accuracy of the measured force, i.e. the system input, is not guaranteed. The inaccurate input reduces the reliability of the developed model in real-time applications in which the system inputs are not fully known.

Many efforts have been taken by researchers to address the uncertainty of the simulation system inputs. Zhao and Pelegri (2016) employed a Bayesian approach with an inverse FE characterisation procedure to estimate viscoelasticity of soft tissue in the presence of measurement noise. Mayeur, Witz, Lecomte-Grosbras, Cosson, and Brieu (2018) presented a non-intrusive method to assess mechanical properties of soft tissue. It was shown that mechanical properties of the tissue in the FE model need to be optimised to obtain the observed

displacement from MRIs. (Richardson et al., 2018) developed an experimental setup to measure the lung volume by tracking the surface deformation. It is seen from the obtained volume-pressure relationship that either measured variables can be very noisy under constant condition.

This work aims to develop a predictive algorithm that can minimise the error of estimates despite noisy inputs of the system. In real-time applications while the true reference value is not known due to the measurement noise and the model error as explained in sections 2.2 and 2.3, a robust predictive algorithm should be able to estimate the tissue response with acceptable accuracy, and this is in addition that the system inputs are not fully known.

2.5 Tissue's Nonlinear Behaviour

Due to the computational complexity of medical simulators, most of the existing methods for simulating soft tissue deformation use linear elastic laws. The theory of linear elasticity assumes a linear relationship between the components of stress and strain. Also, strain components are linearly computed from displacement vectors, hence being able to simulate tissue's small deformation only. However, nonlinear formulations are required to achieve higher physical accuracy for simulation of biological soft tissue deformation.

Many geometrically nonlinear models have been proposed to address large deformations of soft tissue. Lim and De (2007) used a point-collocation-based method (PCMFS) to simulate nonlinear geometric tissue response in virtual surgery. Shaoping Xu, Liu, Hua Zhang, and Linyan Hu (2011) used a nonlinear tensor-mass model (TMM) for surgery simulation. The nonlinear corotational FEM has also been employed by many researchers (Courtecuisse et al., 2014; Courtecuisse et al., 2010; Plantefeve et al., 2016).

However, most nonlinear models, as mentioned above, use a linear material law. In other words, they model large nonlinear deformations but still cannot simulate tissue's deformation resulted from nonlinear material behaviour. Schwartz, Denninger, Rancourt,

Moisan, and Laurendeau (2005) developed a material nonlinear TMM in which the two Lamé constants were modified to represent the local nonlinear elastic behaviour. However, their model did not comply with the material's constitutive laws. The most promising nonlinear hyper-elastic models have been the Total Lagrangian-based models. In this approach, the Second Piola-Kirchhoff stress tensor and the Green-Saint Venant strain tensor are employed with derivatives concerning the initial state of the domain configuration (Miller et al., 2007). Various Total Lagrangian-based methods, such as the Total Lagrangian SPH (Rausch et al., 2017), Total Lagrangian FEM with implicit integration (Mafi & Sirouspour, 2014), MTLED (Horton et al., 2010), and Multiplicative Jacobian Energy Decomposition (MJED) (Marchesseau, Heimann, Chatelin, Willinger, & Delingette, 2010) have been developed to simulate large nonlinear deformation of the biological soft tissue with nonlinear material behaviour.

Despite improvements in computer hardware and computational methods, the Total Lagrangian-based approaches present a challenge for the interactive applications due to the nature of such models' computations being done in the element level which leads to lengthy calculations depending on the size of the mesh. This work aims to launch a computational algorithm that takes advantage of the TLED nonlinear performance but also achieves update frequencies within the range of real-time performance.

2.6 Kalman Filter

The Kalman filter (KF) has long been regarded as the optimal solution to many tracking and visual motion analysis tasks. KF is constructed as an optimal mean-square-error (MSE) filter that uses state-space techniques which enables the filter to be used either as a smoother, a filter, or a predictor. The state-space formulation of the filter also simplifies its implementation in a discrete domain (Simon, 2006).

KF estimates a process by using a form of feedback control: the filter estimates the process state at some time and then obtains feedback in the form of (noisy) measurements. As such, the equations for the KF fall into two groups: i) time update and ii) measurement update equations. The time update equations project the current state forward in time. The measurement update equations are responsible for the feedback. The time update equations can also be thought of as *predictor* equations, while the measurement update equations can be thought of as *corrector* equations. Indeed, the final estimation algorithm resembles that of a *predictor-corrector* algorithm for solving numerical problems. The process of finding the "best estimate" from noisy data amounts to "filtering out" the noise. However, a Kalman filter not only cleans up the data measurements but also projects these measurements onto the state estimate. Figure 2-5 shows the ongoing, recursive algorithm of the discrete Kalman filter.

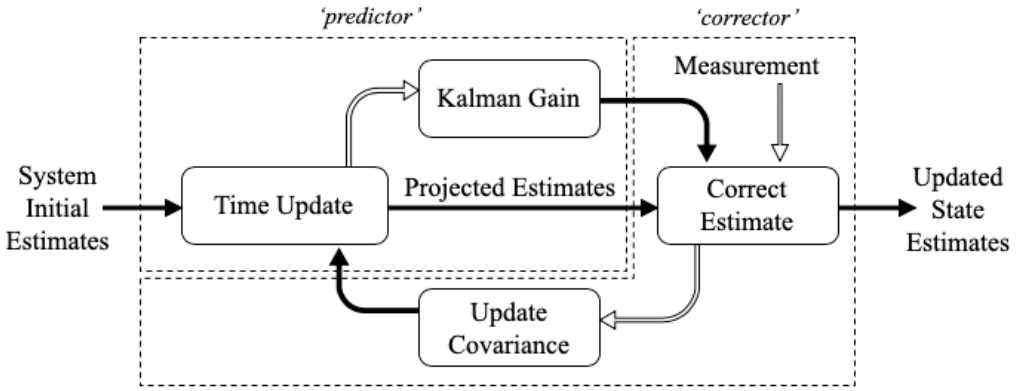

Figure 2-5. Kalman filter recursive algorithm

The ability of the KF to predict data has led to it being used in a broad range of problems. KF has been employed by many researchers for material parameters estimation of an models (Hoshi, Kobayashi, Kawamura, & Fujie, 2007; Xi et al., 2011). Hasegawa, Shimayoshi, Amano, and Matsuda (2016) used KF to reduce the number of iterations in the coupling of cardiovascular simulations, leading to a faster computational performance. Ghahremani and Kamwa (2011) used KF for dynamic state estimation in power systems. (Suga & Kawahara, 2006) used KF to estimate the tidal coastal flow.

2.7 Aims and Objectives

As illustrated in section 1.1.2, modelling of soft tissue mechanics is one of the many essential components for a realistic and interactive simulation of a medical procedure. The deformation simulation of the target soft tissue has been identified as a crucial technology for the development of the second and third generations of the aforementioned medical simulators. Mechanics of the tissue must be identified; A reliable computational algorithm requires to be developed; Fast and robust programming techniques must be utilised to achieve a realistic and interactive simulation of a medical procedure.

This work aims to establish a new algorithm to estimate soft tissue deformations and validate the response experimentally, but to also address the real-time manipulation of the deformable model. The main objectives are:

- to achieve a real-time update frequency through a fast, computational algorithm that combines displacement measurements and uses the finite element model to model soft tissue behaviour in the spatial domain without sacrificing the accuracy,
- to validate the proposed method experimentally, and reduce the error in computational predictions,
- to modify the developed algorithm and consider the model's input uncertainty resulting from the errors of force sensors, and finally
- to address the geometrical and material nonlinearity of the soft tissue.

INTENTIONALLY LEFT BLANK

CHAPTER 3

DEFORMATION ESTIMATION BY KF-FEM

INTENTIONALLY LEFT BLANK

3 Deformation Estimation by KF-FEM

In the first study, the spatio-temporal KF-FEM algorithm is developed. To this purpose, the FE equilibrium equation is temporally linearized with the help of the Newmark-β method. The developed model is then employed as the system equation of the Kalman filtering process. Displacement at some boundary nodes of the geometrical domain is measured and introduced into the developed filtering system as direct measurements. The proposed novel combination of the KF and the FEM uses the partially available measurement to enhance the computational speed as well as to expand the estimates in the spatial domain.

3.1 Method

3.1.1 System Equations

Consider we collect displacement measurement from multiple adjacent mesh nodes that are in contact with the probe tip. The three directional measurement vector at discrete time point k is defined as $\boldsymbol{y}_k \equiv [d_{1x} \quad d_{1y} \quad d_{1z} \quad d_{2x} \quad d_{2y} \quad \dots \quad d_{my} \quad d_{mz}]^T$. It is assumed that the measurement error, v, is spatially uncorrelated with normal distribution around zero, i.e. the white Gaussian noise. Hence, the measurement error has a diagonal covariance matrix $\boldsymbol{R}$, i.e., $v \sim (0, R)$ and $\boldsymbol{E}\left[v_i v_j^T\right] = \boldsymbol{R}[\delta_{ij}]$, where $\boldsymbol{E}[\ ]$ is the expected value, and δ_{ij} is the Kronecker delta function.

Covariance is a measure of how much two random variables vary together, and the covariance matrix is a square matrix that the main diagonal elements are variances and all other off-diagonal elements are the covariance between corresponding elements. It is assumed that the error of the measured displacement at each point is independent from the error at other points. In other words, there is no correlation between measurement error of different points

when the measuring is repeated under identical conditions. So, in the covariance matrix $\boldsymbol{R}$, as introduced above, all off-diagonal elements are zero. The diagonal elements, i.e., the variance of measurement error at each point is calculated from $\sum_{i=1}^{n}(x_i - \bar{x})^2/(n-1)$, where n is the number of measurements and $\bar{x}$ is the mean of the measurements under identical conditions.

The target variable, $\boldsymbol{x}_k$, is the displacement vector at all mesh nodes at each time point. As the measurement vector addresses displacement at some nodes out of the entire spatial domain, it can be mapped from the target variable with a binary matrix, i.e. the measurement matrix $\boldsymbol{H}$, as follows.

$$\boldsymbol{y}_k = \boldsymbol{H}\boldsymbol{x}_k + \boldsymbol{v} \tag{3-1}$$

Appendix A elaborates further with an example that shows how the measurement matrix H is formed to map the contact points displacement out of the entire geometrical domain.

To be able to estimate the target variable $\boldsymbol{x}_k$, it should be defined through a linear discrete-time dynamic model in the global coordinate system as follows (Yarahmadian, Zhong, Gu, & Shin, 2017),

$$\boldsymbol{x}_{k+1} = \boldsymbol{F}\boldsymbol{x}_k + \boldsymbol{G}\boldsymbol{z}_k \tag{3-2}$$

where $\boldsymbol{z}_k$ is the system input. $\boldsymbol{F}$ and $\boldsymbol{G}$ are the transition and input matrices, respectively, and will be derived from the constitutive law's equilibrium equation. The target variable $\boldsymbol{x}_k$ is estimated in two stages. In the first stage, hereafter called the prediction, the model calculates the expected value of the $\boldsymbol{x}_{k+1}$ from equation (3-1), using the displacement measurement ($\boldsymbol{y}$) before but not including time $k+1$. The predicted value is called *priori* estimate and shown with $\hat{x}_{k+1}^{-}$. The *priori* estimates and covariance (P_{k+1}^{-}) of the system are calculated for each time step $k = 1, 2, \ldots$ as follows,

$$\hat{\boldsymbol{x}}_{k+1}^{-} = \boldsymbol{F}\hat{\boldsymbol{x}}_k^{+} + \boldsymbol{G}\boldsymbol{z}_k \tag{3-3}$$

$$P_{k+1}^{-} = \boldsymbol{F}P_k^{+}F^T \tag{3-4}$$

where F^T is the transpose of the transition matrix; $\hat{x}_k^+$ and P_k^+ are the *posteriori* estimate and covariance of the system using measurements up to and including time k, respectively. It is shown (Simon, 2006) that the recursive least squares Kalman filter is given by the following equations:

$$\boldsymbol{K}_{k+1} = P_{k+1}^- \boldsymbol{H}^T (\boldsymbol{H} P_{k+1}^- \boldsymbol{H}^T + \boldsymbol{R})^{-1} \tag{3-5}$$

$$\widehat{\boldsymbol{x}}_{k+1}^+ = \widehat{\boldsymbol{x}}_{k+1}^- + \boldsymbol{K}_{k+1}(\boldsymbol{y}_{k+1} - \boldsymbol{H}\widehat{\boldsymbol{x}}_{k+1}^-) \tag{3-6}$$

$$P_{k+1}^+ = (\boldsymbol{I} - \boldsymbol{K}_{k+1}\boldsymbol{H}) P_{k+1}^- \tag{3-7}$$

where $\boldsymbol{K}_{k+1}$ is the Kalman gain and $\boldsymbol{I}$ is the identity matrix. The term $\boldsymbol{y}_{k+1} - \boldsymbol{H}\widehat{\boldsymbol{x}}_{k+1}^-$ in the equation (3-6) is called the *innovation*. In fact, it is the difference between the predicted state $\boldsymbol{H}\widehat{\boldsymbol{x}}_{k+1}^-$ and the measured state $\boldsymbol{y}_{k+1}$ at the next time step.

3.1.2 Finite Element Formulation

It is assumed that the target body domain obeys the linear isometric elastic material law in the range of small displacements. Tadepalli, Erdemir, and Cavanagh (2011) compared the performance of hexahedral and tetrahedral elements in FE models and discusses the suitability of such assumption. We discretize the geometrical body domain Ω into finite number of 4-node tetrahedral elements. Shape functions are calculated from:

$$N_a(x, y, z) = {}^1\!/_{6V}\,(a_a + b_a x + c_a y + d_a z), \qquad a = 1, 2, 3, 4 \tag{3-8}$$

where

$$6V = det \begin{bmatrix} 1 & x_1 & y_1 & z_1 \\ 1 & x_2 & y_2 & z_2 \\ 1 & x_3 & y_3 & z_3 \\ 1 & x_4 & y_4 & z_4 \end{bmatrix} \tag{3-9}$$

and

$$a_1 = det \begin{bmatrix} x_2 & y_2 & z_2 \\ x_3 & y_3 & z_3 \\ x_4 & y_4 & z_4 \end{bmatrix}, \quad b_1 = det \begin{bmatrix} y_2 & z_2 & 1 \\ y_3 & z_3 & 1 \\ y_4 & z_4 & 1 \end{bmatrix}$$

$$c_1 = det\begin{bmatrix} z_2 & 1 & x_2 \\ z_3 & 1 & x_3 \\ z_4 & 1 & x_4 \end{bmatrix}, \quad d_1 = det\begin{bmatrix} 1 & x_2 & y_2 \\ 1 & x_3 & y_3 \\ 1 & x_4 & y_4 \end{bmatrix} \tag{3-10}$$

with the other constants defined by cyclic interchange of subscripts in the order $1, 2, 3, 4$. The weak form of linear elasticity equilibrium equation, as further discussed in section 3.2, in terms of nodal displacement $\boldsymbol{u}$ in the element level is written as

$$\boldsymbol{M}_{ab}\ddot{\boldsymbol{u}}_b + \boldsymbol{K}_{ab}\boldsymbol{u}_b = \boldsymbol{f}_a \tag{3-11}$$

with the mass matrix $\boldsymbol{M}_{ab} = \sum_e \boldsymbol{M}_{ab}^e$, and the stiffness matrix $\boldsymbol{K}_{ab} = \sum_e \boldsymbol{K}_{ab}^e$ for each nodal pair, and the external force $\boldsymbol{f}_a = \sum_e \boldsymbol{f}_a^e$ at each node on the surface domain. $\ddot{\boldsymbol{u}}$ denotes the nodal acceleration. The element mass and stiffness matrices are calculated from

$$\boldsymbol{M}_{ab}^e = \int_{\Omega_e} \boldsymbol{N}_a \rho \boldsymbol{N}_b d\Omega I, \quad \boldsymbol{K}_{ab}^e = \int_{\Omega_e} \boldsymbol{B}_b^T \boldsymbol{D} \boldsymbol{B}_b d\Omega \tag{3-12}$$

where ρ is the density, $\boldsymbol{B}_b$ is the three-dimensional strain-displacement matrix calculated from

$$\boldsymbol{B}_b = \begin{bmatrix} \partial N_b/\partial x & 0 & 0 & \partial N_b/\partial y & 0 & \partial N_b/\partial z \\ 0 & \partial N_b/\partial y & 0 & \partial N_b/\partial x & \partial N_b/\partial z & 0 \\ 0 & 0 & \partial N_b/\partial z & 0 & \partial N_b/\partial y & \partial N_b/\partial x \end{bmatrix}^T \tag{3-13}$$

and matrix D is

$$\boldsymbol{D} = \frac{E}{(1+\nu)(1-2\upsilon)}\begin{bmatrix} 1-\upsilon & \upsilon & \upsilon & 0 & 0 & 0 \\ \upsilon & 1-\upsilon & \upsilon & 0 & 0 & 0 \\ \upsilon & \upsilon & 1-\upsilon & 0 & 0 & 0 \\ 0 & 0 & 0 & (1-2\upsilon)/2 & 0 & 0 \\ 0 & 0 & 0 & 0 & (1-2\upsilon)/2 & 0 \\ 0 & 0 & 0 & 0 & 0 & (1-2\upsilon)/2 \end{bmatrix} \tag{3-14}$$

with E the elasticity modulus and υ that is the Poisson's ratio. By assembling all the elements into a global formulation and considering Reyleigh damping matrix $\boldsymbol{C} = c_1\boldsymbol{M} + c_2\boldsymbol{K}$, where c_1 and c_2 are determined experimentally, the equilibrium equation can be written as (Zienkiewicz, Taylor, & Zhu, 2013):

$$\boldsymbol{M}\ddot{\boldsymbol{u}} + \boldsymbol{C}\dot{\boldsymbol{u}} + \boldsymbol{K}\boldsymbol{u} = \boldsymbol{f} \tag{3-15}$$

Equation (3-15) requires a temporal solution for the time duration of the analysis to be representable as the system equation of the Kalman filter.

3.1.3 Implicit Time Integration

To formulate the equilibrium equation (3-15) in the time domain, a temporal discretization method is required. The discrete time Newmark-β method describes how a state at time point t_k is determined at time t_{k+1}. In short-time small deformations, the constant acceleration Newmark assumes that the nodal acceleration is constant between time points t_k and t_{k+1}. Two Newmark formulas are as follows.

$$\boldsymbol{u}_{k+1} = \boldsymbol{u}_k + \Delta t \dot{\boldsymbol{u}}_k + (1/2 - \beta)\Delta t^2 \ddot{\boldsymbol{u}}_k + \beta \Delta t^2 \ddot{\boldsymbol{u}}_{k+1} \tag{3-16}$$

$$\dot{\boldsymbol{u}}_{k+1} = \dot{\boldsymbol{u}}_k + (1 - \gamma)\Delta t \ddot{\boldsymbol{u}}_k + \gamma \Delta t \ddot{\boldsymbol{u}}_{k+1} \tag{3-17}$$

where $\Delta t = t_{k+1} - t_k$. The constant acceleration Newmark with coefficients $\beta = 1/4$ and $\gamma = 1/2$ for its fast implicit and unconditionally stable performance (Zienkiewicz et al., 2013) is used to develop the proposed KF-FEM. We correlate each node's displacement, velocity, and acceleration in equation (3-15) with the help of equations (3-16) and (3-17).

3.1.4 KF-FEM Algorithm

We take the displacement as the independent variable and find the velocity and acceleration from two independent Newmark formulas (3-16) and (3-17) as follows.

$$\ddot{\boldsymbol{u}}_{k+1} = 4/\Delta t^2 \,.\, (\boldsymbol{u}_{k+1} - \boldsymbol{u}_k) + 4/\Delta t \,.\, \dot{\boldsymbol{u}}_k - \ddot{\boldsymbol{u}}_k \tag{3-18}$$

$$\dot{\boldsymbol{u}}_{k+1} = 2/\Delta t \,.\, (\boldsymbol{u}_{k+1} - \boldsymbol{u}_k) - \dot{\boldsymbol{u}}_k \tag{3-19}$$

Then, we insert equations (3-18) and (3-19) into the equation (3-15) and formulate the linear discrete-time dynamic FE equation as

$$(4\boldsymbol{M}/\Delta t^2 + 2\boldsymbol{C}/\Delta t + \boldsymbol{K})\boldsymbol{u}_{k+1} = (4\boldsymbol{M}/\Delta t^2 + 2\boldsymbol{C}/\Delta t)\boldsymbol{u}_k + (2\boldsymbol{M}/\Delta t + \boldsymbol{C})\dot{\boldsymbol{u}}_k + \boldsymbol{M}\ddot{\boldsymbol{u}}_k + \boldsymbol{f}_{k+1}. \tag{3-20}$$

By defining $\boldsymbol{A} \equiv 4\boldsymbol{M}/\Delta t^2 + 2\boldsymbol{C}/\Delta t$, $\boldsymbol{L} \equiv 2\boldsymbol{M}/\Delta t + \boldsymbol{C}$, and $\boldsymbol{J} \equiv \boldsymbol{A} + \boldsymbol{K}$, the developed KF-FEM model can be written as

$$\boldsymbol{u}_{k+1} = [\boldsymbol{J}^{-1}\boldsymbol{A}]\boldsymbol{u}_k + [\boldsymbol{J}^{-1}\boldsymbol{L} \quad \boldsymbol{J}^{-1}\boldsymbol{M} \quad \boldsymbol{J}^{-1}] \begin{bmatrix} \dot{\boldsymbol{u}}_k \\ \ddot{\boldsymbol{u}}_k \\ \boldsymbol{f}_{k+1} \end{bmatrix}. \tag{3-21}$$

We take the global displacement $\boldsymbol{u}_{k+1}$ as the system state, i.e., $\boldsymbol{x}_{k+1}$ in equation (3-2), and define other system parameters as $\boldsymbol{F} = [\boldsymbol{J}^{-1}\boldsymbol{A}]$, $\boldsymbol{G} = [\boldsymbol{J}^{-1}\boldsymbol{L} \quad \boldsymbol{J}^{-1}\boldsymbol{M} \quad \boldsymbol{J}^{-1}]$, and $\boldsymbol{z}_{k+1} = [\dot{\boldsymbol{u}}_k \quad \ddot{\boldsymbol{u}}_k \quad \boldsymbol{f}_{k+1}]^T$. The measurement matrix *H* will be defined according to the boundary conditions of the body domain in a way that the observed displacements from the tissue manipulator's tip addresses the relevant nodes from the surface domain.

3.1.5 Real-time Approach

As can be seen from equations (3-4), (3-5), and (3-7), calculation of the estimator covariances and the Kalman gain does not require measurement and state values. Hence, these calculations can be done before the simulation starts. We call this stage the *offline* phase. Hence, we run the proposed algorithm in two *offline* and *online* phases to improve the computational performance of the solver. In the *online* phase, the algorithm circulates through equations (3-3) and (3-6) to calculate the *priori* and *posteriori* estimates at each time step. The two-phase approach, as explained above, is crucial to achieve a real-time performance. Two phases of the developed KF-FEM algorithm are shown in Figure 3-1.

3.2 Code Structure

The proposed algorithm requires to be developed through a well-structured code script. This is to avoid repeated and unnecessary calculations and memory usage in the process of simulation. The code is divided into five sections that can be run separately. This approach eases the process of debugging and makes erasing of unrequired variables possible to enhance the computation. Five steps of the code structure include geometry preparation, forming

material properties, detecting boundary conditions, the offline phase of the KF-FEM, and the real-time phase of the proposed KF-FEM. The five stages of the programmed structure with key activities of each stage are illustrated in Figure 3-2.

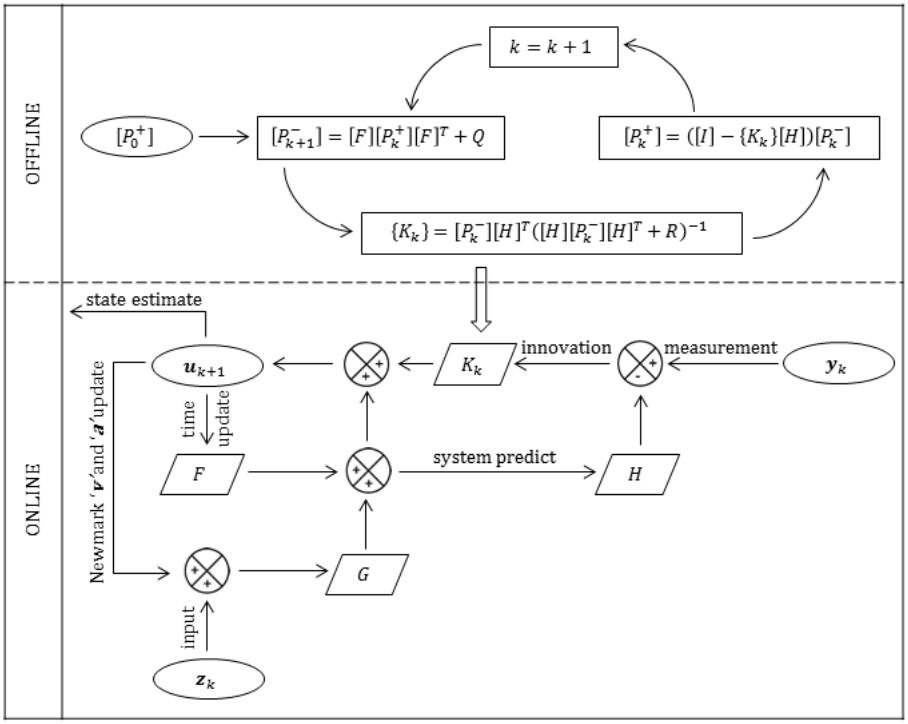

Figure 3-1. The KF-FEM algorithm

3.3 Soft tissue deformation estimation by spatio-temporal Kalman filter FE method

The performance of the developed algorithm is verified, and results are published. Please refer to Appendix B for details.

3.4 Performance Evaluation

For the comparison purposes, the FEM was carried out with Abaqus 6.14 using the implicit Newmark method to derive the displacement at the centre point of the contact area (hereafter, the observation point). Damping was set as recommended by (Taylor et al., 2008). The observation point displacement values from the FEM generated with Abaqus are taken as gold standard values (see Figure 3-4).

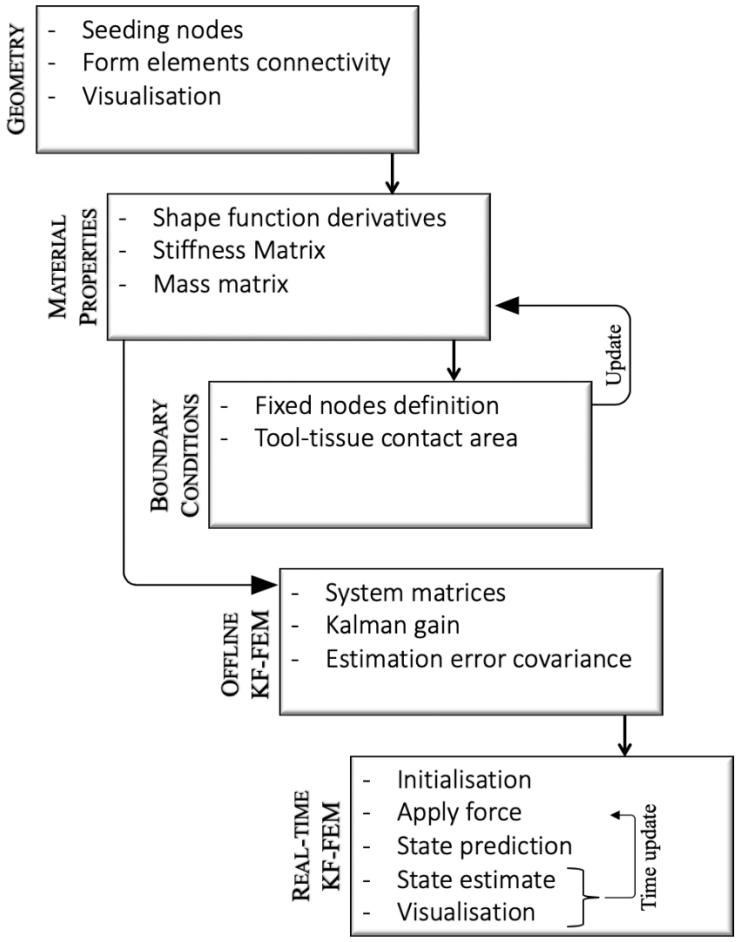

Figure 3-2. The proposed KF-FEM code structure

3.4.1 Simulation Setup

The developed KF-FEM was coded in MATLAB R2015b, and the initial value of the system state was set to zero. In other words, the initial state of the geometry is undeformed, and so, the system state that is the displacement vector of all nodes is set to zero. However, because of user errors and machine inaccuracies, the initial value of the displacement might not be zero in practice. Hence, the initial estimation error covariance was set 0.0001, i.e., a minimal but non-zero value. Measurements required for the KF system equations are generated artificially by adding a random white Gaussian noise to the valid values obtained from the FEM. The 3D surface scan of a pig liver was used to form and visualise the geometry. Then, the geometrical domain was discretized with two different number of linear tetrahedral elements to evaluate the effect of mesh complexity on the proposed method accuracy and computational

speed, as shown in Table 3-1. The tissue's density, Poisson's ratio, and Young's modulus are from the literature (Chui, Kobayashi, Chen, Hisada, & Sakuma, 2004; Samur, Sedef, Basdogan, Avtan, & Duzgun, 2007).

Table 3-1. The liver model mesh properties

	Mesh 1	Mesh 2
No. of nodes	1173	2162
No. of elements	4094	7887

Trials were conducted to study the behaviour of both meshes under the indentation condition (i.e., a compression force at one contact area). We applied a linearly increasing compression force over an area consisting of 8 elements from zero to 0.4 N to simulate the probe's indentation. The force level was selected within the interaction force range of soft tissues that is 0.00004 N-92.0 N (van Gerwen, Dankelman, & van den Dobbelsteen, 2012). It is assumed that there is no rigid body motion that is a realistic assumption for this force magnitude (see Figure 3-3).

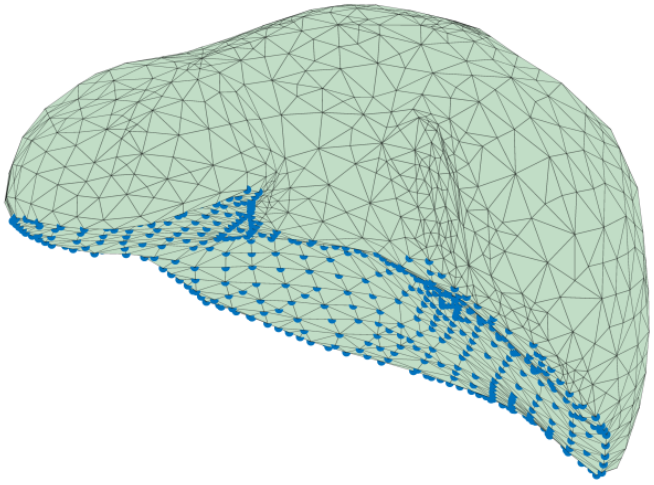

Figure 3-3. Boundary conditions – mesh 2 (fixed nodes are marked with blue)

3.4.2 Estimates Accuracy

Figure 3-4 compares displacements at the observation point obtained by the proposed KF-FEM with the true values from the FEM and measurements (mesh 2). Besides, the normalized error percentage of estimates against measurements concerning the reference FE is

computed from $e_N = (u_i - u_{FE})/u_{max,FE} \times 100$ for $u_i = u_{KF}$ & $u_{meas.}$ and illustrated in Figure 3-4.

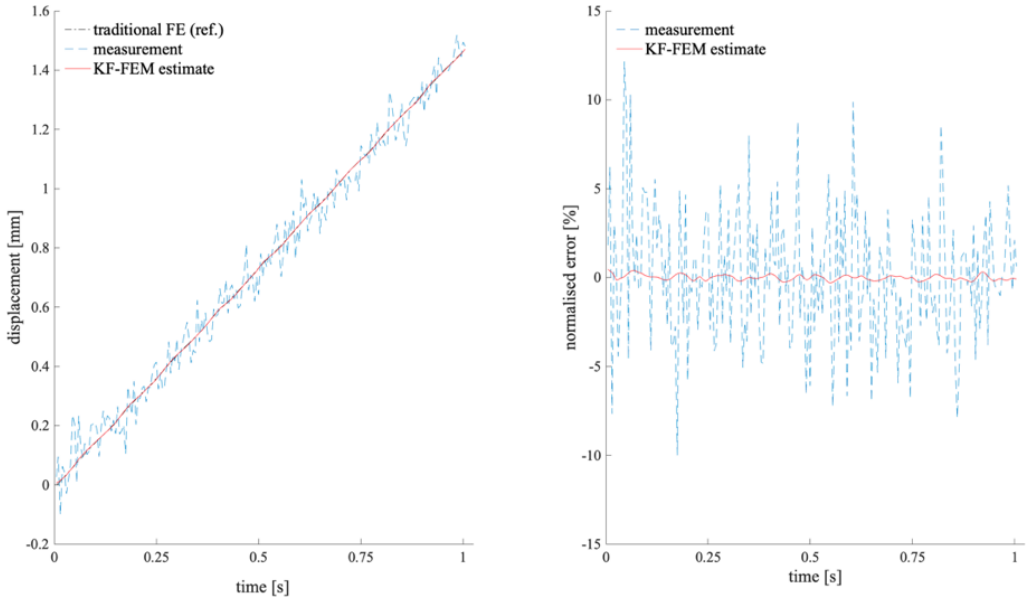

Figure 3-4. Displacement at the observation point from KF-FEM vs. FEM (left), and the normalized error percentage of estimates compared to the measurement (right) – mesh 2

The median error reduction of 90.19% and 96.04% is achieved from mesh 1 and mesh 2 simulations, respectively. Figure 3-5 shows percentage of the reduced error from measurements with the proposed KF-FEM. In addition to that, the absolute value of errors with their medians is computed and shown in Figure 3-6.

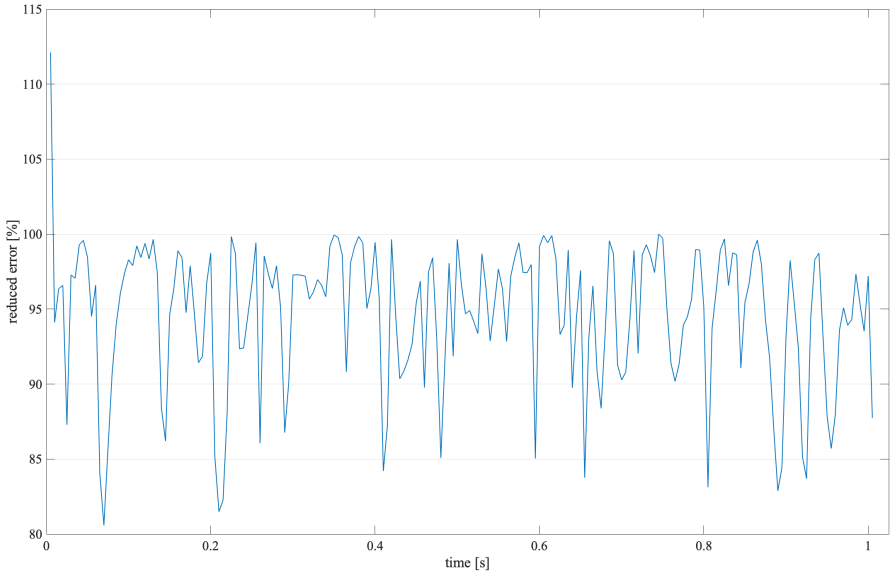

Figure 3-5. The reduced error from measurements (percent) with KF-FEM – mesh 2

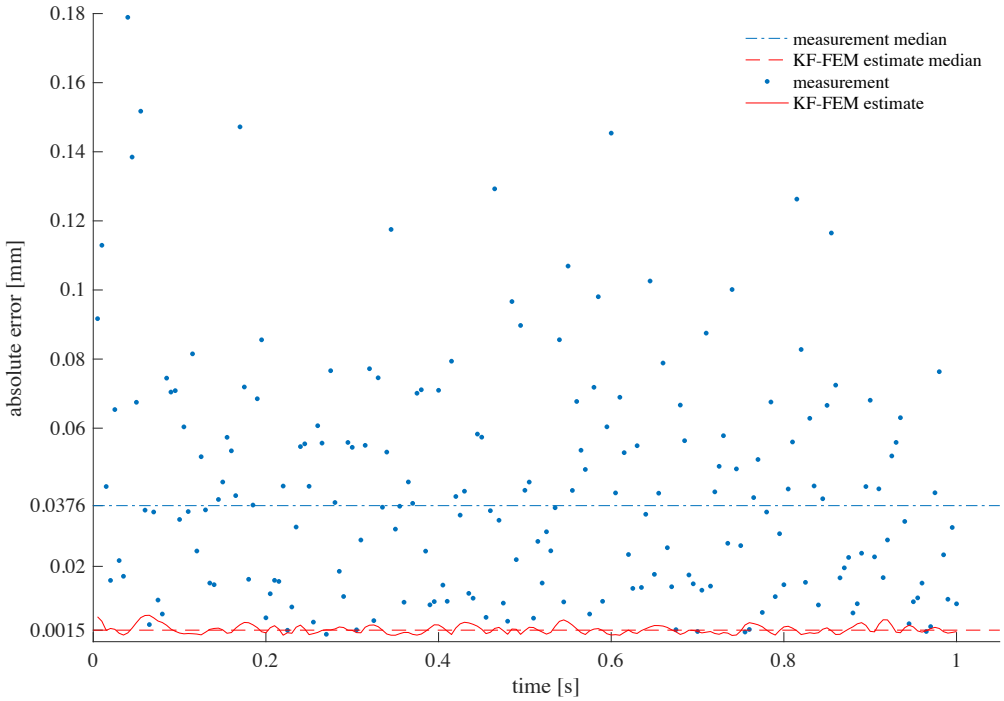

Figure 3-6. The absolute error of KF-FEM estimates vs. measurements – mesh 2

3.4.3 Computational Speed

Simulations were performed on a PC with Intel® Core™ i5-6500 CPU @ 3.20 GHz, 8.00 GB RAM and 64-bit Windows 7. The computational performance of both the FEM with Abaqus and the developed KF-FEM with MATLAB was recorded to assess the computational power of the proposed method. Table 3-2 shows the total computational CPU time and the update frequency of each time step for both simulations. The computational time of the KF-FEM was shorter, allowing to achieve the 25 Hz graphical refresh rate required for real-time visual.

Table 3-2. The computational CPU time and the update frequency

	Total CPU time [s]		Update frequency [Hz]	
	FEM	KF-FEM	FEM	KF-FEM
Mesh 1	40.2	2.25	4.98	88.90
Mesh 2	73.5	5.46	2.72	36.63

Figure 5 shows the estimated deformation of the liver model (mesh 2) by the proposed KF-FEM. The maximum estimated displacement was 1.472 mm compared to the maximum displacement 1.434 mm obtained by the FEM using software ABAQUS, that is less than 3%

different. It should be noted that due to differences in colour definition contours in MATLAB and ABAQUS, displacement colour map obtained from either looks different.

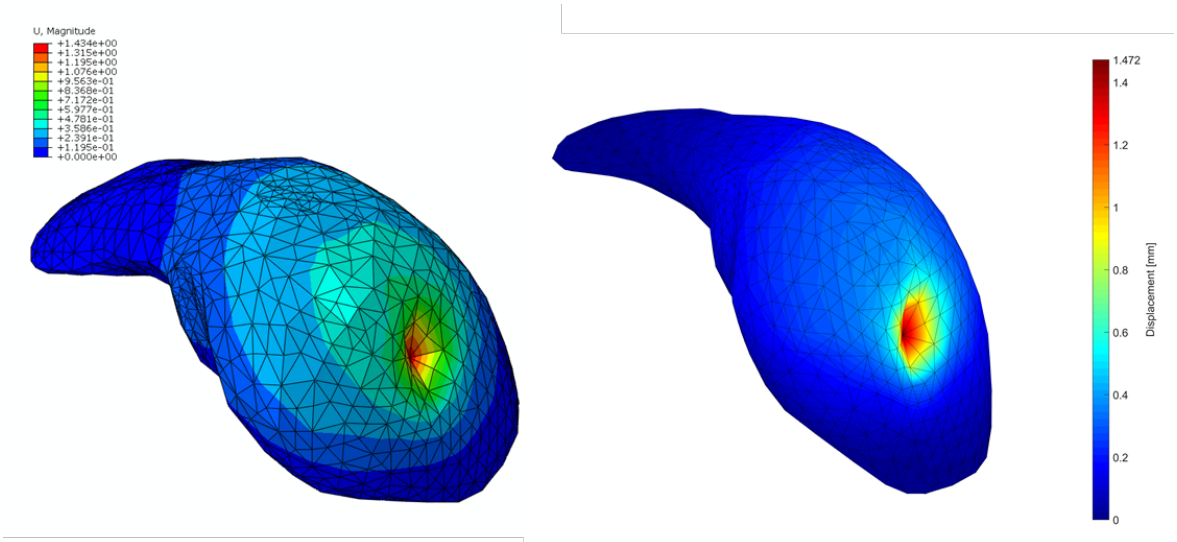

Figure 3-7. Deformed liver model from the FEM (ABAQUS, left) and the KF-FEM (MATLAB, right) – mesh 2

3.5 Conclusion

The proposed algorithm achieved an update frequency of up to 88.9 Hz, that compares favourably to the ~5 Hz computed from the FEM under identical boundary condition and simulation platform. Simulation results show the proposed KF-FEM achieved real-time computational performance without sacrificing accuracy. However, it should be noted that with increase in the number of elements in the mesh that is very probable in complex organs simulations, the update frequency will drop. Table 3-2 shows that the developed KF-FEM calculation frequency dropped ~58.8% between Mesh 1 and Mesh 2 simulations. Although a tiny segment of the geometry is required in computational simulation of small deformations, the graphics interface requires to be present in medical applications. Hence, an optimised hybrid algorithm can be a solution to present the graphics of the non-operation area deformation in combination with the developed KF-FEM in order to avoid sacrificing the computational speed of the operation area.

The FEM does not consider the inaccuracy of the geometrical model concerning the real tissue. Also, due to changes in the material properties of the soft tissue as well as the

boundary conditions, the employed FE model response is not guaranteed. As described in this chapter, the FE model was used as the golden standard model to verify the estimates from the proposed KF-FEM. The uncertainty of the geometrical model requires to be considered in real-time applications. In the next chapter, the project elaborates how to involve the model error in the system equations and validates the results experimentally.

INTENTIONALLY LEFT BLANK

CHAPTER 4

EXPERIMENTAL VALIDATION

INTENTIONALLY LEFT BLANK

4 Experimental Validation

The constitutive methods approaches are fully predictive. In other words, giving known inputs to the system, the output would be entirely determined. It means that any uncertainty in system inputs reflects in the output exactly. This is not a realistic condition, especially for soft tissues with highly varying material properties. Hence, as further presented in sections 2.3 and 2.4, the geometrical model involves error as well as the experimental observations. The KF allows integration of the model error into the system equations, and the novel combination of the KF with the FEM leads to an algorithm that balances the uncertainty of the measurements and the model.

In this chapter, it is explained in the first section of how the model error is inserted into the developed system equation. Then, the procedure to prepare phantom tissue is presented, and test setup, as well as the results of the experiment, are illustrated. The proposed algorithm performance is compared with the experiments and the reference FEM. The outcome is discussed at the end.

4.1 Method

Assume the linear discrete-time dynamic model, Equation (3-2), involves error w as follows,

$$\boldsymbol{x}_{k+1} = \boldsymbol{F}\boldsymbol{x}_k + \boldsymbol{G}\boldsymbol{z}_k + \boldsymbol{w} \tag{4-1}$$

where $\boldsymbol{w}$ is the system noise, assumed to be white Gaussian with known diagonal covariance matrix $\boldsymbol{Q}$, i.e., $\boldsymbol{w}\sim(0, \boldsymbol{Q})$ and $\boldsymbol{E}\left[w_k w_j^T\right] = \boldsymbol{Q}[\delta_{kj}]$. The measurement noise $\boldsymbol{v}$ was taken into account when formulating the proposed system via equation (3-1). It is crucial that the measurement and system noises be uncorrelated, i.e., $\boldsymbol{E}\left[\boldsymbol{v}_k \boldsymbol{w}_j^T\right] = 0$. It is shown that the *priori* covariance of the estimates is influenced by the model error as following (Simon, 2006),

$$P_{k+1}^{-} = \boldsymbol{F} P_k^{+} \boldsymbol{F}^T + \boldsymbol{Q}. \quad (4\text{-}2)$$

The proposed algorithm considers the model error in the estimation by replacing equation (3-4) with (4-2). Hereafter, we call this algorithm the UNC_M.KF-FEM, representing the KF-FEM with an uncertain model. The rest of the procedure operates as described in section 3.1. However, the error of the model requires to be assessed and calculated with the help of experiments. A set of indentation tests is designed and conducted for this purpose.

4.1.1 Specimen Preparation

Silicone is a suitable base material for flexible fabrication of phantom tissues. By using various (Cross-linker: Catalyst) mixing ratios, the elasticity modulus of as high as ~5 MPa is reported in the literature (G. Lamouche et al., 2012; Moser et al., 2016). Adding PDMS (polydimethylsiloxane) oil softens the silicone to achieve elasticity modulus of as low as 10 kPa. However, the material preparation formulations to produce such low elasticities need several weeks to cure if not heated (G. Lamouche et al., 2012). Hence, by choosing an appropriate mixing ratio and fabrication process, it is possible to obtain phantoms with mechanical properties covering a wide range of tissues.

Silicone commercial kits can be purchased from manufacturers. EcoFlex00-30 (Smooth-On) is a highly elastic low modulus silicone kit that is commonly used to mimic human soft tissue behaviour. It includes compound and catalyst, and elasticity modulus of 35~69 kPa can be achieved by following the manufacturer instructions (Jeong, Zhang, Hjort, Hilborn, & Wu, 2016). It cures at room temperature in 4 hours with negligible shrinkage. The low viscosity before cure ensures easy mixing and de-airs the bubbles out of the mould naturally if poured with the constant and uniform flow into the mould.

We followed the manufacturer instructions to obtain tissue with 50 kPa elasticity; however, up to 10% error in the result is expected due to the manual procedure of producing the material. We chose 50 kPa, and not softer, due to the difficulties and the limitation we had

in the size of the samples as well as the small ranges of force that the machine in our experiments could apply. We prepared the samples in blocks of $100 \times 100 \times 20\ mm$; then cut in species of $10 \times 10 \times 5\ mm$ for the indentation test. The manufacturer instruction was followed carefully to achieve a homogeneous phantom with the required elasticity.

4.1.2 Test Setup

We conducted ten indentation tests on the samples made from silicone. The compression machine TMA-Q400 was used in the room temperature for experiments. The samples had the density 1068 kg/m^3 on average. A rigid circular flat-end probe with diameter 2.85 mm was used for indentation. It was assumed that the indenter tip is frictionless, and the force was applied to the centre of the tissue's surface, linearly increasing from 0.01 N to 0.4 N. The loading condition was chosen similar to the literature (Fu & Chui, 2014). The applied force and the observed displacement were recorded, and the experiment results were used to validate the UNC_M.KF-FEM. The force and displacement measurement values obtained from the indentation tests on ten silicone samples are presented in Figure 4-1.

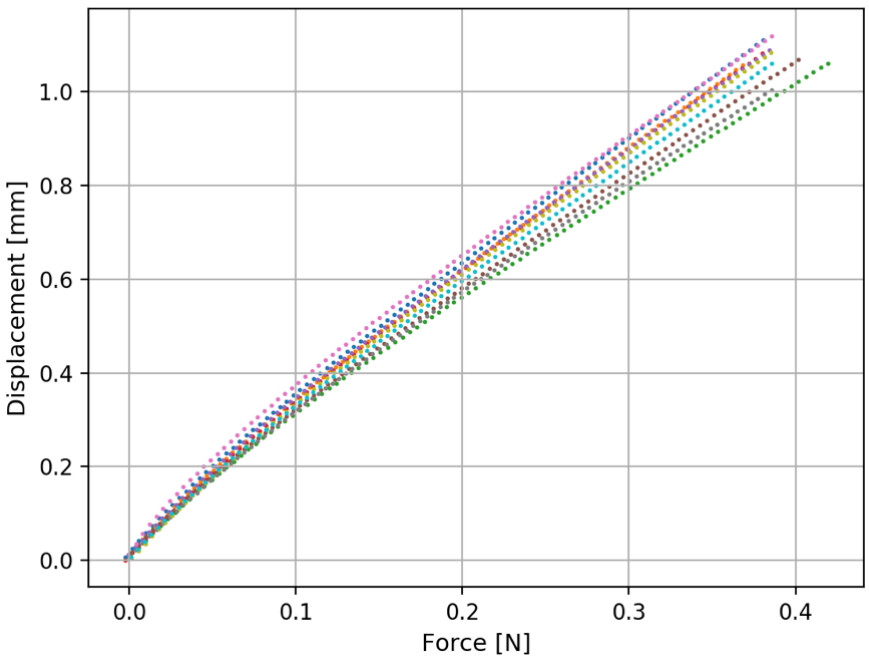

Figure 4-1. Force-displacement measurements from the indentation test on ten silicone samples

4.2 Experiment Results

As earlier stated at the beginning of this chapter, constitutive approaches provide a fully predictive result. In other words, a given known input always ends in the same output from the model. To illustrate this matter, we conducted a one-by-one comparison between the FEM and the UNC_M.KF-FEM given the ten different measurement values obtained from experiments, as shown in Figure 4-2 to Figure 4-6. The material properties and the boundary conditions used in the FEM and KF-FEM are identical. The FEM model with the same size as the sample was created in MATLAB R2015b. The model was discretised into 4941 tetrahedral elements.

It is seen in all ten plots shown in Figure 4-2 to Figure 4-6 that the FEM response under identical boundary conditions and model inputs is constant. But experiment results under the same condition changes moderately at each sample due to the complex behaviour of soft tissue. It is seen that the UNC_M.KF-FEM estimation varies with the help of the available measurements at the time of the simulation. By integrating the potential model error concerning the measures into the system equations, the UNC_M.KF-FEM estimates the displacement in a matter to minimise the error between the estimates and the FEM model versus measurements.

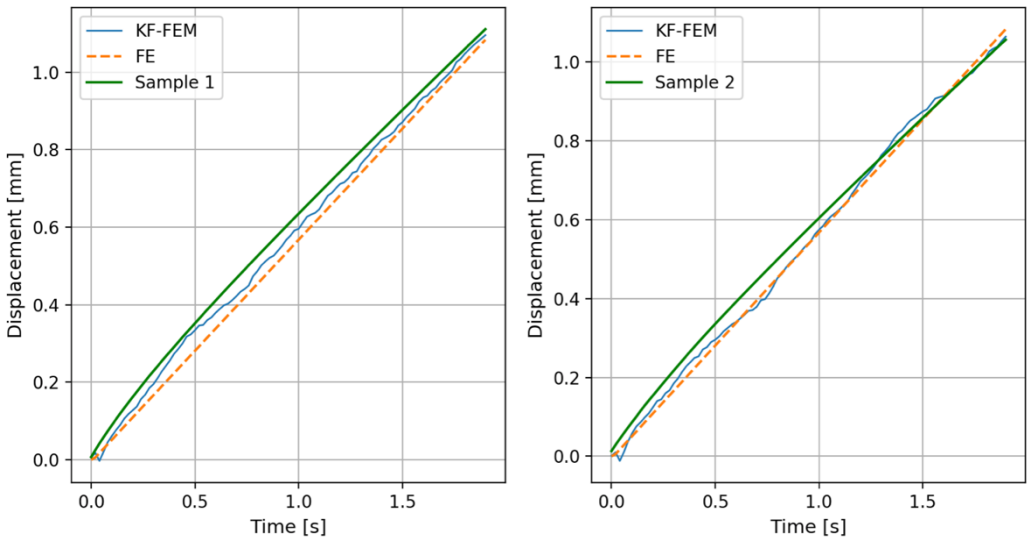

Figure 4-2. The KF-FEM vs. FEM response in comparison with the measurements (samples 1 and 2)

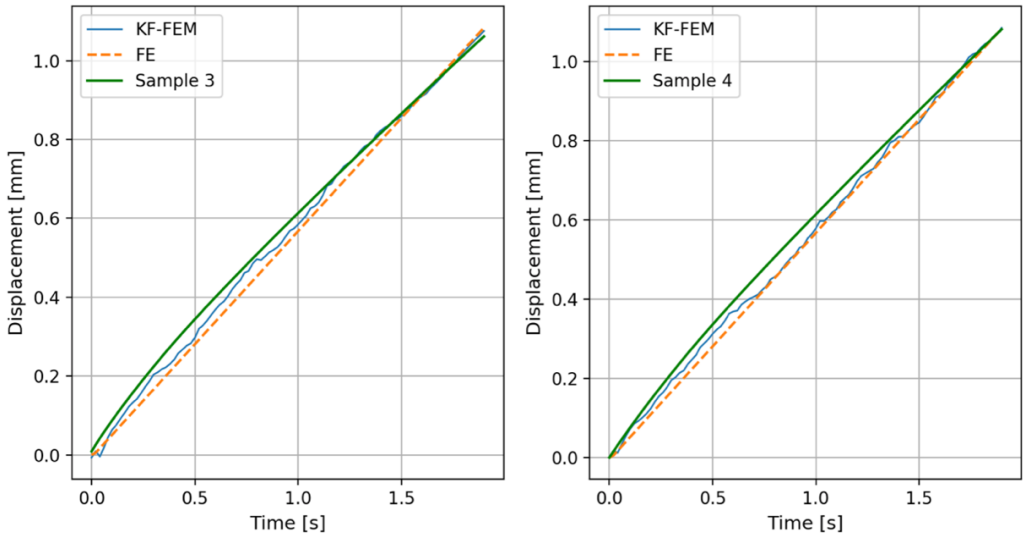

Figure 4-3. The KF-FEM vs. FEM response in comparison with the measurements (samples 3 and 4)

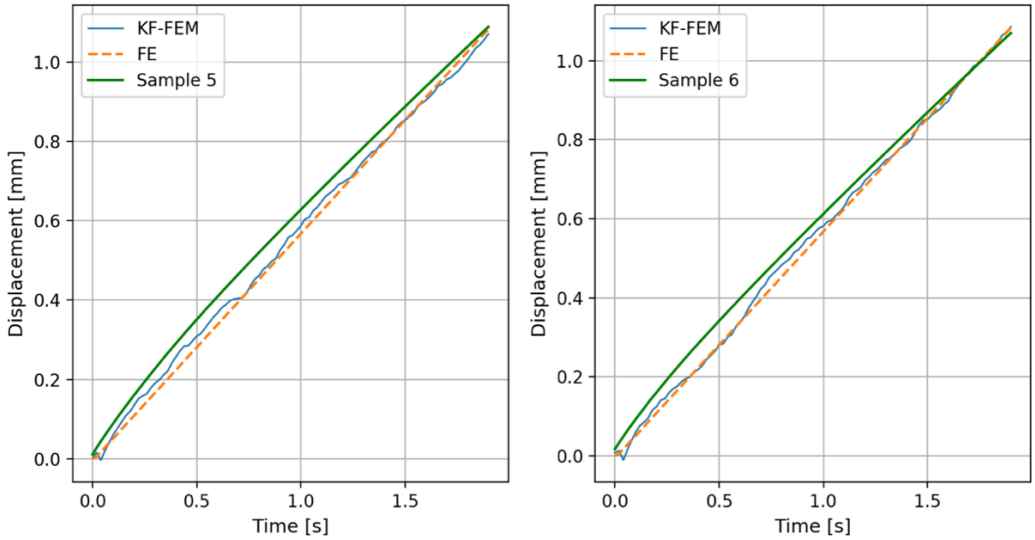

Figure 4-4. The KF-FEM vs. FEM response in comparison with the measurements (samples 5 and 6)

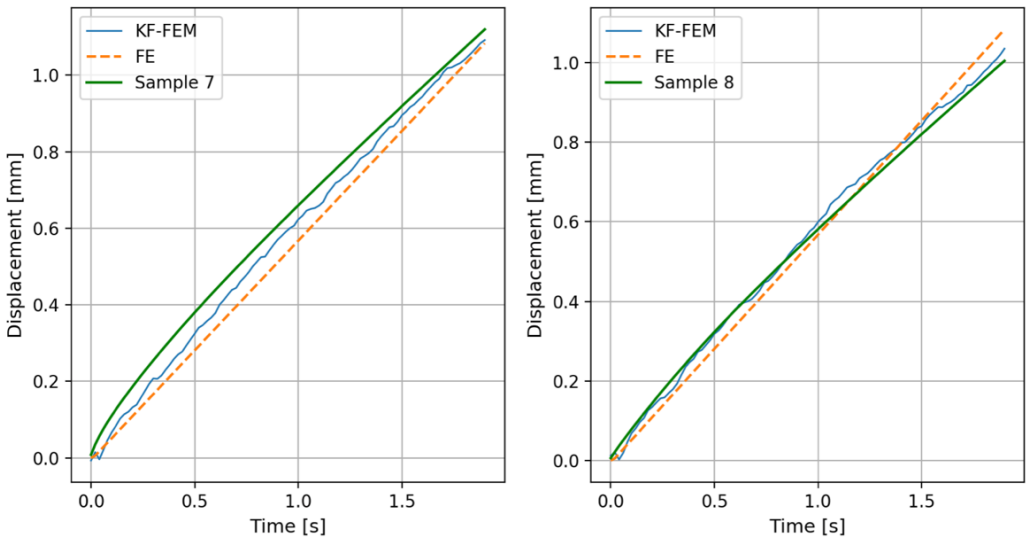

Figure 4-5. The KF-FEM vs. FEM response in comparison with the measurements (samples 7 and 8)

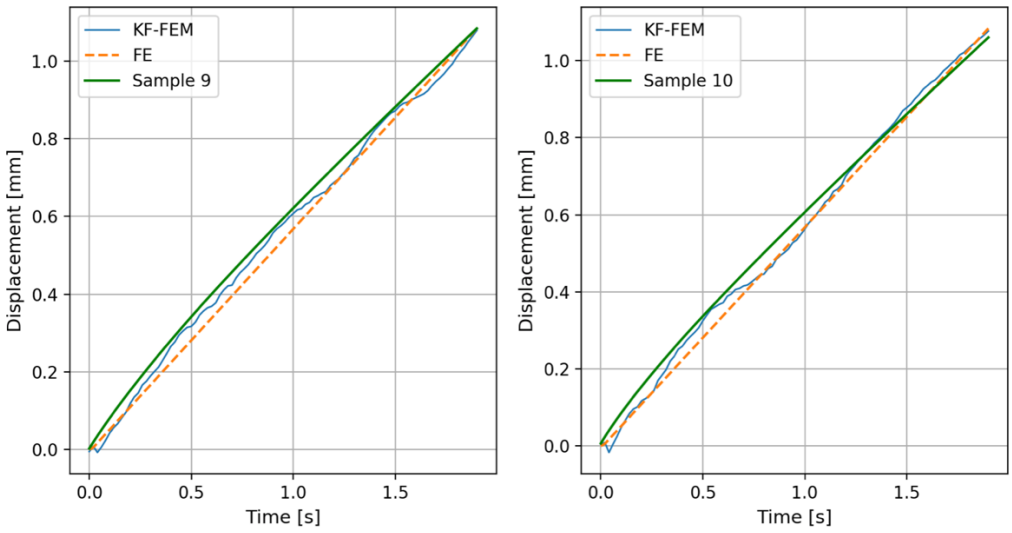

Figure 4-6. The KF-FEM vs. FEM response in comparison with the measurements (samples 9 and 10)

It should be noted that displacement plots obtained from measurements as well as simulated by the FEM, as in Figure 4-2 to Figure 4-6, show a smooth behaviour from the soft tissue. However, these plots cannot be real. The reason is that the measurement sensor flattens measured values according to their update frequency limit. Also, the FEM does not account for human precision in performing tissue manipulation. On the other hand, the noisy displacement estimated by the KF-FEM seems to represent the operation closer to reality. The fluctuations in the estimated displacement are in Microscale, which if a haptic device is used by the operator, the noise will not be sensed by the operator's hand.

4.2.1 Computational Performance

Because of the one-step recursive computational algorithm of the UNC_M.KF-FEM, the computational performance is significantly enhanced in comparison with the FEM. The FEM analysis took 36.2 seconds on average to complete the simulation, but the UNC_M.KF-FEM completed the job in 659 milliseconds on the same computational platform. The computation speed and the equivalent update frequency of both methods is presented in Table 4-1. Further details of the experiments result, as published in Yarahmadian et. al., 2019 is presented in Appendix C.

Table 4-1. Computational performance of the UNC$_M$.KF-FEM vs. the FEM

	FEM	KF-FEM
Computational time (s)	36.2	0.659
Update frequency (Hz)	2.7	145.7

4.2.2 Estimates Accuracy

We calculated the root-mean-square error (RMSE) of the UNC$_M$.KF-FEM versus the FEM concerning the reference measurement from the six samples out of ten with smallest errors. The RMSEs and the calculated average error is shown in Table 4-2. The average error shows less than 0.5% decrease in accuracy from the KF-FEM compared with the employed FEM.

Table 4-2. RMSE (mm) of KF-FEM vs. FEM against measurements at the indenter's tip

	sample 1	sample 2	sample 3	sample 4	sample 5	sample 6	**Avg. error**
FEM	0.049	0.037	0.041	0.034	0.045	0.039	4.08%
KF-FEM	0.054	0.041	0.045	0.039	0.050	0.044	4.55%

The displacement response computed by FEM at four steps of applying the external force from 0.01 to 0.4 N is compared with the median estimate obtained from the KF-FEM and the median measurement. This comparison, accompanied by the standard deviation of measurements and estimates from their medians, is shown in Figure 4-7.

It is seen that the UNC$_M$.KF-FEM result is in good agreement with the experiment result. As can be seen, the UNC$_M$.KF-FEM does not rely on the FEM model result only. It gets advantage from the available measurements as well. Knowing that the FEM model and measurements are both with some extents of inaccuracy, the KF-FEM optimizes the target variable estimates by minimizing the mean square error of estimates. In addition to that, as can be seen from Figure 4-7, the developed method estimates show a smaller deviation from the median of responses in comparison with the measured displacement in the same load condition. In other words, the displacement values computed by the KF-FEM are more consistent than the measured displacements.

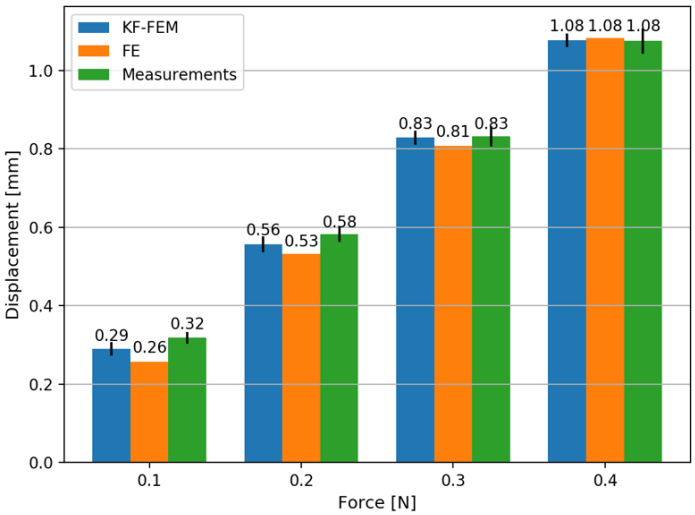

Figure 4-7. The UNC$_M$.KF-FEM vs. Measurement median displacement from ten samples in comparison with the FE model

4.3 Real-life Application

We validated the developed algorithm performance with experiments and presented the results in terms of accuracy and speed in section 4.2. However, the simulations were done under ideal circumstances that the sample material properties were known, and the exact value was used by both FEM and KF-FEM methods.

Human liver becomes stiff as fibrosis spreads out. Sandrin et al. (2003) found out that the elasticity of fibrotic livers varied from 3.35 to 69.1 kPa. (Umut Ozcan, Ocal, Basdogan, Dogusoy, & Tokat, 2011) in a study showed that the liver elasticity is frequency-dependent, and whereas it varied from 10 to 20 kPa in healthy livers, it can vary from 20 to 50 kPa in cirrhotic livers.

The silicon tissues were made with the formulation to have the elasticity 50 kPa. The exact value of the elasticity was used in both FEM and the UNC$_M$.KF-FEM methods. However, in real-life situations, soft tissue's material parameters are highly patient dependent. Besides, diseased tissue might show a different behaviour, especially concerning the stiffness and the scale of the elasticity. To show the significance of the UNC$_M$.KF-FEM in real-life applications, we ran simulations with $E = 45\ kPa$, whereas, the samples had elasticity 50 kPa. In other words, we simulated a situation that the tissue, that is diagnosed with fibrosis, has larger

elasticity than the one used in the FEM, leading to smaller deformations than the FEM prediction. Table 4-3 compares the average error of both solutions against the maximum observed displacement. It is seen by some small uncertainty in the material properties of the tissue, the FEM error increases significantly in comparison with the estimates error from the UNC_M.KF-FEM.

Table 4-3. RMSE (mm) of the UNC_M.KF-FEM and FEM with wrong elasticity against measurements

	sample 1	sample 2	sample 3	sample 4	sample 5	sample 6	**Avg. error**
FEM	0.056	0.082	0.078	0.069	0.065	0.076	7.10%
KF-FEM	0.056	0.056	0.057	0.049	0.057	0.056	5.52%

Compared with the results provided in Table 4-2, the FEM error increased 3.02%, but the KF-FEM error increased 0.97% only. Figure 4-8 compares the displacement estimates from the UNC_M.KF-FEM and the FEM analysis versus the random normal distribution of the measurement values around the mean.

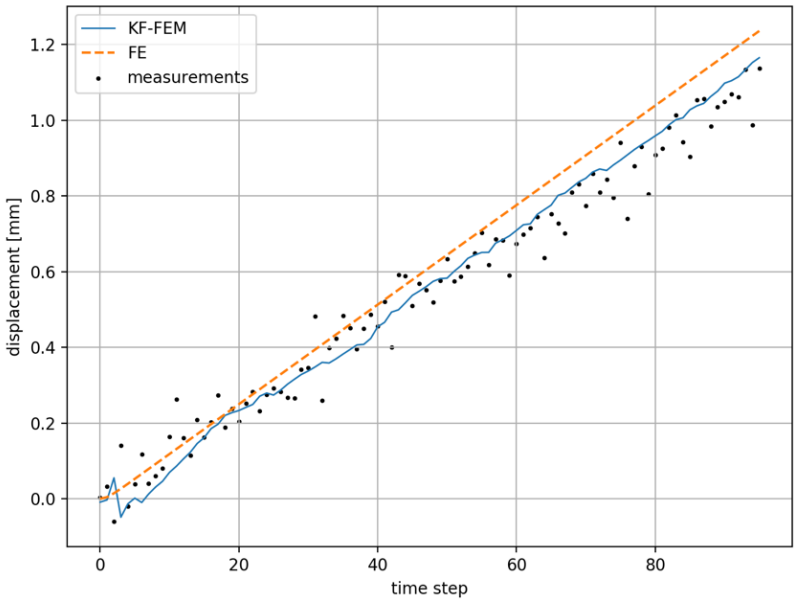

Figure 4-8. Displacement from the uncertain FEM and KF-FEM against experiments

It is seen from Figure 4-8 that the FEM analysis is diverging from the measurements. This is because the reference solution has assumed a softer behaviour from the tissue. But the UNC_M.KF-FEM can balance the estimates between the uncertainty of the model and measurements.

4.4 Conclusion

The developed UNC_M.KF-FEM achieved an update frequency of 145.7 Hz for the deformation of the experimentally tested phantom tissues. Results with the update frequencies above 25 Hz confirm the capability of real-time computational performance of the method. Being capable of involving both measurement and model errors in the system equations, the developed KF-FEM achieved reasonable deformation accuracy compared to the outcome from the FEM. The generated KF-FEM results were more consistent that the measurement, which confirms that the noise of measurement tools should not be ignored in real-time simulations. Furthermore, the experiments confirm that the temporally linearized FEM is reliable within the applied displacement range. Hence, the KF can be employed.

In practice, force values are collected by force sensors, leading to noisy inputs for the system equations. The accuracy of the estimates highly depends on the efficiency of the inputs. Careful considerations are required to account for the system's input uncertainties. In the next chapter, the project addresses the problem of noisy inputs in real-time applications and how to differentiate them from the model error.

CHAPTER 5

MODIFIED ALGORITHM FOR UNCERTAIN SYSTEM INPUTS

INTENTIONALLY LEFT BLANK

5 Modified Algorithm for Uncertain System Inputs

In the last two chapters, a real-time numerical solver was developed and validated through experimental data. Both developed algorithms, KF-FEM and UNC_M.KF-FEM, were able to simulate small deformations of the soft tissue with frequencies of higher than 25 Hz, with the help of direct measurements from the tool-tissue contact area. However, in real-time mechanical problem, the accuracy of the individual results is entirely dependent on the accuracy of the loading inputs that form the boundary and initial conditions.

It was shown in Figure 4-1 that although the experiment setup was constant in all the tests, the force-displacement values measured by the sensors differed. In other words, a constant displacement value (horizontal line in the figure) was obtained from various force values. In the conducted experiments in chapter 4, the observed force from the sensors had noise, but the loading value was considered as a known noiseless input in the simulations. This is a specific disadvantage for practical problems where noisy inputs are unavoidable, and then the time derivatives further exacerbate their effect (Dabnichki, Lauder, Aritan, & Tsirakos, 1997). Also, to fully validate and optimize the predictive power of a computational model one may need to build physical models that control both the inputs and outputs requiring both time and resources (Gardano & Dabnichki, 2006). Figure 5-1 shows the developed KF-FEM in chapter 3, and highlights the modification required to address the uncertain system inputs.

To this purpose, we need to consider the uncertainty of the system input, i.e., the external force in equation (3-21) and modify the developed KF-FEM. A dynamic filtering algorithm is explained in Section 5.1, which is defined as a state estimation problem from noisy input and output. The differential equations of the soft tissue deformation are further modified to meet the requirements of the mentioned algorithm. The estimated displacement from the

modified KF-FEM model (hereafter, UNC$_I$.KF-FEM for the KF-FEM algorithm with uncertain inputs) are verified and compared with the FEM and the developed KF-FEM under identical system input, that is the noisy force.

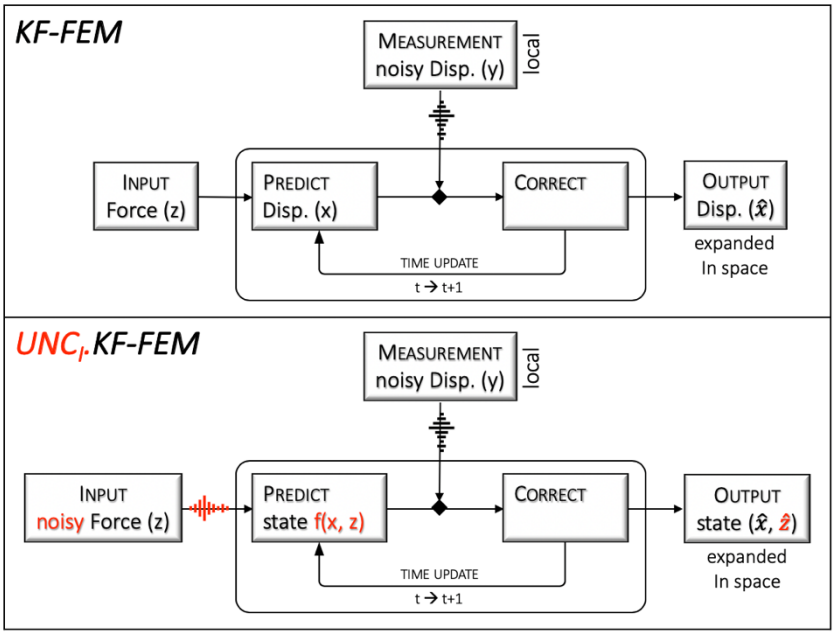

Figure 5-1. The UNC$_I$.KF-FEM algorithm vs. the KF-FEM

5.1 Method

The deterministic discrete-time linear system with time-invariant parameters is considered with a set of measurements as follows,

$$\boldsymbol{x}_{k+1} = \mathbb{A}\boldsymbol{x}_k + \mathbb{B}\boldsymbol{z}_k,$$

$$\boldsymbol{y}_k = \mathbb{C}\boldsymbol{x}_k + \mathbb{D}\boldsymbol{z}_k \tag{5-1}$$

where the system input, $\boldsymbol{z}_k$, and the output, $\boldsymbol{y}_k$, are measured at time point k with the error models

$$z_k^m = z_k + \tilde{z}_k, \quad y_k^m = y_k + \tilde{y}_k. \tag{5-2}$$

The vector of measurement errors is a stationary, white Gaussian noise with positive-definite block diagonal covariance matrix $V = blkdiag(V_{\tilde{z}}, V_{\tilde{y}})$. The target of the defined *noisy I/O model* (equations (5-1) and (5-2)), hereafter modified model, is to find the least square

estimates of the state $\boldsymbol{x}$ from the measured I/O data $\boldsymbol{w}_k^m \coloneqq col(z_k^m, y_k^m)$. The system noise v_1 and the measurement noise v_2 have a joint covariance matrix as follows.

$$\begin{bmatrix} \boldsymbol{Q} & \boldsymbol{S} \\ \boldsymbol{S}^T & \boldsymbol{R} \end{bmatrix} \coloneqq cov(\begin{bmatrix} v_1 \\ v_2 \end{bmatrix} = \begin{bmatrix} -\mathbb{B} & 0 \\ -\mathbb{D} & I \end{bmatrix} \begin{bmatrix} V_{\tilde{z}} & \\ & V_{\tilde{y}} \end{bmatrix} \begin{bmatrix} -\mathbb{B} & 0 \\ -\mathbb{D} & I \end{bmatrix}^T \tag{5-3}$$

Substituting $z_k^m - \tilde{z}_k$ for $\boldsymbol{z}_k$ and $y_k^m - \tilde{y}_k$ for $\boldsymbol{y}_k$ in the system equations (5-1), the process and measurement equations can be written as

$$\begin{aligned} \boldsymbol{x}_{k+1} &= \mathbb{A}\boldsymbol{x}_k + \mathbb{B}\boldsymbol{z}_k^m - \mathbb{B}\tilde{\boldsymbol{z}}_k, \\ \boldsymbol{y}_k^m &= \mathbb{C}\boldsymbol{x}_k + \mathbb{D}\boldsymbol{z}_k^m - \mathbb{D}\tilde{\boldsymbol{z}}_k + \tilde{\boldsymbol{y}}_k \end{aligned} \tag{5-4}$$

where a fake system noise $v_1 \coloneqq -\mathbb{B}\tilde{\boldsymbol{z}}_k$ and measurement noise $v_2 \coloneqq -\mathbb{D}\tilde{\boldsymbol{z}}_k + \tilde{\boldsymbol{y}}_k$ can be introduced into the system. It is shown (AlMutawa, 2012; Markovsky & De Moor, 2005) that the Kalman filter corresponding to the modified system, i.e., equations (5-4), with covariance (5-3) is:

$$\begin{aligned} \boldsymbol{p}_{k+1} &= \boldsymbol{A}_k^{kf}\boldsymbol{p}_k + \boldsymbol{B}_k^{kf}\boldsymbol{w}_k^m, \\ \hat{\boldsymbol{x}}_k &= \boldsymbol{C}_k^{kf}\boldsymbol{p}_k + \boldsymbol{D}_k^{kf}\boldsymbol{w}_k^m \end{aligned} \tag{5-5}$$

where the one-step-ahead prediction, $\boldsymbol{p}_{k+1}$, is defined by the optimal state estimate, $\hat{\boldsymbol{x}}_k$, and the optimal input estimate $\hat{\boldsymbol{z}}_k$. The $\boldsymbol{p}_{k+1}$ can be called the modified state, that is a function of the system state (displacement) and system input (force) calculated as follows,

$$\boldsymbol{p}_{k+1} = \mathbb{A}\hat{\boldsymbol{x}}_k + \mathbb{B}\hat{\boldsymbol{z}}_k. \tag{5-6}$$

The time-variant coefficients of the modified system (5-5) are calculated from

$$\begin{aligned} A_k^{kf} &= \mathbb{A} - K_k\mathbb{C}, \\ B_k^{kf} &= [\mathbb{B} - K_k\mathbb{D} \quad K_k], \\ C_k^{kf} &= I - P_k\mathbb{C}^T(\mathbb{C}P_k\mathbb{C}^T + R)^{-1}\mathbb{C}, \\ D_k^{kf} &= P_k\mathbb{C}^T(\mathbb{C}P_k\mathbb{C}^T + R)^{-1}[-\mathbb{D} \quad I] \end{aligned} \tag{5-7}$$

where the Kalman gain, K_k, and the estimation error covariance, P_k, are calculated from

$$K_k = (\mathbb{A}P_k\mathbb{C}^T + S)(\mathbb{C}P_k\mathbb{C}^T + R)^{-1},$$

$$P_{k+1} = \mathbb{A}P_k\mathbb{A}^T - (\mathbb{A}P_k\mathbb{C}^T + S)(\mathbb{C}P_k\mathbb{C}^T + R)^{-1}(\mathbb{A}P_k\mathbb{C}^T + S)^T + Q. \quad (5\text{-}8)$$

By knowing the one-step-ahead prediction, $\boldsymbol{p}_{k+1}$, and the optimal state estimate, $\widehat{\boldsymbol{x}}_k$, from equation (5-5), we can calculate the optimal input estimate, $\hat{\boldsymbol{z}}_k$, at each time step. In fact, equation (5-6) and the modified Kalman filter (5-5) imply that

$$\hat{\boldsymbol{z}}_k = \mathcal{s}_k\boldsymbol{p}_k + \mathcal{m}_k\boldsymbol{w}_k^m \quad (5\text{-}9)$$

where $\mathcal{s}_k \coloneqq -V_{\tilde{z}}\mathbb{D}^T(\mathbb{C}P_k\mathbb{C}^T + R)^{-1}\mathbb{C}$, and $\mathcal{m}_k \coloneqq$ $[I - V_{\tilde{z}}\mathbb{D}^T(\mathbb{C}P_k\mathbb{C}^T + R)^{-1}\mathbb{D} \quad -V_{\tilde{z}}\mathbb{D}^T(\mathbb{C}P_k\mathbb{C}^T + R)^{-1}]$. The optimal output estimate is calculated from

$$\widehat{\boldsymbol{y}}_k = \left(\mathbb{C}C_k^{kf} + \mathbb{D}\mathcal{s}_k\right)\boldsymbol{p}_k + \left(\mathbb{C}D_k^{kf} + \mathbb{D}\mathcal{m}_k\right)\boldsymbol{w}_k^m. \quad (5\text{-}10)$$

With the set of equations from (5-1) to (5-10), we have an explicit solution for the UNC$_I$.KF-FEM. The proposed UNC$_I$.KF-FEM operates in a similar way to the developed KF-FEM in chapter 3 by predicting one-step-ahead the modified state $\boldsymbol{p}_{k+1}$ and the optimal system state $\widehat{\boldsymbol{x}}_k$ with equation (5-5). The optimal system input $\hat{\boldsymbol{z}}_k$ is then calculated from equation (5-9), and finally the modified state $\boldsymbol{p}_{k+1}$ in the next step is corrected using equation (5-6). After formulating the algorithm, the block diagram of the proposed UNC$_I$.KF-FEM is provided in section 5.2.2.

5.2 Application in Soft Tissue Deformation

To apply the proposed UNC$_I$.KF-FEM in soft tissue's deformation applications, we require to reformulate the material equilibrium equation into the form of the proposed method set of equations (5-1). The measurement and system input equations should be formulated to meet the criteria mentioned as requirements of the set of equations (5-2).

5.2.1 FEM Formulation for the UNC$_I$.KF-FEM

Using the explicit Newmark method with the equilibrium differential equations, the displacement of the soft tissue was introduced as the system state in chapter 3. Then the state equation was reformulated as equation (3-21) to meet the requirements of the proposed KF-FEM. However, by introducing the system input noise into the algorithm, the state equation (3-21) requires modification to meet the essential criteria of the proposed UNC$_I$.KF-FEM, as explained in section 5.1.

First, the measurement errors of the input and output must be uncorrelated. Second, the input measurement should not be state-dependent in order to the system equation being solvable by the modified KF. In other words, the displacement measurement error should be independent from the displacement value. It should be noted that the system input is defined as $\boldsymbol{z}_{k+1} = [\dot{\boldsymbol{u}}_k \quad \ddot{\boldsymbol{u}}_k \quad \boldsymbol{f}_{k+1}]^T$ in the state equation (3-21), which involves the nodal velocity, acceleration, and the external force. The input measurement error comes only from the force measurement that is uncorrelated to the output measurement, i.e., displacement measurement. Hence, the first criterion, as mentioned above, is met with the proposed FEM state equation in Chapter 3. However, the second criterion, that states the independency of the input measurement error and the system state, i.e. the displacement, is not met.

In the small ranges of displacement made in a short period, the dominant driving input is the external force. Hence, the nodal velocity and acceleration derived from the movement have a negligible effect on the system state, that is the one-step-ahead prediction of displacement. So, the system input can be modified and defined as $\boldsymbol{z}_{k+1} \coloneqq \boldsymbol{f}_{k+1}$, that is independent of the system state and meets the second criterion of the UNC$_I$.KF-FEM.

By ignoring the damping effect in the small deformations in a short time simulation as suggested in literature (Taylor et al., 2008), the modified FEM-based system equations are as follows.

$$\boldsymbol{u}_{k+1} = 4\boldsymbol{M}(4\boldsymbol{M}/\Delta t^2 + \boldsymbol{K})^{-1}/\Delta t^2\, \boldsymbol{u}_k + (4\boldsymbol{M}/\Delta t^2 + \boldsymbol{K})^{-1}\boldsymbol{f}_{k+1},$$

$$\boldsymbol{y}_k = \mathbb{C}\boldsymbol{u}_k \tag{5-11}$$

The nodal displacement at the tool-tissue contact area is considered as the output, $\boldsymbol{y}_k$, and so, the output measurement does not include the external force as a variable. Hence, the measurement matrices are defined as $\mathbb{D} = 0$ and $\mathbb{C}$ to be a binary matrix that maps the measured displacement to the global vector of displacement. Comparing the modified state equation (5-11) with equation (5-1) implies that:

- The system input is $\boldsymbol{z}_k = \boldsymbol{f}_{k+1}$ with the control matrix $\mathbb{B} = (4M/\Delta t^2 + K)^{-1}$,
- The system state is $\boldsymbol{x}_{k+1} = \boldsymbol{u}_{k+1}$ with the transition matrix $\mathbb{A} = 4M.\mathbb{B}/\Delta t^2$,
- $\mathbb{D} = 0$, and $\mathbb{C}$ is the binary measurement matrix.

The modified model parameters are calculated from equations (5-7) and (5-8), and will be used in the modified system set of equations (5-5) to calculate the optimal input and output estimates from equations (5-9) and (5-10).

5.2.2 The Modified Algorithm

With the method elaborated in sections 5.1 and 5.2.1, we have the solution for deformation estimation using noisy force and displacement measurements. Similar to the developed KF-FEM in chapter 3, some equations are independent of the measurements, and thus, can be calculated before the simulation runs. In real-time applications, this step is sometimes called the *offline* stage. Figure 5-2 shows the block diagram of the computation in the offline stage of the proposed UNC$_I$.KF-FEM.

The calculation of the offline stage is an essential step in the real-time capability of the proposed algorithm. By pre-assessment of the offline stage and the convergence of the estimation error covariance towards the zero, the model is ready to run in real time. The I/O measurements ($\boldsymbol{f}_{k+1}$, $\boldsymbol{y}_{k+1}$), the modified system coefficients (A_k^{kf}, B_k^{kf}, C_k^{kf}, D_k^{kf}) and optimal input coefficients ($\mathcal{s}_k$, $\mathcal{m}_k$), both from the offline stage are used to predict the modified

state ($\boldsymbol{p}_{k+1}$). Then, the optimal state ($\widehat{\boldsymbol{x}}_k$), input estimates ($\widehat{\boldsymbol{z}}_k$), and the output estimates ($\widehat{\boldsymbol{y}}_k$) are calculated in the correction step. Figure 5-3 shows the real-time stage block diagram of the proposed UNC$_I$.KF-FEM.

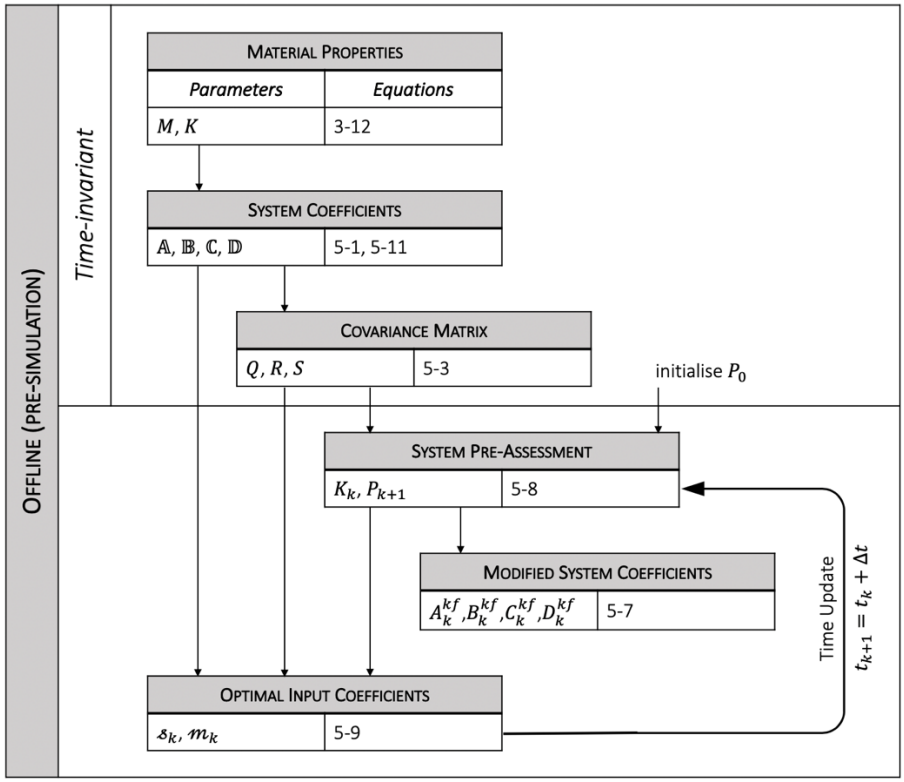

Figure 5-2. The UNC$_I$.KF-FEM offline stage

5.3 Performance Evaluation and Comparison

A cubic model of size $8 \times 8 \times 3\ mm$ is simulated to evaluate the performance of the modified algorithm with noisy I/O. The first order tetrahedral element is used to discretize the cube into 2062 elements compound of 549 nodes. Material properties are the same as properties as explained in section 3.4. It is assumed that the cube sits immobilized on its largest surface. A circular flat-end indenter with radius $2\ mm$ applies force to the centre of the top surface (hereafter, the observation point) linearly increasing from 0 to $0.1\ N$. For the comparison purposes, the FEM was carried out with Abaqus 6.14 to derive the displacement at the observation point. The displacement values from the FEM generated with Abaqus are taken as gold standard values.

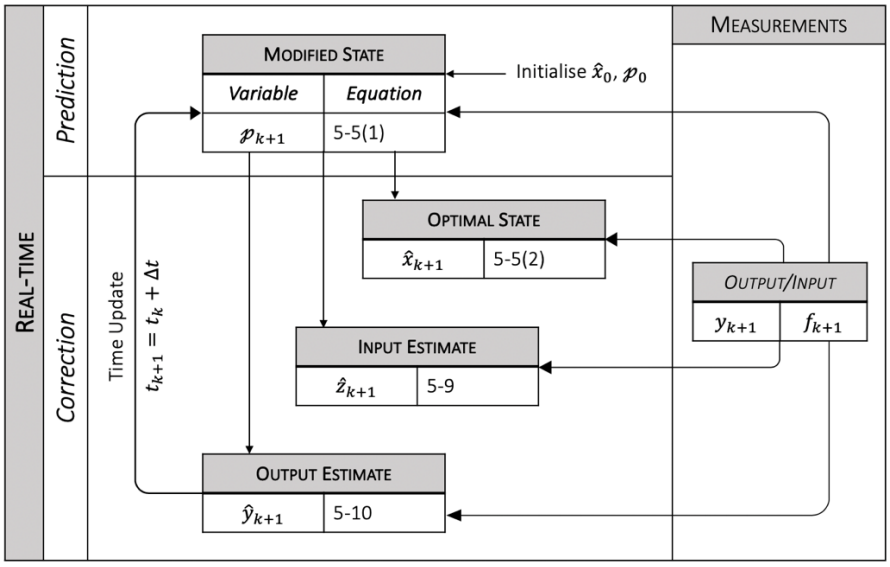

Figure 5-3. The UNC$_I$.KF-FEM real-time stage

5.3.1 Initial Error Recognition

Noisy input and output are generated artificially by adding zero-mean Gaussian noise to the gold standard force and displacement values of the FEM at the observation point. As stated in equation (5-2), the measurement error in the UNC$_I$.KF-FEM method is a two-element vector representing the system output and input errors, $\tilde{y}_k$ and $\tilde{z}_k$ respectively. Although the I/O errors are independent, the various combination of the errors results in different capacities of noise filtration via the proposed algorithm.

To find the optimum measurement error covariance, we formed a 11×11 grid of measurement errors in the range of the artificially generated noise magnitude (see Figure 5-4). In Figure 5-4, the horizontal axes are the input and output (force and displacement respectively) measurement error covariances, and the vertical axis shows the combined filtered noise. The simulation was run with initial V_z and V_y as shown at each grid point. Then the combined filtered noise from the measured force and displacement obtained by the developed UNC$_I$.KF-FEM was calculated and shown as the third dimension of Figure 5-4. This process was repeated for every grid point, leading to 121 runs. The maximum filtered noise (z value) was figured out from the plotted surface, and the x and y values of that specific point were considered as the

optimised initial measurement error covariance in that range. By moving the grid values towards the maximum filtered noise (as shown in steps 2 and 3 of Figure 5-4), we repeated this process two more times. In other words, the simulation was run 363 times in total to find the optimum initial value of the I/O error covariances. Figure 5-4 illustrates the procedure of finding the optimum measurement error covariance. The error covariances with the maximum combined filtered noise, as shown with the coordinate box in stage 3 of Figure 5-4, were selected as the initial value of the measurement error covariances.

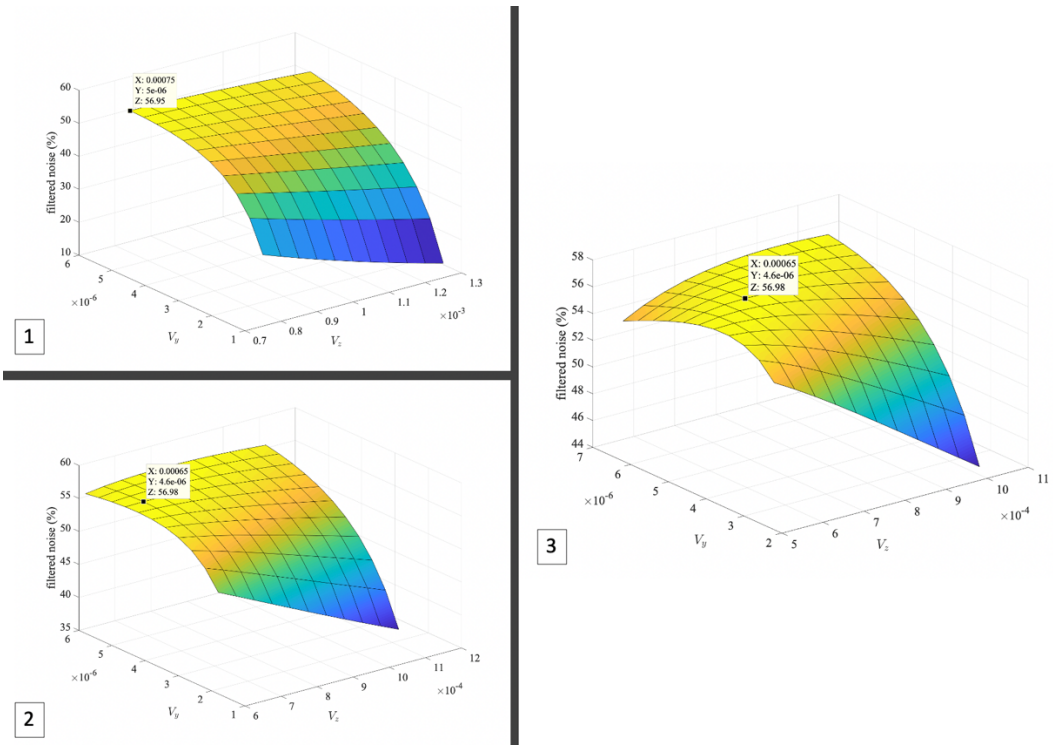

Figure 5-4. Initialisation of the measurement error covariance

5.3.2 Simulation Results

5.3.2.1 Computation speed.

In order to calculate the update frequency of the proposed UNC$_I$.KF-FEM, the total computation time of each simulation out of 363 runs was calculated and divided by the number of time steps in the simulation. The average computation time of each time step by the UNC$_I$.KF-FEM was 0.0076 seconds. Hence, the update frequency is approximately 131.6 Hz that is significantly larger than the target 25 Hz.

5.3.2.2 Deformation accuracy.

Figure 5-5 compares the displacement values at the observation point from the FEM with noiseless input (i.e., the external force) with the simulation outcome from three other models. The first model uses the FEM given the noisy force. The second and third model use the developed KF-FEM and its modified version, respectively, given the same noisy force as the first model.

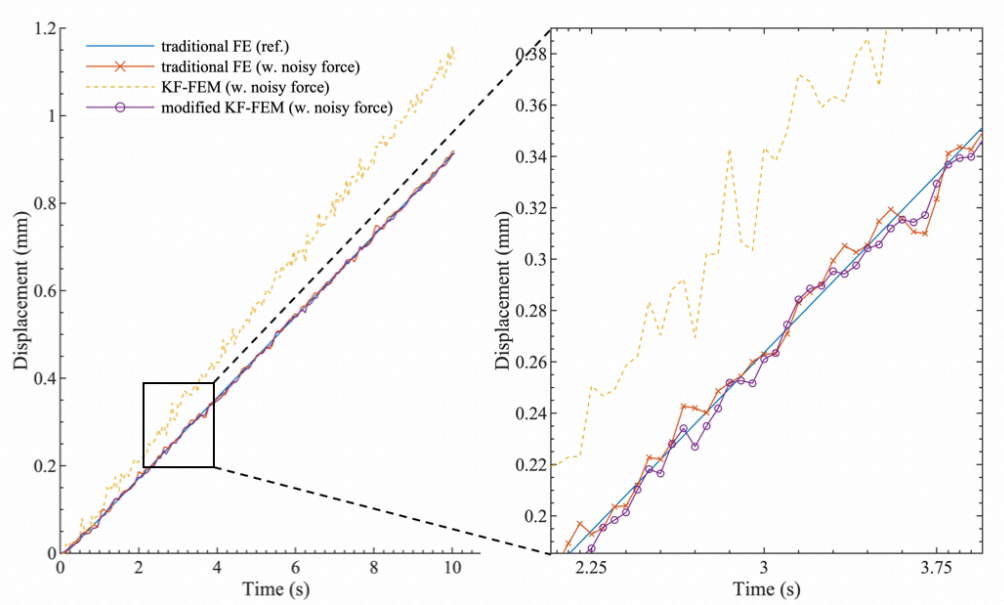

Figure 5-5. Comparing displacement values from the developed KF-FEM and its modified algorithm with the FEM

It can be seen from Figure 5-5 that the estimated displacement by the modified KF-FEM (the purple line) is more accurate than the standard developed KF-FEM (the yellow dash line). This is because the KF-FEM either takes the noisy force as the actual values and so, reflects the force error in displacement estimates, or adds the force error to the model error and thus, accounts the force noise as the error of the model and diverges from the FEM calculations. Besides, the classic FEM given the noisy force (the red line) replicates the input error in the outcome, that is the displacement. Inevitably the FEM reproduces the force error in the displacement. The initial developed KF-FEM takes force uncertainty as a system error and corrects the result from the state equation towards the obtained measurements. However, the

proposed UNC$_I$.KF-FEM does not compromise the reliability of the model by incorporating the noise of the applied force measurement.

The normalised error percentage of the measurements, the FEM with noisy inputs, and the UNC$_I$.KF-FEM with reference to the golden FEM is calculated from $e_N = (u_i - u_{FEM})/u_{max,FEM} \times 100$ for $u_i = u_{meas.}$ & $u_{noisy.FEM}$ & $u_{UNCI.KF-FEM}$. Then, the standard deviation of the obtained errors, e_N, is calculated to evaluate the consistency and reliability of the discussed methods estimates. (see Table 5-1). Results showed 23.6% improvement in estimates accuracy of the proposed UNC$_I$.KF-FEM compared to the FEM with noisy input force. Also, the UNC$_I$.KF-FEM filtered 58.1% of the measurement noise. In addition to that, the normalised error standard deviation of the discussed solution in a random point, in which measurement is not available, is calculated and presented in Table 5-1. It is seen that displacement estimates with 31.3% higher accuracy than the FEM with respect to the gold values are achieved.

Table 5-1. The models normalized error [%] standard deviation

	Observation point	Random point
noisy displacement	1.142	-
FEM w. noisy force	0.6265	0.6265
UNC$_I$.KF-FEM	0.4787	0.4302

5.4 Conclusion

The proposed algorithm achieved its two main goals. The update frequency of the deformation estimation is improved from around 3~5 Hz for the FEM to approximately 131 Hz for the UNC$_I$.KF-FEM within the same geometrical domain. The proposed UNC$_I$.KF-FEM not only incorporated real-time measurements to enhance the computational process of displacement estimation but also reduced the effect of the error in the measurements. Around 60% of the noise in the displacement measurement was filtered by the UNC$_I$.KF-FEM. Further to this, the UNC$_I$.KF-FEM could differentiate the input uncertainty from the system error, leading to more accurate estimates compared to the FEM with the noisy boundary forces.

Further research should aim to relax the requirement for linear elastic behaviour, i.e., to expand the method beyond small deformations. The next chapter is focused on large nonlinear deformation of soft tissues.

CHAPTER 6

LARGE NONLINEAR DEFORMATIONS

INTENTIONALLY LEFT BLANK

6 Large Nonlinear Deformations

The behaviour of biological soft tissues is well known to be nonlinear, hence much probable to undergo large displacements in any medical application that the tissue deformation is involved. Through chapters 3 to 5, this project has developed a real-time optimal numerical solver that benefits from the accuracy and realistic approach of the FEM, combined with a filtering algorithm that employs direct measurements to enhance the computational performance of the soft tissue deformation estimation. However, simulation results were verified and experimentally validated within the small linear scale of deformations. Hence, the incorporation of nonlinear soft tissue deformation is needed.

This chapter combines the Total Lagrangian Explicit Dynamics (TLED) with the optimal estimator Kalman filter. We've called this combination the NL_{TL}.KF-FEM. The employment of the TLED approach in the NL_{TL}.KF-FEM makes calculations possible in local 3-dimensional finite elements of the spatial domain, leading to improved computational performance. As further explained in the following sections, the equilibrium differential equations need modification to suit the system equations of the proposed NL_{TL}.KF-FEM. Besides, advanced programming techniques, such as N-dimensional arrays and data structures as further will be explained in section 6.4, are used to avoid slow iterative processes of computation in the mesh element level.

6.1 Total Lagrangian Explicit Dynamics

Computing the deformation of soft tissue requires efficient integration of time into the dynamic equation of equilibrium. In explicit FEM, the central difference method is used to calculate the acceleration at the beginning of the governing equation, then to determine the unknown nodal displacement. Total Lagrangian Explicit Dynamics (TLED) approach

eliminates the requirement for iteration at each time step, leading to an efficient algorithm for real-time applications (Miller et al., 2007). An overview of the TLED algorithm, as described by Taylor et al. (2008), is presented in this section.

6.1.1 Displacement-based Framework

We study the deformation of the target tissue through the displacement of material points in the body domain. It is assumed that the external loads and boundary conditions are well defined, and the motion of the body is studied in a fixed global Cartesian coordinate system. The coordinate of a material point is given by ${}^{t}x$, and the displacement vector is given by ${}^{t}\boldsymbol{u}$ at time point t. The *deformation gradient* tensor is calculated from

$$ {}^{t}_{0}X_{ij} = \partial\ {}^{t}x_i / \partial\ {}_{0}x_j \tag{6-1} $$

where the Latin right subscript, ranging from 1 to 3 in three dimensions, indicates the tensor components; the left superscript is the configuration in which the quantity occurs, and the left subscript is the configuration with respect to which the quantity occurs. As can be seen from equation (6-1), in the Total Lagrangian method, the deformation is calculated concerning the undeformed status. From the deformation gradient, the *Right Cauchy-Green deformation* tensor can be written as

$$ {}^{t}_{0}\boldsymbol{C} = {}^{t}_{0}\boldsymbol{X}^{T}\,{}^{t}_{0}\boldsymbol{X} \tag{6-2} $$

where ${}^{t}_{0}\boldsymbol{X}^{T}$ is the transpose of the deformation gradient tensor, and subsequently the *Green-Lagrange strain* tensor ${}^{t}_{0}\boldsymbol{E}$ is calculated from

$$ {}^{t}_{0}\boldsymbol{E} = \frac{1}{2}({}^{t}_{0}\boldsymbol{C} - I). \tag{6-3} $$

An appropriate stress measure is required for use with the Green-Lagrange strain. The *Cauchy stress* tensor $\boldsymbol{\sigma}$, also known as true stress tensor, is used for stress analysis of material bodies undergoing small deformations. For large deformations, other measures of stress such as *Piola-Kirchhoff stress* tensor are required. In the Total Lagrangian method, as stated by

Taylor et al. (2008), the stress measure that consolidates with Green-Lagrang strain is the second Piola-Kirchhoff stress tensor ${}_0^t\boldsymbol{S}$, calculated from

$$ {}_0^t\boldsymbol{S} = {}^tJ\, {}_t^0\boldsymbol{X}\, {}^t\boldsymbol{\sigma}\, {}_t^0\boldsymbol{X}^T \tag{6-4} $$

where ${}^tJ = \det({}_0^t\boldsymbol{X})$ is the Jacobian determinant, ${}_t^0\boldsymbol{X} = ({}_0^t\boldsymbol{X})^{-1}$ is the inverse of the deformation gradient tensor, and ${}^t\boldsymbol{\sigma}$ is the Cauchy stress tensor at time t.

6.1.2 Finite Element Solution

The fundamental equilibrium equation for the three-dimensional behaviour of a solid is called principle of virtual work (also known as virtual displacements). In the Total Lagrangian method, the equilibrium equation is written as

$$ \int_{0V} {}_0^tS_{ij}\delta\, {}_0^tE_{ij}\, d\, {}^0V = \int_{0V} {}_0^tf_i^B \delta u_i\, d\, {}^0V + \int_{0S_f} {}_0^tf_i^S \delta u_i^S\, d\, {}^0S \tag{6-5} $$

where the left- and right-hand sides of the equation represent the internal and external virtual works, respectively, performed over the undeformed configuration. $\delta\, {}_0^tE_{ij}$ are the strain variations corresponding to virtual displacements δu_i, ${}_0^tf_i^B$ are body forces, and ${}_0^tf_i^S$ are surface tractions with corresponding displacement δu_i^S.

The body domain is divided into a finite number of elements with unknown nodal displacements, and the relevant quantities are interpolated within each element using appropriate shape functions. By assembling elements into a global formulation, the equilibrium equation can be written as

$$ \boldsymbol{M}\ddot{\boldsymbol{u}} + \boldsymbol{C}\dot{\boldsymbol{u}} + \boldsymbol{K}(u)\boldsymbol{u} = \boldsymbol{r} \tag{6-6} $$

where $\dot{\boldsymbol{u}}$ is the first time-derivative of displacement, i.e., the velocity; $\boldsymbol{r}$ represents the externally applied load; $\boldsymbol{M}$ and $\boldsymbol{C}$ are the (constant) mass and damping matrices, respectively, and $\boldsymbol{K}(u)$ is the stiffness matrix that is nonlinearly dependent on global nodal displacements.

6.1.3 Time Integration

A numerical time integration scheme is required to find the equilibrium position at each time point. The explicit approach of the Central Difference method eliminates the need for iterations in each time step. Using the Central Difference method, the stiffness term in equation (6-6) can be calculated from

$$ {}^{t}\boldsymbol{K}(u)\ {}^{t}\boldsymbol{u} = \sum_{e}\ {}^{t}\boldsymbol{F}^{(e)} \tag{6-7} $$

where ${}^{t}\boldsymbol{F}^{(e)}$ is the global nodal force contribution due to stresses in element e at time t. For a given element ${}^{t}F$ is computed from

$$ {}^{t}\boldsymbol{F} = \int_{{}^{0}V} {}_{0}^{t}\boldsymbol{B}^{T}\ {}_{0}^{t}\widehat{\boldsymbol{S}}d\ {}^{0}\boldsymbol{V} \tag{6-8} $$

where ${}_{0}^{t}B$ is the strain-displacement matrix, $\widehat{\boldsymbol{S}} = [S_{11}\quad S_{22}\quad S_{33}\quad S_{12}\quad S_{23}\quad S_{13}]^{T}$ is the vector from six independent components of the symmetric *second Piola-Kirchhoff stress* tensor, and ${}^{0}V$ is the initial volume of the element. It should be noted that the stiffness matrix $\boldsymbol{K}(u)$ does not need to be assembled at each time step as the nodal force contribution can be calculated at the element level. This feature is a decisive factor over implicit methods and enhances computational performance significantly. Two independent equations of the Central Difference method are

$$ \begin{aligned} {}^{t+\Delta t}\boldsymbol{u} &= {}^{t}\boldsymbol{u} + \Delta t\ {}^{t}\dot{\boldsymbol{u}} + \Delta t^{2}\ {}^{t}\ddot{\boldsymbol{u}}/2, \\ {}^{t+\Delta t}\dot{\boldsymbol{u}} &= {}^{t}\dot{\boldsymbol{u}} + \Delta t\ {}^{t}\ddot{\boldsymbol{u}} + \Delta t({}^{t+\Delta t}\ddot{\boldsymbol{u}} + {}^{t}\ddot{\boldsymbol{u}})/2 \end{aligned} \tag{6-9} $$

where Δt is the time increment. By inserting the stiffness term from equation (6-8) and the computed velocity and acceleration from the set of equations (6-9) in equation (6-6), nodal displacement at the next time point can be calculated from

$$ {}^{t+\Delta t}\boldsymbol{u}_{i} = \frac{{}^{t}R_{i} - {}^{t}F_{i} + 2M_{ii}\ {}^{t}\boldsymbol{u}_{i}/\Delta t^{2} + (C_{ii}/2\Delta t - M_{ii}/\Delta t^{2})\,{}^{t-\Delta t}\boldsymbol{u}_{i}}{C_{ii}/2\Delta t + M_{ii}/\Delta t^{2}}. \tag{6-10} $$

Explicit methods, such as the Central Difference method are conditionally stable. Time increment Δt must be smaller than the critical value $\Delta t_{cr} = L_{e}/c$. L_{e} is the smallest

characteristic element length, and the dilatational wave speed of the material, c, is calculated from

$$c = \sqrt{\frac{E(1-\nu)}{\rho(1+\nu)(1-2\nu)}} \tag{6-11}$$

In large nonlinear analyses, smaller time increments should be considered as Δt_{cr} changes with deformation.

6.1.4 Element Nodal Forces

Referring to equation (6-10), matrices M and C are constant so can be precomputed. The external load $\boldsymbol{r}$ is the input of the system so is available at each time step. The main computational effort in the elaborated process is to calculate the elements nodal force, ${}^{t}F$, at each time step.

6.1.4.1 The strain-displacement matrix.

The strain-displacement matrix ${}^{t}_{0}B$ depends on the geometry of the body domain. Hence, in large deformations, i.e., geometrically nonlinear deformations, ${}^{t}_{0}B$ varies in time and should be calculated at each time step. The strain-displacement matrix can be updated at each time step using the stationary matrix ${}^{0}B$ and the deformation gradient tensor as follows.

$${}^{t}_{0}\boldsymbol{B}^{(a)} = {}^{0}\boldsymbol{B}^{(a)}\,{}^{t}_{0}\boldsymbol{X}^{T}. \tag{6-12}$$

where the right superscript, (a), denotes that the a^{th} submatrix of the strain-displacement matrix, that (a) ranges from 1 to the N number of nodes in each element. The stationary submatrices are calculated from the spatial derivatives of the element shape functions h as follows.

$${}^{0}\boldsymbol{B}^{(a)} = \begin{bmatrix} h_{a,1} & 0 & 0 & h_{a,2} & 0 & h_{a,3} \\ 0 & h_{a,2} & 0 & h_{a,1} & h_{a,3} & 0 \\ 0 & 0 & h_{a,3} & 0 & h_{a,2} & h_{a,1} \end{bmatrix}^{T} \tag{6-13}$$

where $h_{a,i} = \partial h_a / \partial\ {}^0x_i$ for $i = 1, 2, 3$. It is seen that the spatial derivatives of the shape functions are calculated in regard to the initial configuration of the geometry. Hence, the stationary strain-displacement matrix can be precomputed from equation (6-13).

6.1.4.2 Stress tensor.

The stress tensor results from the differentiation of the strain energy density function (SEDF) with respect to the Green-Lagrange strain tensor. Several energy functions have been proposed for the soft tissue. In this work, we use the hyperelastic neo-Hookean model, that the stress components can be calculated from

$$ {}^t_0\sigma_{ij} = \mu\left(\delta_{ij} - {}^t_0C^{-1}_{ij}\right) + \lambda\ {}^tJ(\ {}^tJ - 1){}^t_0C^{-1}_{ij}. \tag{6-14}$$

where μ and λ, are calculated from

$$\mu = E/2(1+\nu),$$

$$\lambda = E\nu/(1+\nu)(1-2\nu). \tag{6-15}$$

It can be seen from equation (6-14) that the computation of element stresses at each time step requires the calculation of deformation tensor ${}^t_0C$ from equation (6-2). Hence, deformation gradient tensor ${}^t_0X$ should be obtained beforehand at each time step. ${}^t_0X$ can be calculated from

$$ {}^t_0\boldsymbol{X} = {}^t_0\partial \boldsymbol{U}_x + \boldsymbol{I} \tag{6-16}$$

where I is the Identity matrix, and ${}^t_0\partial \boldsymbol{U}_x$ is a matrix of element displacement derivatives calculated from ${}^t_0\partial \boldsymbol{U}_x = {}^t\boldsymbol{U}_e^T\ {}^0\partial \boldsymbol{H}_x$. ${}^t\boldsymbol{U}_e^T$ is a matrix of element nodal displacements; ${}^0\partial \boldsymbol{H}_x$ is a matrix of elements shape function spatial derivatives and can be precomputed.

Calculating the strain-stress matrix from equation (6-12), the element nodal force integral as shown in equation (6-8) can be evaluated as following for linear tetrahedral elements.

$$ {}^t\boldsymbol{F} = {}^0V\,{}^t_0\boldsymbol{B}^T\,{}^t_0\boldsymbol{\sigma} \tag{6-17}$$

The computed element nodal force at each time step is used in equation (6-10) to calculate the next time step displacement.

6.2 Modified Solver for Nonlinear Deformation

Soft tissue's complex behaviour is highly resulted from the material and geometrical nonlinearity of the tissue. In other words, not only the stress-strain relationship is nonlinear (material), also the strain is nonlinearly related to displacement values (geometry). Besides, the nonlinear nature of the boundary conditions at the tool-tissue's contact area adds to the complexity of the soft tissue's deformation simulation. As earlier discussed in chapter 1, and shown in Figure 1-2, the tool-tissue interaction is not in the scope of this project. However, the TLED, explained in section 6.1, considers both material and geometrical nonlinearity.

6.2.1 State Equations

The equilibrium equation (6-10)should be reformulated to match the KF state equation (3-2). We consider nodal displacements ${}^{t}\boldsymbol{u}$ as the unknown variable. Ignoring the negligible damping effect in short time simulations, equation (6-10) reduces to

$${}^{t+\Delta t}\boldsymbol{u}_i = \frac{\Delta t^2}{M_{ii}}\left({}^{t}\boldsymbol{r}_i - {}^{t}\boldsymbol{F}_i\right) + 2\ {}^{t}\boldsymbol{u}_i - {}^{t-\Delta t}\boldsymbol{u}_i. \tag{6-18}$$

Taylor et al. (2008) discussed the suitability of neglecting damping effect in soft tissue deformation in fast short period simulations.

As can be seen in equation (6-18), the state estimate at each time step, i.e. ${}^{t+\Delta t}\boldsymbol{u}_i$, depends on two last state estimates. But the filtering system equation (3-2) relates the state estimate to specifically the last time estimate only. This means that the second last estimate is taken as the system input, leading to an uncertain system input. This results an output estimate with lower accuracy. To avoid the explained issue and improve the estimates accuracy, we define the new state (hereafter, the NL-state) as ${}^{t+\Delta t}\boldsymbol{x} \coloneqq \begin{bmatrix} {}^{t+\Delta t}\boldsymbol{u} \\ {}^{t}\boldsymbol{u} \end{bmatrix}$. Hence, equation (6-18) can be reframed as

$$\begin{bmatrix} {}^{t+\Delta t}\boldsymbol{u} \\ {}^{t}\boldsymbol{u} \end{bmatrix} = \begin{bmatrix} 2 & -1 \\ 1 & 0 \end{bmatrix} \begin{bmatrix} {}^{t}\boldsymbol{u} \\ {}^{t-\Delta t}\boldsymbol{u} \end{bmatrix} + \begin{bmatrix} \frac{\Delta t^2}{M_{ii}} \\ 0 \end{bmatrix} \left({}^{t}\boldsymbol{r}_i - {}^{t}\boldsymbol{F}_i\right). \tag{6-19}$$

So, the system equation (3-2) parameters are defined as $F = \begin{bmatrix} 2 & -1 \\ 1 & 0 \end{bmatrix}$, $G = \begin{bmatrix} \frac{\Delta t^2}{M_{ii}} & 0 \end{bmatrix}^T$, and ${}^t\boldsymbol{z} = \left({}^t\boldsymbol{r}_i - {}^t\boldsymbol{F}_i \right)$. The nodal displacement at the indenter tip (observation point), that is a scalar value, is collected as measurements. Hence, the measurement matrix H is a block 1×2 matrix that relates the displacement scalar values to the NL-state vector. In the other word, $H \coloneqq [H_1 \quad 0]$ with H_1 to be a binary matrix with the proper dimension mapping the observation point in the mesh global coordinate system.

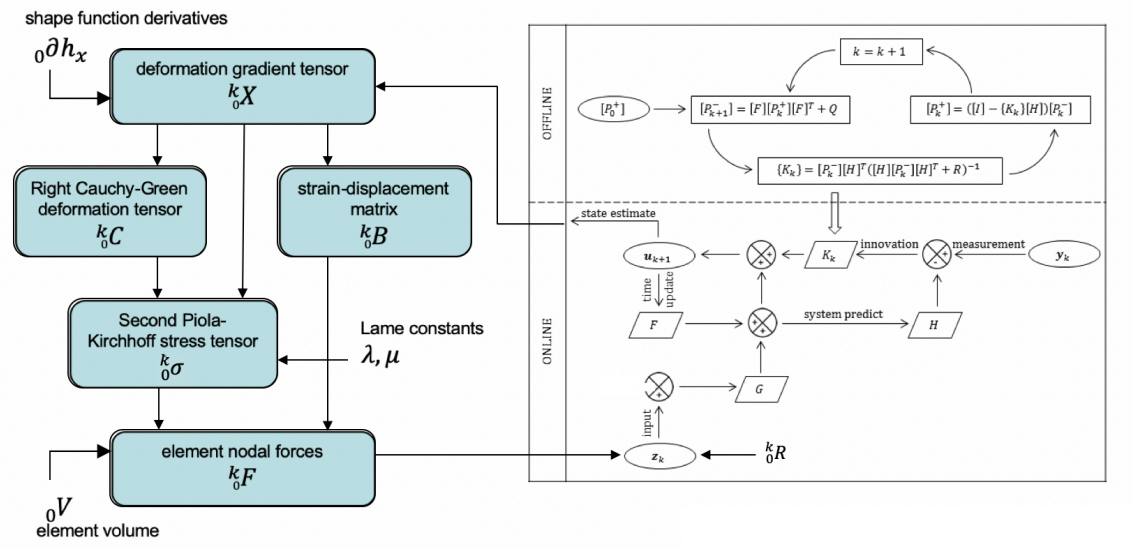

Figure 6-1. The NL$_{TL}$.KF-FEM for large nonlinear deformations

6.2.2 Modified Algorithm

The basic developed KF-FEM algorithm, shown in Figure 3-1, is modified for large nonlinear deformations as explained in sections 6.1 and 6.2.1. Figure 6-1 illustrates the modified algorithm.

6.3 Performance Evaluation

Simulations were conducted on a $8 \times 8 \times 3\, mm$ cubic model to evaluate the performance of the proposed method in terms of accuracy and computational speed. The body domain is divided into 2062 4-node tetrahedral elements compound of 549 nodes. Material properties including the density, Poisson's ratio, and Young's modulus are obtained from the literature, as presented in Section 3.4.

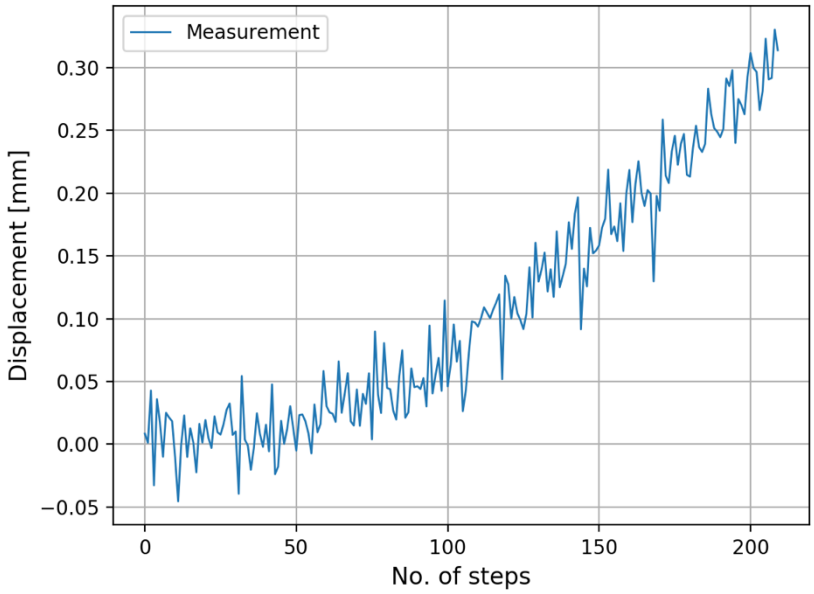

Figure 6-2. Displacement measurement at the observation point

The nodes on the bottom surface are considered as the fixed boundary condition. A circular flat-end probe with 4 mm diameter applies the load at the centre of the model's top surface, linearly increasing from 0 to 0.2 N in 210 time-steps. We employed the lump mass matrix (LMM) formulation, that diagonalizes the mass matrix. For comparison purposes, the FEM was carried out to derive the displacement at the centre point of the contact area (hereafter, the observation point). The displacement values from the FEM are taken as reference values. Measurements required for the NL_{TL}.KF-FEM system equations are generated artificially by adding a random white Gaussian noise to the reference values. Figure 6-2 shows the artificially generated measurement at the observation point.

The proposed algorithm is coded with Python programming language. The initial value of the displacement vector is set to zero. Figure 6-3 shows the undeformed and deformed cube model. Because displacement values are very small, only mesh nodes are illustrated for a clear vision of the deformation. In Figure 6-3(b), colour tones are used to illustrate the magnitude and direction of the displacement. Most nodes with nearly zero displacements, especially towards the bottom parts of the model, are shown with bright green. Nodes with darker tones

towards purple have positive displacements (downward), and nodes with brighter tones towards yellow have negative displacements (upward). It is interpreted that nodes in a very close circular distance from the probe edge move upward due to the incompressibility of the tissue.

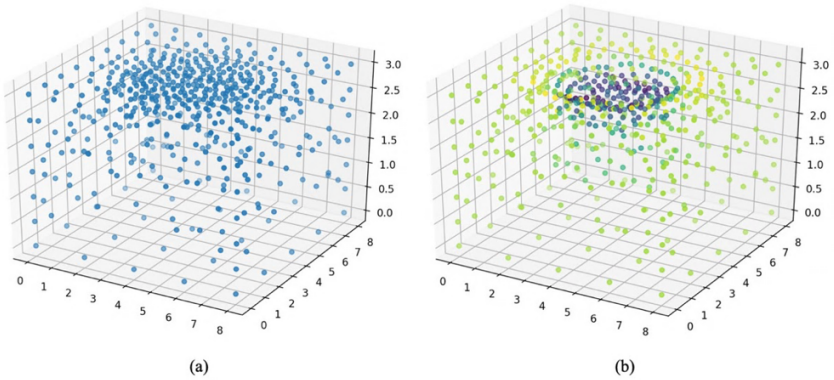

Figure 6-3. The simulated model; (a) undeformed, (b) deformed

6.3.1 Estimates Accuracy

Figure 6-4 compares displacement estimates at the observation point obtained by the developed KF-FEM with true values from the FEM and measurements. It can be seen from Figure 6-4 that the NL_{TL}.KF-FEM estimates are a trade-off between displacement measurements and the modelled FE predictions. Using the calculated gain at each time step, the algorithm compares the model prediction with the measurements and updates its next time step estimate.

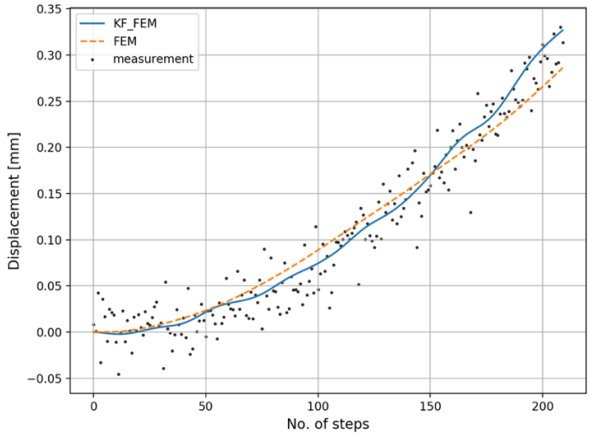

Figure 6-4. The NL_{TL}.KF-FEM estimates vs. the reference FEM and measurements at the observation point

The mean absolute error (MAE) of the developed KF-FEM estimates and the FEM with respect to the measurements are calculated and presented in Table 6-1. The error percentage of both methods in regard to the maximum computed displacement is also presented in Table 6-1.

Table 6-1. The estimates MAE in comparison with the FEM

	MAE [mm]	Error [%]
FEM	0.019	6.20
NL_{TL}.KF-FEM	0.018	5.75

The proposed NL_{TL}.KF-FEM estimates soft tissue deformation across the entire body domain using only the loading input (force and displacement) available at one point (i.e., the observation point). Figure 6-5 shows the displacement at a random point with negative displacement in close distance from the probe edge. It should be noted that at nodes that the measurement is not available, the NL_{TL}.KF-FEM relies on the FE model prediction and the computed spatial gain. Hence, the estimates show higher variations, although in micro scale. As an example, this simulation had around 0.3 mm the maximum displacement after 200-time steps, as shown in Figure 6-4. At the same time point, Figure 6-5 shows around 0.03 mm displacement in a random point, calculated by the FEM with less than 0.01 mm difference from the estimated value by the NL_{TL}.KF-FEM. One of the reasons leading to this variation can be the quality of the mesh. The better the quality of the mesh, the more reliable the FEM is in the absence of measurements.

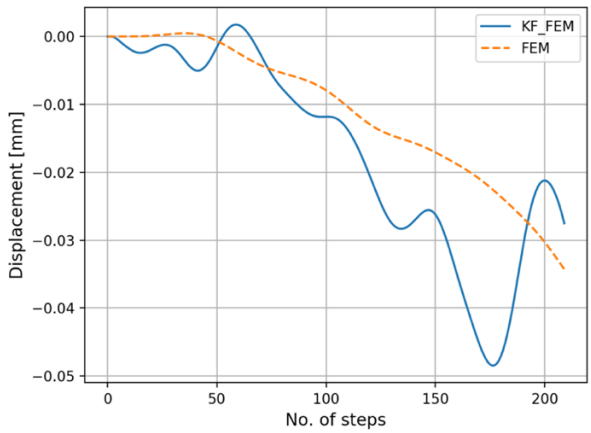

Figure 6-5. The NL KF-FEM estimates vs. the reference FEM in a random point

6.3.2 Computational performance

The NL_{TL}.KF-FEM simulation was performed on a laptop with 3.1 GHz Intel Core i5 Macintosh with 8 GB memory. The total computational time for 210 time-steps was around 5.5 ~ 6 seconds on average. The equivalent update frequency is 35 Hz, and above, that is higher than the 25 Hz graphical refresh rate required for real-time visual feedback.

6.4 Real-time Implementation

Employing the TLED approach has shown the advantage of computations being done in the element level, i.e., there is no need to assemble material matrices and system parameters in the geometrical global scale. In addition to that, derivatives are computed with respect to the initial undeformed state of the geometrical model, that eliminates the requirement of updating parameters time derivatives at each time step. However, calculations in the element level may cause a slow performance as several computational loops through the mesh nodes and elements are involved.

6.4.1 Geometry Structure

Advance programming techniques are used in this project to avoid slow computational process of element-wise calculation. Mesh nodes are stored with their indices and coordinates in a 2D array. Elements connectivity 2D array lists the mesh elements with their 4 nodes indices that form the relevant element. Figure 6-6 shows 5 random samples from the nodes and elements connectivity 2-dimensional arrays.

Node	x(mm)	y(mm)	z(mm)
90	8.0	0.0	1.0
368	3.4	3.7	1.5
508	7.3	1.8	1.9
539	0.5	5.5	2.5
93	8.0	0.0	2.5

Element	n1	n2	n3	n4
1630	545	319	539	540
1055	468	4	196	75
606	439	484	152	145
912	368	216	217	367
426	466	368	467	417

Figure 6-6. Samples from the mesh nodes coordinates and the elements connectivity list

As an example, Figure 6-6 shows that element #912 is formed from tetrahedral connection between nodes 368, 216, 217, and 367 and their respective coordinates in the global coordinate system. To enhance the speed of calculations, a 2D array is formed that maps each node with its index to the elements indices in which is being shared. It also implements that what local number out of 4 that specific node gets within that element. This approach helps not to lose the track of nodes and their connections in deformed status. To exemplify, Figure 6-7 shows that node #2 is included in 3 elements, and node #20 is shared between 8 elements.

	node	elem	local_n
128	20	887	1
129	20	992	2
130	20	1296	3
131	20	1559	3
132	20	1654	1
133	20	1951	3
134	20	2041	1
135	20	2042	2

	node	elem	local_n
12	2	563	1
13	2	1539	3
14	2	1802	1

Figure 6-7. Samples from the nodes mapping array

Figure 6-8 shows the mesh mapping structure. The programmed structure increases the calculation speed to update each node coordinates after computations are completed at element level, without requiring the global assembly of the spatial domain.

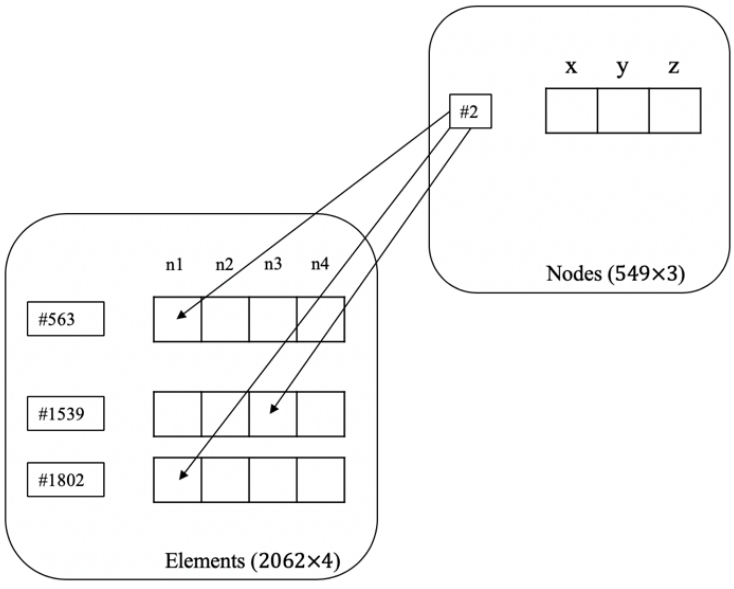

Figure 6-8. Mesh mapping structure

6.4.2 Arrays Structure

The main computational effort in the explained procedure is calculating the elements nodal force vector at each time step. Because each element computation can be completed independent from the rest, it is important to structure proper 3-dimensional arrays to avoid computational loops. In a 3-dimensional deformation with 4-node tetrahedral elements employed in discretizing the geometry, model parameters in the element level will have dimensions as follows.

- Shape function spatial derivatives, ${}^{0}\partial H_x$: $2062 \times 4 \times 3$
- Deformation gradient tensor, ${}^{t}_{0}X$: $2062 \times 3 \times 3$
- Strain-displacement matrix, ${}^{t}_{0}B$: $2062 \times 6 \times 12$
- Right Cauchy-Green deformation tensor, ${}^{t}_{0}C$: $2062 \times 3 \times 3$
- Second Piola-Kirchhoff stress tensor, ${}^{t}_{0}\sigma$: $2062 \times 6 \times 1$
- Element nodal forces, ${}^{t}\boldsymbol{F}$: $2062 \times 4 \times 3$

Figure 6-9 illustrates a schematic of the programmed structure in the core of the simulation.

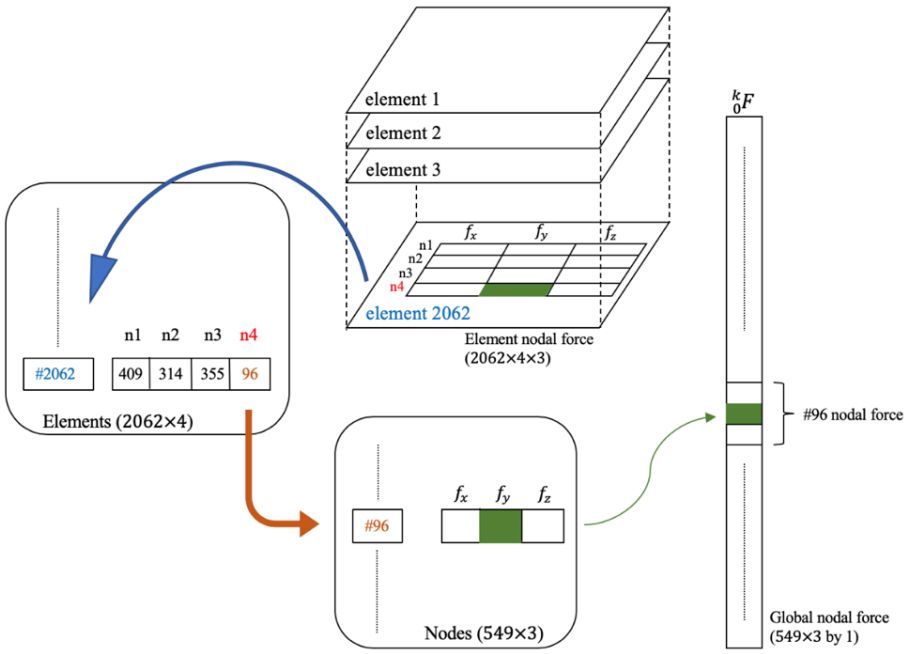

Figure 6-9. A schematic of the structure developed for parallel calculation of elements nodal forces

6.5 Conclusion

A fast estimation algorithm is proposed that computes large nonlinear deformations of soft tissues and achieves high computational speed suitable for real-time medical applications. The proposed method uses the Total Lagrangian Explicit Dynamics (TLED) approach to simulate nonlinear deformations while employing the optimised estimator Kalman filter (KF) to correct and validate the output through the incorporation of direct measurements. The proposed method achieved the update frequency of minimum 35 Hz. Further to this, it filtered out the measurement noise and was able to improve the displacement estimates accuracy by 0.45% (see Table 6-1). The proposed NL_{TL}.KF-FEM can expand its estimates in the spatial domain while measurements are only available at some areas of the geometrical model.

Further research requires to improve the functionalities of the proposed method. Soft tissues material properties are highly patient dependent. The proposed algorithm should be modified to estimate tissue's parameters, such as Young's modulus, in real time and correct the system estimates with the updated settings. Also, soft tissues under large deformations exhibit inhomogeneous behaviour. More complex material properties with higher order energy functions should be considered to simulate the behaviour of the tissue appropriately.

INTENTIONALLY LEFT BLANK

CHAPTER 7

CONCLUSION

INTENTIONALLY LEFT BLANK

7 Conclusion

The high-precision continuum mechanics equilibrium equations were employed to develop a real-time optimal predicting algorithm to estimate the deformation of the biological soft tissue for medical training simulators. The established algorithm benefits from the high accuracy and realistic approach of the finite element method (FEM) and the fast and recursive solution of the optimal estimator Kalman filter (KF).

7.1 Computational Speed vs. Accuracy

The proposed algorithm achieved an update frequency of ~89 Hz in the small range indentation simulation of a liver model compound of ~4100 elements (Table 3-2). The obtained calculation frequency is an excellent improvement to the ~5 Hz computed by FEM under identical boundary condition and simulation platform.

Besides, simulation results show that the developed KF-FEM does not sacrifice estimation accuracy. The KF-FEM displacement estimates median error concerning the FEM response, i.e. the standard reference value, was $0.0015\ mm$, while the median error of the measured displacement at the indenter tip was $0.0376\ mm$. This means that the proposed method was able to filter out ~96% of the measurement noise (Figure 3-6). In addition to that, the estimation median error was achieved in a simulation of maximum $1.472\ mm$ displacement. In other words, the normalized estimation error was ~0.1% on average (Figure 3-4). The developed algorithm promises high accuracy estimates with real-time computational performance in small linear ranges of soft tissue deformation.

7.2 Analytical Model Inaccuracy

Soft tissues material properties are not constant in different situations; they are patient specific as well. Geometrical models are also not accurate in terms of the operation boundary conditions. Hence, the analytical approaches such as the FEM do not guarantee the outcome.

The developed KF-FEM introduced the model error into the system equations. Simulation results were compared with the experiments conducted on silicon samples. The calibrated KF-FEM with initial measurement and model errors produced more consistent estimates in comparison with the observed noisy measurements. In addition to that, the KF-FEM estimates were a trade-off between measurements and the FE model response (Figure 4-7).

The proposed algorithm achieved an update frequency of ~145 Hz in deformation simulation of a cubic model compound of ~5000 elements (Appendix C, Table 2). Results confirm the capability of real-time computational performance of the method.

Including both measurement and model errors in the system equations, results confirmed that the developed KF-FEM could improve the fully predictive response of the FEM in real-time applications. Furthermore, the experiments confirm that the temporally linearized FEM is reliable within the applied displacement range. Hence, the KF can be employed.

7.3 System Input Uncertainty

In real-time applications, force values are obtained from sensors, leading to uncertain system inputs. The developed KF-FEM was further improved with the modified state involving both input and output. System input error was introduced as a “fake” system error. Simulations were conducted on a cubic model compound of ~2100 elements and compared with the reference FEM given the noisy input force.

The modified KF-FEM filtered ~58% of the measurement noise and increased the accuracy of the estimates by ~24% in comparison with the FEM given the uncertain input

force (Table 5-1). The update frequency of the deformation estimation was improved from around 3~5 Hz for the conventional FEM to approximately 36~131 Hz for the KF-FEM within the same geometrical domain.

Results confirmed that the proposed method incorporated real-time I/O measurements and enhance the computational process of displacement estimation. It also reduced the effect of the error in the I/O measurements. Further to this, the modified algorithm could differentiate the input uncertainty from the model error, leading to more accurate estimates compared to the classic FEM with the noisy boundary forces (Figure 5-5).

7.4 Large Nonlinear Deformations

A nonlinear strain energy function was considered with nonlinear strain-displacement function to simulate complex material and geometrical nonlinear behaviour of the tissue. The Total Lagrangian Explicit Dynamics (TLED) approach was used and reformulated the equilibrium equations to meet the requirements of the system equations of the optimised estimator KF. A two-time-step displacement vector was introduced as the system state.

The proposed method achieved the update frequency of minimum 35 Hz. Further to this, it filtered out the measurement noise and was able to improve the displacement estimates accuracy in comparison with the reference FEM (Table 6-1).

7.5 Contributions

- The high precision FEM and fast, optimized estimator KF were combined and achieved accurate real-time simulations of the biological soft tissue deformation.
- The converging towards zero estimation error in the offline phase made the algorithm promising the performance before the actual simulation begins.

- The measurement, the model, and the input errors were all considered, leading to an optimized estimation differentiating the system error from I/O measurements.
- Displacement estimates were extendable in the spatial domain while direct measurements were only available at some points of the geometry.
- Geometrical and material nonlinear deformation was achieved.

7.6 Future Work

Further research requires to improve the functionalities of the proposed method. Soft tissues material properties are highly patient dependent. The proposed algorithm should be modified to estimate tissue's parameters, such as Young's modulus, in real-time and correct the system estimates with the updated settings.

Soft tissues under large deformations exhibit inhomogeneous behaviour. More complex material properties with higher-order energy functions should be considered to simulate the behaviour of the tissue appropriately.

The model error and I/O measurement noise are not constant in practice. They might not have necessarily a white Gaussian distribution as well. Adaptive noise recognition approaches are required to be implemented into the developed KF-FEM to enhance the accuracy of the estimates and not lose the real-time performance.

Publications

Yarahmadian, M., Zhong, Y., Gu, C., & Shin, J. (2017). Soft tissue deformation estimation by spatio-temporal Kalman filter finite element method. *Technology and Health Care, 26*(S1), 317-325. doi:10.3233/THC-174640

Yarahmadian, M., Dabnichki, P., Pang, T.Y. (2019). Soft tissue behaviour estimation in small deformations. *Proceedings of ICM13*, 184-189

References

AlMutawa, J. (2012). Robust Kalman smoother for EIV state space model based on multivariate least trimmed squares estimator. *IMA journal of mathematical control and information, 29*(1), 23-32. doi:10.1093/imamci/dnr022

Bo, Z., Lixu, G., Jingsi, Z., Zhennan, Y., Lei, P., & Qiang, Z. (2008). Simulation of organ deformation using boundary element method and meshless shape matching. In (Vol. 2008, pp. 3253-3256).

Castaneda, M. A. P., & Cosio, F. A. (2004). Deformable model of the prostate for TURP surgery simulation. *Comput. Graph.-UK, 28*(5), 767-777. doi:10.1016/j.cag.2004.06.014

Chui, C., Kobayashi, E., Chen, X., Hisada, T., & Sakuma, I. (2004). Combined compression and elongation experiments and non-linear modelling of liver tissue for surgical simulation. *Medical and Biological Engineering and Computing, 42*(6), 787-798. doi:10.1007/bf02345212

Comas, O., Taylor, Z. A., Allard, J., Ourselin, S., Cotin, S., & Passenger, J. (2008). Efficient nonlinear FEM for soft tissue modelling and its GPU implementation within the open source framework SOFA. In (Vol. 5104, pp. 28-39).

Cotin, S., Delingette, H., & Ayache, N. (1999). Real-time elastic deformations of soft tissues for surgery simulation. *IEEE Transactions on Visualization and Computer Graphics, 5*(1), 62-73. doi:10.1109/2945.764872

Courtecuisse, H., Allard, J., Kerfriden, P., Bordas, S. P. A., Cotin, S., & Duriez, C. (2014). Real-time simulation of contact and cutting of heterogeneous soft-tissues. *Medical Image Analysis, 18*(2), 394-410. doi:10.1016/j.media.2013.11.001

Courtecuisse, H., Jung, H., Allard, J., Duriez, C., Lee, D. Y., & Cotin, S. (2010). GPU-based real-time soft tissue deformation with cutting and haptic feedback. *Prog Biophys Mol Biol, 103*(2-3), 159-168. doi:10.1016/j.pbiomolbio.2010.09.016

Cover, S. A., Ezquerra, N. F., O'Brien, J. F., Rowe, R., Gadacz, T., & Palm, E. (1993). Interactively deformable models for surgery simulation. *IEEE Computer Graphics and Applications, 13*(6), 68-75. doi:10.1109/38.252559

Dabnichki, P., Lauder, M., Aritan, S., & Tsirakos, D. (1997). Accuracy evaluation of an on-line kinematic system via dynamic tests. *Journal of Medical Engineering & Technology, 21*(2), 53-66. doi:10.3109/03091909709008405

De, S., Kim, J., Lim, Y.-J., & Srinivasan, M. A. (2005). The point collocation-based method of finite spheres (PCMFS) for real time surgery simulation. *Computers and Structures, 83*(17-18), 1515-1525. doi:10.1016/j.compstruc.2004.12.003

Deo, D. (2010). A physics driven neural networks-based simulation system (PhyNNeSS) and its application to local and remote surgery simulation. In S. De (Ed.): ProQuest Dissertations Publishing.

Famaey, N., & Vander Sloten, J. (2008). Soft tissue modelling for applications in virtual surgery and surgical robotics. *Comput Methods Biomech Biomed Engin, 11*(4), 351-366. doi:10.1080/10255840802020412

Fortmeier, D., Mastmeyer, A., Schroder, J., & Handels, H. (2016). A Virtual Reality System for PTCD Simulation Using Direct Visuo-Haptic Rendering of Partially Segmented Image Data. *IEEE Journal of Biomedical and Health Informatics, 20*(1), 355-366. doi:10.1109/JBHI.2014.2381772

Freutel, M., Schmidt, H., Dürselen, L., Ignatius, A., & Galbusera, F. (2014). Finite element modeling of soft tissues: Material models, tissue interaction and challenges. *Clinical Biomechanics*, 363-372. doi:10.1016/j.clinbiomech.2014.01.006

Fu, Y. B., & Chui, C. K. (2014). Modelling and simulation of porcine liver tissue indentation using finite element method and uniaxial stress-strain data. *Journal of Biomechanics, 47*(10), 2430-2435. doi:10.1016/j.jbiomech.2014.04.009

Gardano, P., & Dabnichki, P. (2006). Application of boundary element method to modelling of added mass and its effect on hydrodynamic forces. *Computer Modeling in Engineering and Sciences, 15*(2), 87.

Georgii, J., & Westermann, R. (2005). Mass-spring systems on the GPU. *Simulation Modelling Practice and Theory, 13*(8), 693-702. doi:10.1016/j.simpat.2005.08.004

Ghahremani, E., & Kamwa, I. (2011). Dynamic State Estimation in Power System by Applying the Extended Kalman Filter With Unknown Inputs to Phasor Measurements. *Power Systems, IEEE Transactions on, 26*(4), 2556-2566. doi:10.1109/tpwrs.2011.2145396

Hammer, P., Sacks, M. S., Del Nido, P. J., & Howe, R. D. (2011). Mass-Spring Model for Simulation of Heart Valve Tissue Mechanical Behavior. *39*(6). doi:10.1007/s10439-011-0278-5

Hasegawa, Y., Shimayoshi, T., Amano, A., & Matsuda, T. (2016). Application of the Kalman Filter for Faster Strong Coupling of Cardiovascular Simulations. *IEEE Journal of Biomedical and Health Informatics, 20*(4), 1100-1106. doi:10.1109/jbhi.2015.2436212

Horton, A., Wittek, A., Joldes, G. R., & Miller, K. (2010). A meshless Total Lagrangian explicit dynamics algorithm for surgical simulation. *International Journal for Numerical Methods in Biomedical Engineering, 26*(8), 977-998. doi:10.1002/cnm.1374

Hoshi, T., Kobayashi, Y., Kawamura, K., & Fujie, M. G. (2007). *Developing an intraoperative methodology using the finite element method and the extended Kalman filter to identify the material parameters of an organ model.* Paper presented at the Annual International Conference of the IEEE Engineering in Medicine and Biology - Proceedings.

Jansson, J., & Vergeest, J. S. M. (2002). A discrete mechanics model for deformable bodies. *Computer-Aided Design, 34*(12), 913-928. doi:10.1016/S0010-4485(01)00146-4

Jeong, S. H., Zhang, S., Hjort, K., Hilborn, J., & Wu, Z. (2016). PDMS‐Based Elastomer Tuned Soft, Stretchable, and Sticky for Epidermal Electronics. *Advanced Materials, 28*(28), 5830-5836. doi:10.1002/adma.201505372

Jinao, Z., Yongmin, Z., & Chengfan, G. (2018). Deformable Models for Surgical Simulation: A Survey. *IEEE Reviews in Biomedical Engineering, 11*, 143-164. doi:10.1109/RBME.2017.2773521

Joldes, G. R., Chowdhury, H., Wittek, A., & Miller, K. (2017). A new method for essential boundary conditions imposition in explicit meshless methods. *Engineering Analysis with Boundary Elements, 80*, 94-104. doi:10.1016/j.enganabound.2017.03.011

Joldes, G. R., Wittek, A., & Miller, K. (2009). Suite of finite element algorithms for accurate computation of soft tissue deformation for surgical simulation. *Medical Image Analysis, 13*(6), 912-919. doi:http://dx.doi.org/10.1016/j.media.2008.12.001

Kenedi, R. M., Gibson, T., Evans, J. H., & Barbenel, J. C. (1975). Tissue mechanics. *Physics in medicine and biology, 20*(3), 699-717.

Kerdok, A. E., Cotin, S. M., Ottensmeyer, M. P., Galea, A. M., Howe, R. D., & Dawson, S. L. (2003). Truth cube: Establishing physical standards for soft tissue simulation. *Medical Image Analysis, 7*(3), 283-291. doi:10.1016/S1361-8415(03)00008-2

Kim, J., Choi, C., De, S., & Srinivasan, M. A. (2007). Virtual surgery simulation for medical training using multi‐resolution organ models. *International Journal of Medical Robotics and Computer Assisted Surgery, 3*(2), 149-158. doi:10.1002/rcs.140

Kühnapfel, U., Çakmak, H. K., & Maaß, H. (2000). Endoscopic surgery training using virtual reality and deformable tissue simulation. *Computers & Graphics, 24*(5), 671-682. doi:10.1016/S0097-8493(00)00070-4

Kunkler, K. (2006). The role of medical simulation: an overview. *International Journal of Medical Robotics and Computer Assisted Surgery, 2*(3), 203-210. doi:10.1002/rcs.101

Lamouche, G., Kennedy, B., Kennedy, K., Bisaillon, C. E., Curatolo, A., Campbell, G., . . . Sampson, D. D. (2012). Review of tissue simulating phantoms with controllable optical, mechanical and structural properties for use in optical coherence tomography. *Biomedical Optics Express, 3*(6), 1381-1398. doi:10.1364/BOE.3.001381

Lamouche, G., Kennedy, B. F., Kennedy, K. M., Bisaillon, C.-E., Curatolo, A., Campbell, G., . . . Sampson, D. D. (2012). Review of tissue simulating phantoms with controllable optical, mechanical and structural properties for use in optical coherence tomography. *Biomedical Optics Express, 3*(6), 1381-1398. doi:10.1364/BOE.3.001381

Lee, B., Popescu, D. C., Joshi, B., & Ourselin, S. (2006). Efficient topology modification and deformation for finite element models using condensation. *Studies in Health Technology and Informatics, 119*, 299-304.

Li, C., Ding, J., Hong, Z., Pan, Y., & Liu, P. X. (2018). A Surface Mass-Spring Model With New Flexion Springs and Collision Detection Algorithms Based on Volume Structure for Real-Time Soft-Tissue Deformation Interaction. *IEEE Access, 6*, 75572-75597. doi:10.1109/ACCESS.2018.2883679

Li, M., Miller, K., Joldes, G. R., Doyle, B., Garlapati, R. R., Kikinis, R., & Wittek, A. (2015). Patient-specific biomechanical model as whole-body CT image registration tool. In (Vol. 22, pp. 22-34).

Lim, Y.-J., & De, S. (2007). Real time simulation of nonlinear tissue response in virtual surgery using the point collocation-based method of finite spheres. *Computer Methods in Applied Mechanics and Engineering, 196*(31–32), 3011-3024. doi:http://dx.doi.org/10.1016/j.cma.2006.05.015

Liu, X. P., Shaoping, X., Hua, Z., & Linyan, H. (2011). A New Hybrid Soft Tissue Model for Visio-Haptic Simulation. *IEEE Transactions on Instrumentation and Measurement, 60*(11), 3570-3581. doi:10.1109/TIM.2011.2161142

Lorente, D., Martínez-Martínez, F., Rupérez, M. J., Lago, M. A., Martínez-Sober, M., Escandell-Montero, P., . . . Martín-Guerrero, J. D. (2017). A framework for modelling the biomechanical behaviour of the human liver during breathing in real time using machine learning. *Expert Systems With Applications, 71*, 342-357. doi:10.1016/j.eswa.2016.11.037

Mafi, R., & Sirouspour, S. (2014). GPU‐based acceleration of computations in nonlinear finite element deformation analysis. *International Journal for Numerical Methods in Biomedical Engineering, 30*(3), 365-381. doi:10.1002/cnm.2607

Marchesseau, S., Heimann, T., Chatelin, S., Willinger, R., & Delingette, H. (2010). Fast porous visco-hyperelastic soft tissue model for surgery simulation: Application to liver surgery. *Progress in Biophysics and Molecular Biology, 103*(2-3), 185-196. doi:10.1016/j.pbiomolbio.2010.09.005

Markovsky, I., & De Moor, B. (2005). Linear dynamic filtering with noisy input and output. *Automatica, 41*(1), 167-171. doi:10.1016/j.automatica.2004.08.014

Mayeur, O., Witz, J.-F., Lecomte-Grosbras, P., Cosson, M., & Brieu, M. (2018). Patient-specific simulation: non-destructive identification method for soft tissue under large strain – Application to pelvic system. *Computational Biomechanics for Medicine*.

Meehan, M., Teschner, M., & Girod, S. (2003). Three-dimensional simulation and prediction of craniofacial surgery. *Orthodontics & craniofacial research, 6 suppl 1*, 102-107.

Meier, U., López, O., Monserrat, C., Juan, M. C., & Alcañiz, M. (2005). Real-time deformable models for surgery simulation: a survey. *Computer Methods and Programs in Biomedicine, 77*(3), 183-197. doi:10.1016/j.cmpb.2004.11.002

Miller, K., Joldes, G., Lance, D., & Wittek, A. (2007). Total Lagrangian explicit dynamics finite element algorithm for computing soft tissue deformation. *Communications in Numerical Methods in Engineering, 23*(2), 121-134. doi:10.1002/cnm.887

Misra, S., Macura, K. J., Ramesh, K. T., & Okamura, A. M. (2009). The importance of organ geometry and boundary constraints for planning of medical interventions. *Medical Engineering & Physics, 31*(2), 195-206. doi:https://doi.org/10.1016/j.medengphy.2008.08.002

Moser, R., Kettlgruber, G., Siket, C. M., Drack, M., Graz, I. M., Cakmak, U., . . . Bauer, S. (2016). From Playroom to Lab: Tough Stretchable Electronics Analyzed with a Tabletop Tensile Tester Made from Toy‐Bricks. *Advanced Science, 3*(4), n/a-n/a. doi:10.1002/advs.201500396

Nealen, A., Müller, M., Keiser, R., Boxerman, E., & Carlson, M. (2006). Physically based deformable models in computer graphics. *Computer Graphics Forum, 25*(4), 809-836. doi:10.1111/j.1467-8659.2006.01000.x

Neumann, P. F., Sadler, L. L., & Gieser, J. (1998). Virtual reality vitrectomy simulator. In (Vol. 1496, pp. 910-917).

Niroomandi, S., Alfaro, I., Cueto, E., & Chinesta, F. (2012). Accounting for large deformations in real-time simulations of soft tissues based on reduced-order models. *Computer Methods and Programs in Biomedicine, 105*(1), 1-12. doi:http://dx.doi.org/10.1016/j.cmpb.2010.06.012

Palyanov, A., Khayrulin, S., & Larson, S. D. (2016). Application of smoothed particle hydrodynamics to modeling mechanisms of biological tissue. *Advances in Engineering Software, 98*, 1-11. doi:10.1016/j.advengsoft.2016.03.002

Patete, P., Iacono, M. I., Spadea, M. F., Trecate, G., Vergnaghi, D., Mainardi, L. T., & Baroni, G. (2013). A multi-tissue mass-spring model for computer assisted breast surgery. *Medical Engineering & Physics, 35*(1), 47-53. doi:http://dx.doi.org/10.1016/j.medengphy.2012.03.008

Peeken, J., Goldberg, T., Knie, C., Komboz, B., Bernhofer, M., Pasa, F., . . . Combs, S. (2018). Treatment information improve machine learning survival prediction in soft tissue sarcoma patients. *Radiother. Oncol., 127*(s1), S198-S198.

Picinbono, G., Lombardo, J. C., Delingette, H., & Ayache, N. (2002). Improving realism of a surgery simulator: linear anisotropic elasticity, complex interactions and force extrapolation. *Journal of Visualization and Computer Animation, 13*(3), 147-167. doi:10.1002/vis.257

Plantefeve, R., Peterlik, I., Haouchine, N., & Cotin, S. (2016). Patient-Specific Biomechanical Modeling for Guidance During Minimally-Invasive Hepatic Surgery. *Annals of Biomedical Engineering, 44*(1), 139-153. doi:10.1007/s10439-015-1419-z

Rausch, M., Karniadakis, G., & Humphrey, J. (2017). Modeling Soft Tissue Damage and Failure Using a Combined Particle/Continuum Approach. *Biomechanics and Modeling in Mechanobiology, 16*(1), 249-261. doi:10.1007/s10237-016-0814-1

Richardson, S., Babarenda Gamage, T. P., HajiRassouliha, A., Jackson, T., Hedges, K., Clark, A., . . . Nielsen, P. M. F. (2018). *Towards a real-time full-field stereoscopic imaging system for tracking lung surface deformation under pressure controlled ventilation*.

Rodríguez, A., León, A., & Arroyo, G. (2016). Parallel deformation of heterogeneous ChainMail models: Application to interactive deformation of large medical volumes. *Computers in Biology and Medicine, 79*, 222-232. doi:10.1016/j.compbiomed.2016.10.012

Rodríguez, A., León, A., Arroyo, G., & Mantas, J. (2015). SP-ChainMail: a GPU-based sparse parallel ChainMail algorithm for deforming medical volumes. *An International Journal of High-Performance Computer Design, Analysis, and Use, 71*(9), 3482-3499. doi:10.1007/s11227-015-1445-5

Samur, E., Sedef, M., Basdogan, C., Avtan, L., & Duzgun, O. (2007). A robotic indenter for minimally invasive measurement and characterization of soft tissue response. *Medical Image Analysis, 11*(4), 361-373. doi:10.1016/j.media.2007.04.001

Sandrin, L., Fourquet, B., Hasquenoph, J.-M., Yon, S., Fournier, C., Mal, F., . . . Palau, R. (2003). Transient elastography: a new noninvasive method for assessment of hepatic fibrosis. *Ultrasound in Medicine & Biology, 29*(12), 1705-1713. doi:10.1016/j.ultrasmedbio.2003.07.001

Satava, R. M. (1996). Medical virtual reality: The current status of the future. *Studies in Health Technology and Informatics, 29*, 100-106. doi:10.3233/978-1-60750-873-1-100

Schwartz, J.-M., Denninger, M., Rancourt, D., Moisan, C., & Laurendeau, D. (2005). Modelling liver tissue properties using a non-linear visco-elastic model for surgery simulation. *Medical Image Analysis, 9*(2), 103-112. doi:10.1016/j.media.2004.11.002

Sederberg, T. W., & Parry, S. R. (1986). Free-form deformation of solid geometric models. *SIGGRAPH Comput. Graph., 20*(4), 151-160. doi:10.1145/15886.15903

Shaoping Xu, X. P., Liu, X. P., Hua Zhang, X. P., & Linyan Hu, X. P. (2011). A Nonlinear Viscoelastic Tensor-Mass Visual Model for Surgery Simulation. *Instrumentation and Measurement, IEEE Transactions on, 60*(1), 14-20. doi:10.1109/tim.2010.2065450

Simon, D. (2006). *Optimal state estimation : Kalman, H. [infinity] and nonlinear approaches*. New Jersey: John Wiley.

Suga, R., & Kawahara, M. (2006). Estimation of Tidal Current using Kalman Filter Finite-Element Method. *Computers & Mathematics with Applications, 52*(8-9), 1289-1298. doi:10.1016/j.camwa.2006.11.006

Tadepalli, S. C., Erdemir, A., & Cavanagh, P. R. (2011). Comparison of hexahedral and tetrahedral elements in finite element analysis of the foot and footwear. *Journal of Biomechanics, 44*(12), 2337-2343. doi:http://dx.doi.org/10.1016/j.jbiomech.2011.05.006

Talbot, H., Spadoni, F., Duriez, C., Sermesant, M., O'neill, M., Jaïs, P., . . . Delingette, H. (2017). Interactive training system for interventional electrocardiology procedures. *Medical Image Analysis, 35*(C), 225-237. doi:10.1016/j.media.2016.06.040

Taylor, Z. A., Cheng, M., & Ourselin, S. (2008). High-speed nonlinear finite element analysis for surgical simulation using graphics processing units. *IEEE Transactions on Medical Imaging, 27*(5), 650-663. doi:10.1109/tmi.2007.913112

Tonutti, M., Gras, G., & Yang, G.-Z. (2017). A machine learning approach for real-time modelling of tissue deformation in image-guided neurosurgery. *Artificial Intelligence in Medicine, 80*, 39-47. doi:10.1016/j.artmed.2017.07.004

Umut Ozcan, M., Ocal, S., Basdogan, C., Dogusoy, G., & Tokat, Y. (2011). Characterization of frequency-dependent material properties of human liver and its pathologies using an impact hammer. *Medical Image Analysis, 15*(1), 45-52. doi:10.1016/j.media.2010.06.010

van Gerwen, D. J., Dankelman, J., & van den Dobbelsteen, J. J. (2012). Needle–tissue interaction forces – A survey of experimental data. *Medical Engineering and Physics, 34*(6), 665-680. doi:10.1016/j.medengphy.2012.04.007

Villard, P., Vidal, F., ap Cenydd, L., Holbrey, R., Pisharody, S., Johnson, S., . . . Gould, D. (2014). Interventional radiology virtual simulator for liver biopsy. *A journal for*

interdisciplinary research, development and applications of image guided diagnosis and therapy, 9(2), 255-267. doi:10.1007/s11548-013-0929-0

Wang, P., Becker, A. A., Jones, I. A., Glover, A. T., Benford, S. D., Greenhalgh, C. M., & Vloeberghs, M. (2007). Virtual reality simulation of surgery with haptic feedback based on the boundary element method. *Computers & Structures, 85*(7–8), 331-339. doi:http://dx.doi.org/10.1016/j.compstruc.2006.11.021

Wen, T., & Tao Ruan, W. (2014). Constraint-Based Soft Tissue Simulation for Virtual Surgical Training. *Biomedical Engineering, IEEE Transactions on, 61*(11), 2698-2706. doi:10.1109/tbme.2014.2326009

Wittek, A., Grosland, N. M., Joldes, G. R., Magnotta, V., & Miller, K. (2016). From Finite Element Meshes to Clouds of Points: A Review of Methods for Generation of Computational Biomechanics Models for Patient-Specific Applications. *Annals of Biomedical Engineering, 44*(1), 3-15. doi:10.1007/s10439-015-1469-2

Wu, J., Westermann, R., & Dick, C. (2015). A Survey of Physically Based Simulation of Cuts in Deformable Bodies. *Computer Graphics Forum, 34*(6), 161-187. doi:10.1111/cgf.12528

Wu, W., & Heng, P. A. (2004). A hybrid condensed finite element model with GPU acceleration for interactive 3D soft tissue cutting. *Computer Animation and Virtual Worlds, 15*(3‐4), 219-227. doi:10.1002/cav.24

Wu, W., & Heng, P. A. (2004). A hybrid condensed finite element model with GPU acceleration for interactive 3D soft tissue cutting. *Computer Animation and Virtual Worlds, 15*(3-4), 219-227. doi:10.1002/cav.24

Xi, J., Lamata, P., Lee, J., Moireau, P., Chapelle, D., & Smith, N. (2011). Myocardial transversely isotropic material parameter estimation from in-silico measurements based on a reduced-order unscented Kalman filter. *Journal of the Mechanical Behavior of Biomedical Materials, 4*(7), 1090-1102. doi:10.1016/j.jmbbm.2011.03.018

Yanni, Z., Liu, P. X., Qiangqiang, C., Pinhua, L., & Chunquan, L. (2017). A New Deformation Model of Biological Tissue for Surgery Simulation. *IEEE Transactions on Cybernetics, 47*(11), 3494-3503. doi:10.1109/TCYB.2016.2560938

Yarahmadian, M., Dabnichki, P., Pang, T.Y. (2019). Soft tissue behaviour estimation in small deformations. *Proceedings of ICM13*, 184-189

Yarahmadian, M., Zhong, Y., Gu, C., & Shin, J. (2017). Soft tissue deformation estimation by spatio-temporal Kalman filter finite element method. *Technology and Health Care, 26*(S1), 317-325. doi:10.3233/THC-174640

Zhang, Y., Folkert, M. R., Li, B., Huang, X., Meyer, J. J., Chiu, T., . . . Wang, J. (2019). 4D liver tumor localization using cone-beam projections and a biomechanical model. *Radiotherapy and Oncology, 133*, 183-192. doi:https://doi.org/10.1016/j.radonc.2018.10.040

Zhao, X., & Pelegri, A. A. (2016). A Bayesian approach for characterization of soft tissue viscoelasticity in acoustic radiation force imaging. *International Journal for Numerical Methods in Biomedical Engineering, 32*(4), n/a-n/a. doi:10.1002/cnm.2741

Zhou, J., Luo, Z., Li, C., & Deng, M. (2018). Real-time deformation of human soft tissues: A radial basis meshless 3D model based on Marquardt's algorithm. *Computer Methods and Programs in Biomedicine, 153*, 237-252. doi:10.1016/j.cmpb.2017.09.008

Zhu, B., & Gu, L. (2012). A hybrid deformable model for real-time surgical simulation. *Computerized Medical Imaging and Graphics, 36*(5), 356-365. doi:http://dx.doi.org/10.1016/j.compmedimag.2012.03.001

Zienkiewicz, O. C. a., Taylor, R. L., & Zhu, J. Z. (2013). *The finite element method : its basis and fundamentals* (Seventh edition. ed.): Elsevier, Butterworth-Heinemann.

Zou, Y., & Liu, P. X. (2017). A high-resolution model for soft tissue deformation based on point primitives. *Computer Methods and Programs in Biomedicine, 148*, 113-121. doi:10.1016/j.cmpb.2017.06.013

Appendix A

Assume that four nodes out of the total n number of mesh nodes are in contact with the indenter tip. Let us give them some random indices for simplicity of the formulation, for example, nodes number 2, 5, 6, and m. In one-directional displacement along the vertical axis (axis z), the measurement vector at each time point is $\boldsymbol{y} = [d_{2z} \quad d_{5z} \quad d_{6z} \quad d_{mz}]^T$. The state vector, i.e. displacement vector, includes the displacement of all n nodes at each time point along the three principal directions x, y, and z. Hence, it has the dimension $3n \times 1$ as follows.

$$\boldsymbol{x} = [d_{1x} \quad d_{1y} \quad d_{1z} \quad d_{2x} \quad d_{2y} \quad \dots \quad d_{ny} \quad d_{nz}]^T \qquad \text{(Appendix A-1)}$$

We need a matrix, called H, that maps the indices of the observation points from the state vector in a way that $\boldsymbol{y} = H\boldsymbol{x}$ at each time step, as shown in equation (3-1). Figure Appendix A-1 illustrates how the measurement matrix is formed depending on the observation nodes' indices.

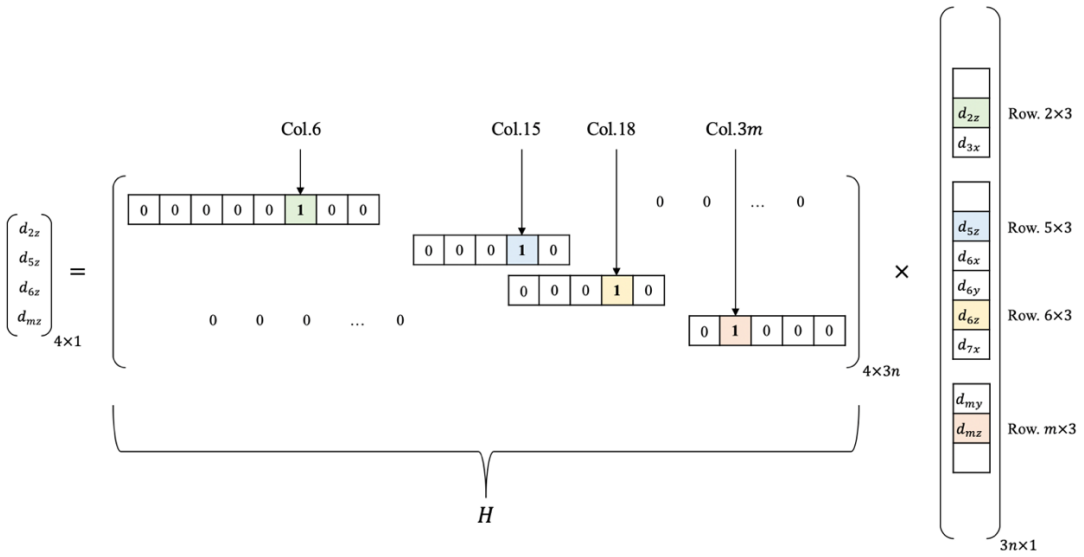

Figure 7-1. The binary measurement matrix addressing observation points in the state vector

As can be seen from figure Appendix A-1, all elements of matrix H are zero except the elements that correspond to the observation points. Because the geometrical model is three dimensional, the displacement of each node along the z-axis is the third position in the target node's indices. In the applications that the contact area is constant during the simulation, the observation points are detected before the operation; hence, matrix H can be predefined.

Appendix B

Technology and Health Care 26 (2018) S317–S325
DOI 10.3233/THC-174640
IOS Press

Soft tissue deformation estimation by spatio-temporal Kalman filter finite element method

Mehran Yarahmadian*, Yongmin Zhong, Chengfan Gu and Jaehyun Shin
School of Engineering, RMIT University, Bundoora, Australia

Abstract.
BACKGROUND: Soft tissue modeling plays an important role in the development of surgical training simulators as well as in robot-assisted minimally invasive surgeries. It has been known that while the traditional Finite Element Method (FEM) promises the accurate modeling of soft tissue deformation, it still suffers from a slow computational process.
OBJECTIVE: This paper presents a Kalman filter finite element method to model soft tissue deformation in real time without sacrificing the traditional FEM accuracy.
METHODS: The proposed method employs the FEM equilibrium equation and formulates it as a filtering process to estimate soft tissue behavior using real-time measurement data. The model is temporally discretized using the Newmark method and further formulated as the system state equation.
RESULTS: Simulation results demonstrate that the computational time of KF-FEM is approximately 10 times shorter than the traditional FEM and it is still as accurate as the traditional FEM. The normalized root-mean-square error of the proposed KF-FEM in reference to the traditional FEM is computed as 0.0116.
CONCLUSIONS: It is concluded that the proposed method significantly improves the computational performance of the traditional FEM without sacrificing FEM accuracy. The proposed method also filters noises involved in system state and measurement data.

Keywords: Soft tissue deformation, finite element, real-time estimation, Kalman filter

1. Introduction

A large number of research efforts has been dedicated to the modeling of soft tissue deformation which has been a challenging task to meet the requirements of both the physical realism and the real-time computational performance [1,2]. Among the current methods for modeling of soft tissue deformation, the Finite Element Method (FEM) focuses on continuum mechanics for accurate deformation modeling in which the mechanical behaviors of soft tissues are accurately characterized by continuum constitutive equations [3]. However, these methods suffer from an expensive computational load [4,5].

A variety of strategies has been employed to improve the computational performance of FEM. The matrix condensation technique reduces the computational time by limiting the full computation of volume elements to the surface nodes [6]. However, this simplification significantly reduces the simulation

*Corresponding author: Mehran Yarahmadian, School of Engineering, RMIT University, Bundoora, VIC 3083, Australia. Tel.: +61 03 9925 6018; Fax: +61 03 9925 6108; E-mail: mehran.yarahmadian@gmail.com.

0928-7329/18/$35.00 © 2018 – IOS Press and the authors. All rights reserved
This article is published online with Open Access and distributed under the terms of the Creative Commons Attribution Non-Commercial License (CC BY-NC 4.0).

accuracy. The pre-computation method uses pre-computed equilibrium solutions to reduce the computational time [7]. However, this method does not allow topographical changes in the body domain, and its pre-computation process is also time-consuming. The explicit FEM reduces the computational load by eliminating the iterative solution of large systems [8]. However, the stability of the solution is strictly dependent on the size of studied time steps. The GPU (Graphics Processing Unit) acceleration is a technique to use GPU to facilitate the computational performance of FEM [9]. However, this method relies on hardware, and it does not solve the computational problem fundamentally. In general, with most of the existing methods, the enhanced computational performance of FEM is achieved by sacrificing the accuracy of FEM modeling.

Kalman filter is a commonly used method for real-time estimation of system state parameters. Kato et al. employed the Kalman filter to estimate the ground motion [10]. Zeng et al. combined the extended Kalman filter with an optimization algorithm to estimate the state parameters of lateral flow immunoassay [11]. The major difficulty in using the Kalman filter lies in the construction of the system state equation to describe the dynamics of soft tissue deformation.

This paper presents a new method for real-time simulation of soft tissue deformation. Rather than direct calculation of soft tissue deformation from FEM, which causes a slow computational process, this method formulates the deformation of soft tissues as a filtering identification process. The computational domain is temporally discretized be the Newmark method and further transformed into a state space representation. Finally, a Kalman filter is developed to eliminate system and measurement noises to estimate the dynamic behaviors of soft tissues in real time based on measurement data. Simulations and analysis have been conducted to verify the performance of the proposed method.

2. Methodology

2.1. State and measurement equations

Consider the following linear discrete-time dynamic system with the state vector $\boldsymbol{x}_k$ given a set of measurement y_k at time point k,

$$\boldsymbol{x}_k = F\boldsymbol{x}_{k-1} + G\boldsymbol{z}_{k-1} \tag{1}$$

$$y_k = H\boldsymbol{x}_k + v \tag{2}$$

where $\boldsymbol{z}$ is the system input, F, H, and G are the state transition, measurement, and input matrices respectively, and v is the measurement zero-mean white Gaussian noise with known diagonal covariance R. The Kalman filter is described as a linear recursive least-square estimator,

$$\hat{\boldsymbol{x}}_k = \hat{\boldsymbol{x}}_{k-1} + K_k(y_k - H\hat{\boldsymbol{x}}_{k-1}) \tag{3}$$

where K_k is the Kalman gain and $\hat{\boldsymbol{x}}_k$ is the estimation of state $\boldsymbol{x}_k$ to minimize the sum of squares between the previous estimation $H\hat{\boldsymbol{x}}_{k-1}$ and current measurement y_k. The item $y_k - H\hat{\boldsymbol{x}}_{k-1}$ is called the innovation term.

2.2. Finite element formulation

Soft tissues are highly complex in terms of material composition. For the modeling purpose, it is very important to choose appropriate material law and parameters that describe mechanical properties of soft tissues. While soft tissue structure shows time-dependent, nonlinear and anisotropic behaviors, in

terms of small deformation within a short-term period, soft tissues can be investigated by linear isotropic models to high precision.

The basic equations of an elastic material are strains, stresses and equilibrium relations [12]. In case of small deformations, the six independent components of the strain matrix, i.e. ε_{ij} are computed from displacements in the form of

$$\varepsilon_{ij} = (\boldsymbol{u}_{i,j} + \boldsymbol{u}_{j,i})/2 \tag{4}$$

where $\boldsymbol{u}$ is the displacement and $\boldsymbol{u}_{i,j} \equiv \partial \boldsymbol{u}_i / \partial x_j$ with respect to a coordinate component x_j. For elastic materials, the Hooke's law linear stress-strain relationship can be represented as

$$\boldsymbol{\sigma}_{ij} = D_{ijkl}\varepsilon_{kl} \tag{5}$$

where $\boldsymbol{\sigma}$ is the stress and D_{ijkl} is the elastic moduli for an isotropic elastic material. Using only the six independent components of the symmetric stress, the linear momentum or equilibrium equation can be written as

$$\partial \boldsymbol{\sigma}_{ij} / \partial x_i + \boldsymbol{b}_i = \rho \ddot{\boldsymbol{u}}_i \tag{6}$$

where $\boldsymbol{b}$ is the vector of body forces, ρ is the mass density per unit volume and $\ddot{\boldsymbol{u}}$ is the acceleration vector.

It is assumed that the domain of analysis is divided into a set of elements and nodes over the entire body domain Ω. In consideration of the Rayleigh damping coefficient $C = \alpha_0 M + \alpha_1 K$ and by evaluating the weak form of equilibrium equations for an individual linear elastic element and thereafter assembling of all elements, the equilibrium equation can be written as

$$M\ddot{\boldsymbol{u}} + C\dot{\boldsymbol{u}} + K\boldsymbol{u} = \boldsymbol{f} \tag{7}$$

where $M = \sum_e M^e_{ab}$ is the mass matrix, $C = \alpha_0 M + \alpha_1 K$ is the Rayleigh damping coefficient, $K = \sum_e K^e_{ab}$ is the stiffness matrix, $\boldsymbol{f} = \sum_e \boldsymbol{f}^e_a$ is the external force, and $\dot{\boldsymbol{u}}$ is the velocity vector.

In discrete-time finite element methods, the transient solution for the studied time duration is described with a set of discrete time points t_k and approximations to the solution are determined at these points. One of the commonly used methods is the Newmark constant acceleration method [12], which is a one-step procedure to describe how a known solution at time t_{k-1} is determined at time t_k. Since the three discrete quantities $\boldsymbol{a}_k$, $\boldsymbol{v}_k$, and $\boldsymbol{u}_k$ that are the acceleration, the velocity, and the displacement vectors, respectively, are involved in Eq. (7), it requires three independent time equations to obtain a solution at each discrete time point. One is the equilibrium equation, and the other two are the Newmark formulas, Eqs (8) and (9). These are written as

$$\boldsymbol{u}_k = \boldsymbol{u}_{k-1} + \Delta t \boldsymbol{v}_{k-1} + \Delta t^2 (\boldsymbol{a}_{k-1} + \boldsymbol{a}_k)/4 \tag{8}$$

$$\boldsymbol{v}_k = \boldsymbol{v}_{k-1} + \Delta t (\boldsymbol{a}_{k-1} + \boldsymbol{a}_k)/2 \tag{9}$$

$$\boldsymbol{f}_k - M\boldsymbol{a}_{\boldsymbol{k}} - C\boldsymbol{v}_{\boldsymbol{k}} - K\boldsymbol{u}_{\boldsymbol{k}} = 0 \tag{10}$$

where $\Delta t = t_k - t_{k-1}$ and the equilibrium equation must be satisfied at each time point t_k.

Equation (10) is commonly solved by numerical algorithms, such as refined Gaussian elimination and Gauss-Seidel iterative schemes. The numerical solution is computationally expensive due to the iterative process. Therefore, numerical algorithms are not suitable to solve the above equations for the real-time requirement of soft tissue deformation. Further, numerical algorithms may also develop oscillations unless certain precautions are taken.

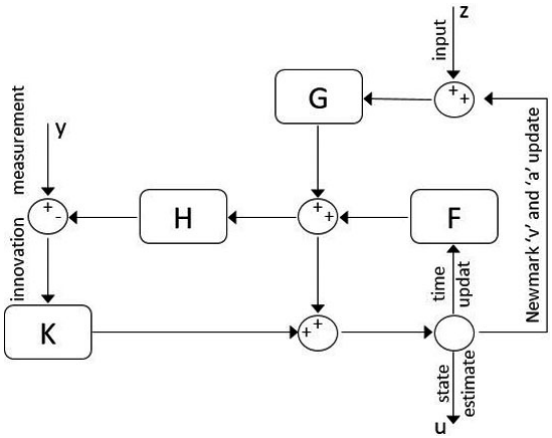

Fig. 1. Discrete-time KF-FEM block diagram.

In comparison with numerical algorithms, the Kalman filter uses a straightforward formulation for state space solution rather than an iterative process, leading to enhanced computational speed. Moreover, this recursive filtering method uses only the last time step estimation to compare with real-time measurements and optimize the next step estimation. By considering Eq. (10) as the system equation of the Kalman filter and solving it based on a set of measurements, it will result in a computationally fast and accurate solution.

2.3. KF-FEM algorithm

To solve Eq. (10) we can select any one of the discrete-time quantities $\boldsymbol{a}_k$, $\boldsymbol{v}_k$ and $\boldsymbol{u}_k$ as the main time-dependent variable and solve for the other two from the Newmark formulas. Without loss of generality, let us consider $\boldsymbol{u}_k$ as the primary variable and calculate velocity and acceleration using the Newmark formulas. By substituting velocity and acceleration vectors into the equilibrium Eq. (10) and reordering the equation into the form of Kalman state equation, we will have

$$\boldsymbol{u}_k = \left[J^{-1}A\right]\boldsymbol{u}_{k-1} + \left[J^{-1}L \;\; J^{-1}M \;\; J^{-1}I\right]\begin{bmatrix}\boldsymbol{v}_{k-1}\\ \boldsymbol{a}_{k-1}\\ \boldsymbol{f}_k\end{bmatrix} \tag{11}$$

where

$$A = 4M/\Delta t^2 + 2C/\Delta t \tag{12}$$

$$J = A + K \tag{13}$$

$$L = 4M/\Delta t + C \tag{14}$$

Note that input vector at each time point t_k will be a function of velocity and acceleration calculated from previous time point t_{k-1}, and a known external force at the current time. Figure 1 illustrates the block diagram of the proposed algorithm.

3. Performance evaluation and discussion

Simulations were conducted on a cubic model to evaluate performance of the proposed method. The

Table 1
Mesh specifications and test setting

Size of the model	No. of nodes	No. of elements	Analysis time	Time increments
$4 \times 4 \times 7$ (mm)	200	672	$t = 1$ (s)	$\Delta t = 0.002$ (s)
Applied force	Rayleigh coefficients	Density	Poisson's ratio	Young's modulus
$f = 3$ (kN/m^2)	$\alpha_0 = 0.0, \alpha_1 = 0.1$	$\rho = 1068$ (kg/m^3)	$\nu = 0.47$	$E = 10$ (kPa)

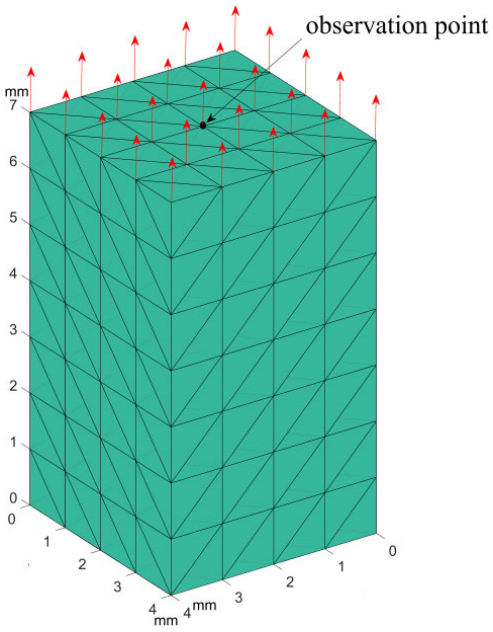

Fig. 2. Finite element verification model.

model is subject to uniform distributed stretch applied on the top surface. The measurement was obtained from deformation results at the observation point by traditional FEM with added random noise. The estimates of the proposed KF-FEM are compared with the results obtained from traditional FEM.

1st order tetrahedral elements with linear shape functions having 1 mm length per edge are used to uniformly discretize the domain. The mesh specifications and the analysis settings are shown in Table 1. It is considered that nodes on the bottom surface are fixed, and all nodes on the top surface are under a constant uniform axial tensile force selected within the interaction force range of soft tissues [13,14]. The tissue density, Poisson's ratio, and Young's modulus are derived from the experimental tests on the porcine liver [15,16]. Figure 2 shows the sample domain, from which the measurement matrix for displacement of the observation point was obtained.

Material, damping, and stiffness matrices are formed for the body domain. Then the finite element direct solver Gauss Elimination is employed to observe the behavior of the model under the described boundary conditions. In practice, measurements involve noise. Accordingly, we added random white Gaussian noise to the displacement values obtained from the traditional FEM modeling. Figure 3 shows the noisy measurement, which is the displacement of the observation point specified in Fig. 2. Artificial noise was added to the displacement obtained from the FEM rather than using real experimental noisy displacements in order to compare estimates of the proposed KF-FEM with known reference values, i.e. the displacement from the traditional FEM without noise. Two points out of the fixed points were

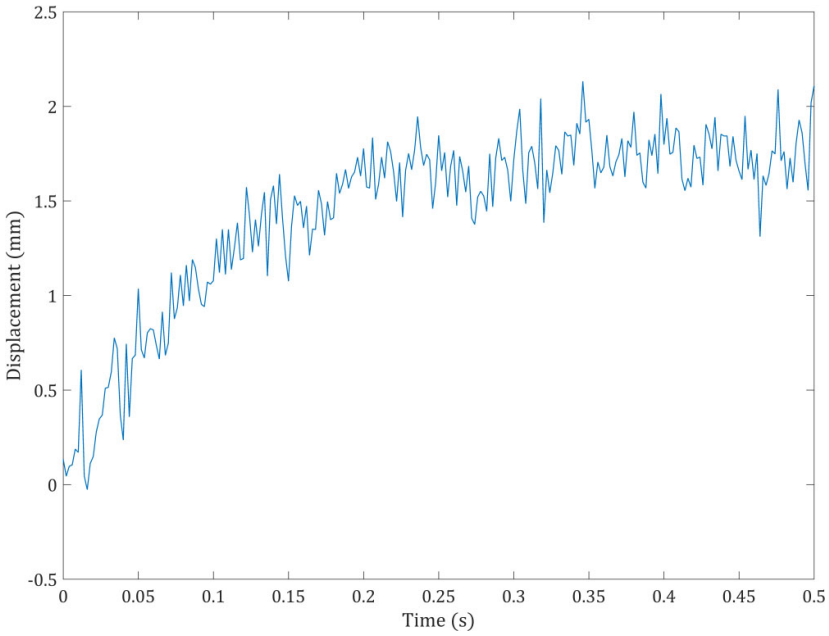

Fig. 3. Artificial noisy measurement for KF-FEM.

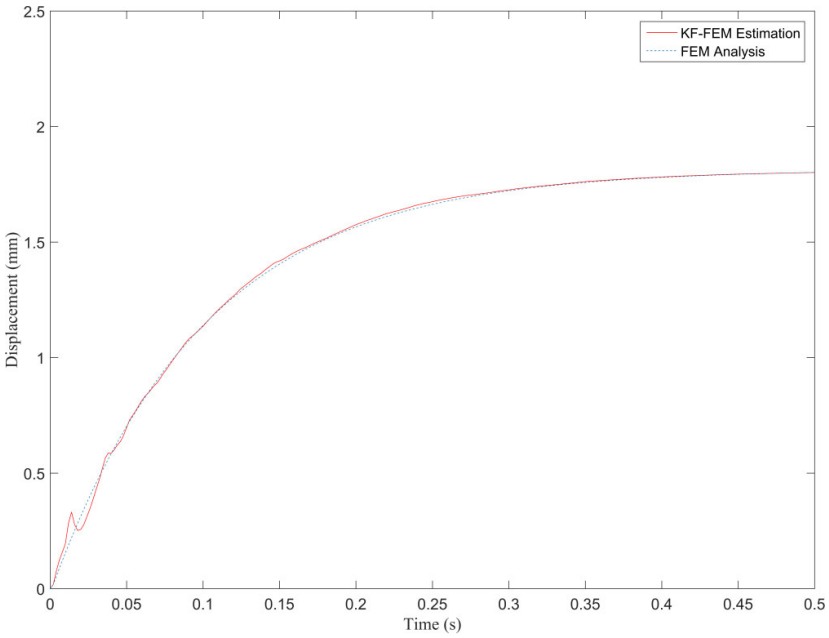

Fig. 4. Displacement obtained from FEM and KF-FEM at evaluation point 1.

selected to evaluate the estimation. One is the observation point (evaluation point 1), and the other is a random point (evaluation point 2). The random point was located 2 mm underneath the surface. System and measurement equations were initialized and measurement noise covariance was considered to have the intensity of 0.001.

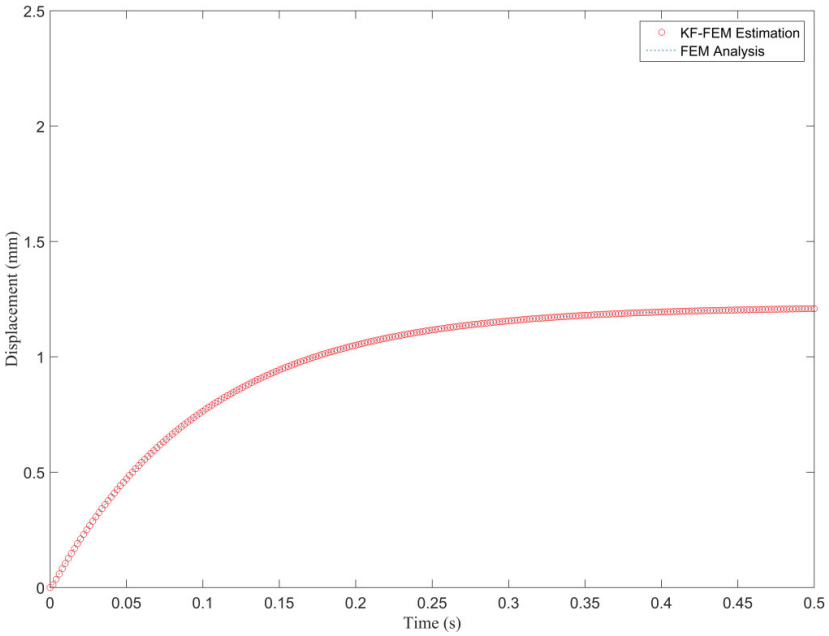

Fig. 5. Displacement obtained from FEM and KF-FEM at evaluation point 2.

The proposed algorithm was implemented in MATLAB R2014b on a PC with Intel® Core™ i7-2600 CPU @ 3.40 GHz, RAM 8.00 GB and 64-bit Windows 7. Two kinds of simulations were conducted under the same conditions for the cubic model. The first simulation was conducted to observe the deformation behaviors from the traditional FEM, and the second simulation was conducted to observe the deformation behaviors of the proposed KF-FEM. Subsequently, the results from the two simulations were compared in terms of accuracy and computational efficiency. Figures 4 and 5 compare the results of both traditional FEM and KF-FEM at different evaluation points.

Although the measurement was collected from one node (i.e. the observation point), the system was still able to estimate the deformation behaviors of all other nodes. This is because material matrices M, C and K were obtained from a finite element model, and the Kalman state vector was the displacement vector of all nodes in three coordinate directions. Further, the proposed method not only uses measurements to optimize the state estimates in the time domain, but it also conducts estimations in the spatial domain.

Figure 4 illustrates that the proposed method completely filters the measurement noise at the observation point and its estimation is in good agreement with the FEM response. The Kalman filter is a recursive optimal estimation method that only uses the Kalman gain obtained from the last time point for posterior estimation. This leads to estimations being more reliable after several time points based on the precision of the primary knowledge of the system and measurement noises. In Fig. 4, the uncertainty of the estimations can be seen in the first 25 steps from the total 500, i.e. in the first 0.05 seconds of deformation. The resultant NRMSE (normalized root-mean-square error) at the observation point between the traditional FEM and proposed KF-FEM is 0.0116. Furthermore, Fig. 5 shows that the KF-FEM estimates accurately follow the traditional FEM response at any other point except for the observation point with noisy measurements. To compare the computational performance of both methods, we computed the whole simulation time divided by the number of time steps. The computational time of each time step was 0.1735 s for traditional FEM, while it was only 0.0158 s for the proposed KF-FEM. In other words,

the computational time of the KF-FEM is approximately 10 times faster than traditional FEM. This is because the proposed method uses a statistical estimation process to estimate soft tissue deformation. In contrast, traditional FEM uses a numerical process, which requires the calculation of the inversion of material matrices at each time step, leading to an expensive computational load for soft tissue deformation. The computed calculation frequency of about 63 Hz from the proposed KF-FEM confirms the real-time performance of the described methodology.

4. Conclusion

This paper presents a new method for real-time prediction and analysis of soft tissue deformation. It conducts soft tissue deformation with a filtering process to estimate mechanical behaviors of soft tissue in real time based on measurement data. Simulation results demonstrate that the proposed method is as accurate as the traditional finite element method in terms of soft tissue deformation, but with the capability to achieve real-time computational performance. It can also eliminate unavoidable noises involved in system state and measurement.

The proposed method considers the linear elastic behavior of the tissue and it can deal with only small deformations of soft tissues. It is expected that in the future a nonlinear Kalman filter will be developed to deal with the nonlinear behaviors of soft tissues. Also, modifications to the filtering algorithm are in progress for simultaneous estimation of the system input that is the unknown deformation of the computational domain, and the state vector, i.e. the applied external force given real-time measurement from a haptic device.

Conflict of interest

None to report.

References

[1] Niroomandi S, Alfaro I, Cueto E, Chinesta F. Accounting for large deformations in real-time simulations of soft tissues based on reduced-order models. Computer Methods and Programs in Biomedicine 2012; 105(1): 1-12.
[2] Zhong Y, Shirinzadeh B, Smith J, Gu C. Soft tissue deformation with reaction-diffusion process for surgery simulation. Journal of Visual Languages & Computing 2012; 23(1): 1-12.
[3] Freutel M, Schmidt H, Dürselen L, Ignatius A, Galbusera F. Finite element modeling of soft tissues: Material models, tissue interaction and challenges. Clinical Biomechanics 2014; 363-72.
[4] Tadepalli SC, Erdemir A, Cavanagh PR. Comparison of hexahedral and tetrahedral elements in finite element analysis of the foot and footwear. J Biomech 2011; 44(12): 2337-43.
[5] Wen T, Tao RW. Constraint-based soft tissue simulation for virtual surgical training. Biomedical Engineering, IEEE Transactions on 2014; 61(11): 2698-706.
[6] Wu W, Chen H, Pheng AH. A computation model on real-time interactive soft tissue cutting and deformation. Jisuanji Fuzhu Sheji Yu Tuxingxue Xuebao/Journal of Computer-Aided Design and Computer Graphics 2010; 22(2): 185-90.
[7] Peterlík I, Sedef M, Basdogan C, Matyska L. Real-time visio-haptic interaction with static soft tissue models having geometric and material nonlinearity. Computers & Graphics 2010; 34(1): 43-54.
[8] Zwick B, Joldes GR, Wittek A, Miller K. Numerical algorithm for simulation of soft tissue swelling and shrinking in a total lagrangian explicit dynamics framework. Computational Biomechanics for Medicine: New Approaches and New Applications 2015; 37-46.
[9] Courtecuisse H, Allard J, Kerfriden P, Bordas SPA, Cotin S, Duriez C. Real-time simulation of contact and cutting of heterogeneous soft-tissues. Medical Image Analysis 2014; 18(2): 394-410.

[10] Kato Y, Kawahara M, Koizumi N. Kalman filter finite element method applied to dynamic ground motion. International Journal for Numerical and Analytical Methods in Geomechanics 2009; 33(9): 1135-51.
[11] Zeng N, Wang Z, Li Y, Du M, Liu X. A hybrid EKF and switching PSO algorithm for joint state and parameter estimation of lateral flow immunoassay models. IEEE-ACM Transactions on Computational Biology and Bioinformatics 2012; 9(2): 321-9.
[12] Zienkiewicz OCA, Taylor RL, Zhu JZ. The finite element method: Its basis and fundamentals. Seventh edition, Taylor RLA, Zhu JZA, editors, Elsevier, Butterworth-Heinemann 2013.
[13] van Gerwen DJ, Dankelman J, van den Dobbelsteen JJ. Needle-tissue interaction forces – a survey of experimental data. Medical Engineering and Physics 2012; 34(6): 665-80.
[14] Wang W, Shi Y, Goldenberg AA, Yuan X, Zhang P, He L, et al. Experimental analysis of robot-assisted needle insertion into porcine liver. Bio-Medical Materials and Engineering 2015; 26: S375-S80.
[15] Chui C, Kobayashi E, Chen X, Hisada T, Sakuma I. Combined compression and elongation experiments and non-linear modelling of liver tissue for surgical simulation. Medical and Biological Engineering and Computing 2004; 42(6): 787-98.
[16] Samur E, Sedef M, Basdogan C, Avtan L, Duzgun O. A robotic indenter for minimally invasive measurement and characterization of soft tissue response. Medical Image Analysis 2007; 11(4): 361-73.

Appendix C

13th International Conference on the Mechanical Behaviour of Materials (ICM13), 11-14 June 2019, Melbourne, Australia

Soft Tissue Behaviour Estimation in Small Deformations

M. Yarahmadian[1*], P. Dabnichki[1] and T.Y. Pang[1]

[1] *School of Engineering, RMIT University, Melbourne, Australia*

[*] *Corresponding author. Email: mehran.yarahmadian@gmail.com*

Abstract: The core of a medical simulator in applications such as diagnosis and palpation simulation rely on the realistic mechanical modelling of the manipulated soft tissue. The traditional Finite Element Method is the most accurate physical approach to simulate soft tissue behaviour but suffers from extended computational time due to the complexity of the tissue models. This paper presents a novel computational method that employs the computationally fast Kalman filter to speeding up the traditional FEM without sacrificing its accuracy. The Newmark-β temporal discretization method is used to formulate the FE equilibrium equation in state-space representation. Given the real-time displacement measurements from the manipulated tissue, the proposed KF-FEM was able to estimate the system state variable, i.e. displacement, in near real-time performance as perceived by humans. Simulations of the indentation operation on a pig liver shows that the proposed method achieves a response frequency of more than 25 Hz. In addition, it is demonstrated that the proposed method was able to filter more than 90% of the noise in the displacement measurements. It is concluded that the proposed KF-FEM utilizes the strength of the traditional FEM in terms of accuracy and achieves a real-time computational performance by incorporating direct measurements from the manipulated tissue. Furthermore, adoption of the Kalman filter allows to optimally reduce the noise level involved in measurements. The method allows to achieve highly accurate tissue response model in real-time loading.

Keywords: finite element method, Kalman filter, real-time estimation, small deformation and soft tissue behaviour.

1 Introduction

Realistic mechanical modelling of soft tissues has gained greater significance with the development of new medical systems such as medical training simulators. Although substantial research efforts have been dedicated to the mechanical modelling of soft tissues behaviour, a realistic simulation of soft tissues deformation remains a big challenge. A realistic and interactive training simulator not only requires the efficiency of computations without sacrificing the accuracy, but also must be adaptive to real world scenario [1], hence the model must be able to correct itself with the help of real-time measurements. The existing methods for modelling of soft tissue deformations are a trade-off between the real-time performance and the reliability of the model responses. Methods such as the finite element method (FEM) and the boundary element method model the mechanical behaviour of soft tissues accurately based on continuum mechanics [2,3], but they are either slow in terms of computation or fundamental solutions do not always exist in explicit form. Simpler and faster methods such as mass-spring and meshless models are fast [4,5], but exhibit reduced accuracy as they do not account realistically for the material properties.

The Kalman filter (KF) as an optimal estimator infers parameters of interest from indirect, inaccurate, and uncertain observations and minimises the mean square error of the estimated parameters. Its fast and recursive approach has made it popular for online real-time applications as measurements can be processed as they arrive without the need for measurement equations to be inverted. The Kalman filter does not only reduce the data noise, but it also projects the measurements onto the state estimate. The KF method has been used in a variety of applications. Zeng et al. developed a combination of KF and an optimization method to estimate the state parameters of lateral flow immunoassay [6] while Delalleau et al. used it to identify the material properties of the human skin [7].

A variety of strategies has been developed to improve the computational performance of the FEM as the most promising approach to the soft tissue deformation modelling. Zwick et al. employed an explicit approach to eliminate the iterative process for large systems [8], although the stability of the explicit solutions remained conditional. The graphics processing unit acceleration technique has also been employed by researchers to enhance the computational performance of the FEM [9,10]. However, this approach is strongly hardware dependent requiring substantive computational power.

In this work, a KF-FEM algorithm is demonstrated to estimate deformations due to applied surface loads with high accuracy when compared to the artificially simulated reference FE model [11]. The computational speed of the developed algorithm was around 11 times faster than the traditional FEM under the same boundary and loading condition. Besides, the developed KF-FEM algorithm was modified to incorporate noisy indentation measurements. The indentation test was repeated several times on a phantom tissue made from silicone rubber and the deviation of the developed FE model from the observations was considered as the error of the system.

2 Methods

The Kalman requires a state model that describes the transformation of the state vector over time, and an observation model that represents the relationship between the state vector and the measurements. The state model and the observation model in a discrete time system are given in (1) and (2) respectively.

$$\boldsymbol{x}_{k+1} = F\boldsymbol{x}_k + G\boldsymbol{z}_k + w_k \tag{1}$$

$$\boldsymbol{y}_k = H\boldsymbol{x}_k + v_k \tag{2}$$

where $\boldsymbol{x}_k$ is the state vector; F its transition matrix; $\boldsymbol{z}_k$ is the system input with G its control matrix; $\boldsymbol{y}_k$ is the set of measurements and H the measurement matrix; w_k and v_k are model and measurement noises with known covariances Q and R respectively.

The Kalman filter estimates the parameters of interest, i.e. the state vector, in a two-step procedure. In the first step it predicts *a priori* value of the state using equation (1), without considering w_k that is the uncertainty of the model. Then the covariance of the model uncertainty, i.e. Q, is used to calculate the corresponding covariance of the prediction in this step. By using equation (2) in the second step the system corrects its prediction with the arrival of measurements and calculates *a posteriori* value of the state vector so that the error covariance of the estimates is minimised. This procedure is repeated for each time step. Figure 1 illustrates two steps of the Kalman filter algorithm.

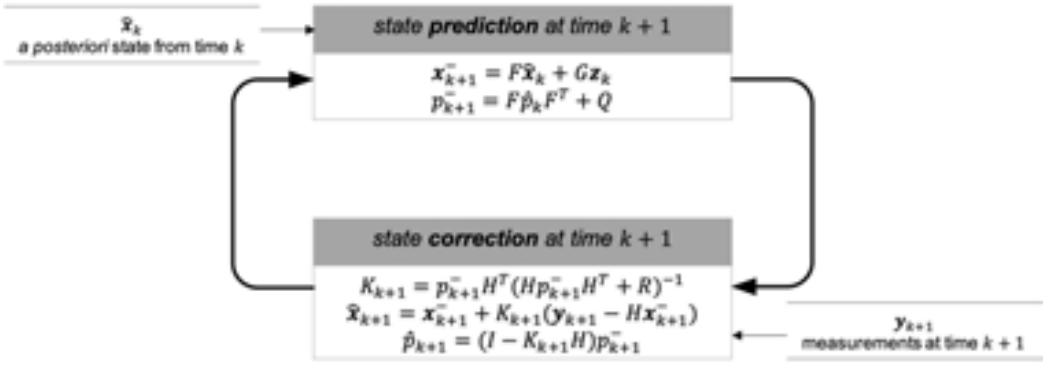

Figure 1: The Kalman filter algorithm

The errors' covariance in the mentioned two-step algorithm is represented by p_k at each time step, and K_k is the Kalman gain which defines either measurements or the model estimates are more reliable.

In the small deformations range within a short period of time, soft tissues behavior can be modelled with a linear elastic constitutive model [2]. The body domain of the tissue requires to be discretized into finite number of elements that are connected via nodes. The Hooke's law applies to individual elements as well as the body domain. The equilibrium equation in the global formulation can be written as:

$$M\ddot{\boldsymbol{u}} + K\boldsymbol{u} = \boldsymbol{f} \tag{3}$$

where $\boldsymbol{u}$ is the nodal displacement, $\ddot{\boldsymbol{u}}$ is the nodal acceleration, $\boldsymbol{f}$ is the external load, M and K are the global mass and stiffness matrices respectively.

To simulate the deformation of the soft tissue under the external load, the nodal displacement of the whole geometrical domain is selected as the state vector, and the applied external load is the input for the set of Kalman filter system equations. To formulate the equilibrium equation (3) in the form of the Kalman filter model equation (1) a temporal transient solution is required to split the time period of interest into discrete time points t_k which state estimates can be determined at these time points. The

Newmark constant acceleration method is one of the effective approaches that describes how a known solution at time step t_k is determined at time step t_{k+1} [12]. Two independent and first order derivative estimates of the Newmark method are:

$$\boldsymbol{u}_{k+1} = \boldsymbol{u}_k + \Delta t\dot{\boldsymbol{u}}_k + \Delta t^2(\ddot{\boldsymbol{u}}_{k+1} + \ddot{\boldsymbol{u}}_k)/4 \quad (4)$$

$$\dot{\boldsymbol{u}}_{k+1} = \dot{\boldsymbol{u}}_k + \Delta t(\ddot{\boldsymbol{u}}_{k+1} + \ddot{\boldsymbol{u}}_k)/2 \quad (5)$$

where $\boldsymbol{u}$ is the nodal displacement and $\dot{\boldsymbol{u}}$ the nodal velocity and Δt is the sampling time step. By considering the displacement vector as the independent variable and calculating the velocity and acceleration from equations (4) and (5); then replacing $\ddot{\boldsymbol{u}}$ in (3) with the acceleration obtained from the Newmark formulas; the nodal displacement formula can be written as following:

$$\boldsymbol{u}_{k+1} = (J^{-1}.4M/\Delta t^2)\boldsymbol{u}_k + (J^{-1}.4M/\Delta t)\dot{\boldsymbol{u}}_k + (J^{-1}.M)\ddot{\boldsymbol{u}}_k + J^{-1}\boldsymbol{f}_{k+1} \quad (6)$$

where $J = 4M/\Delta t^2 + K$. By comparing the equilibrium equation (6) with the Kalman filter state model (1), the system parameters are defined as; the state vector $\boldsymbol{x}_k \equiv \boldsymbol{u}_k$, the transition matrix $F \equiv J^{-1}.4M/\Delta t^2$, the control matrix $G \equiv [J^{-1}.4M/\Delta t \quad J^{-1}.M \quad J^{-1}]$, and the input vector $\boldsymbol{z}_k \equiv [\dot{\boldsymbol{u}}_k \quad \ddot{\boldsymbol{u}}_k \quad \boldsymbol{f}_{k+1}]^T$. From the defined input vector, it must be noted that the system's input at each time step is a block vector of the external force at the current time point and the nodal velocity and acceleration vectors from the previous time points.

3 Experimental Validation

The developed KF-FEM model was verified [11] with artificially generated data only, assuming that the foundation FE model was 100% accurate. In the other word, the model error covariance Q was considered zero. In practice, due to the complexity of the soft tissue, the model involves error as well as the experimental observations. The novelty of combining the optimal estimator, i.e. Kalman filter, with the traditional FE model is that the developed algorithm balances the uncertainty of the model as well as the measurements.

Figure 2: Experiments setup for the indentation of the phantom tissue

Experiments were conducted to evaluate the performance of the proposed method. Indentation tests were conducted on a phantom tissue using the TMA-Q400 machine in the room temperature. The phantom tissue is made up of silicone rubbers which have similar characteristics of human soft tissues [13]. Six cubic shape samples ($10 \times 10 \times 5\ mm$) were prepared to fit into the test machine. The density of samples was computed 1068 kg/m^3 by average. As shown in Figure 2, a frictionless rigid circular flat-end probe with 2.85 mm diameter was used to indent the tissue vertically. The loading condition was similar to the literature [14], where an indentation force is applied to the centre of the tissue's surface with a linear increase from 0.01 N to 0.4 N. Displacements were collected from the samples and are shown in Figure 3.

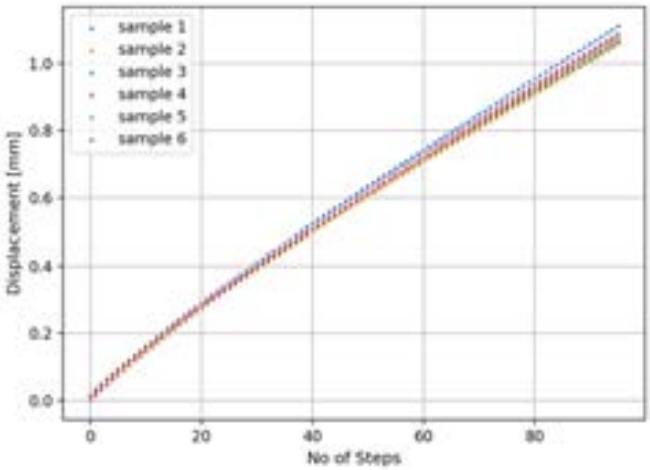

Figure 3: Real time displacements from the 6 phantom tissues indentation

A FEM model of a cube with the same size as the samples was created in MATLAB R2015b. The model was discretised into 4941 tetrahedral elements with 1123 mesh nodes. The nodes in contact with the probe were identified according to the probe's tip location and its diameter. The share of the applied force at each time step was determined according to the number of elements involved. To compute the model uncertainty, the traditional FEM was conducted under the same condition as the experiments, then the error of measured displacements compared to the FEM response was taken as the model error, i.e. Q. The measured displacements were taken as noisy measurements with known error covariance computed from the errors of 6 samples, i.e. R. The developed KF-FEM algorithm was run as explained in Figure 1 in 96 time-steps to solve the equilibrium equation (6). A comparison between the developed KF-FEM estimates and the traditional FEM computed displacement at two different nodes are illustrated in Figure 4.

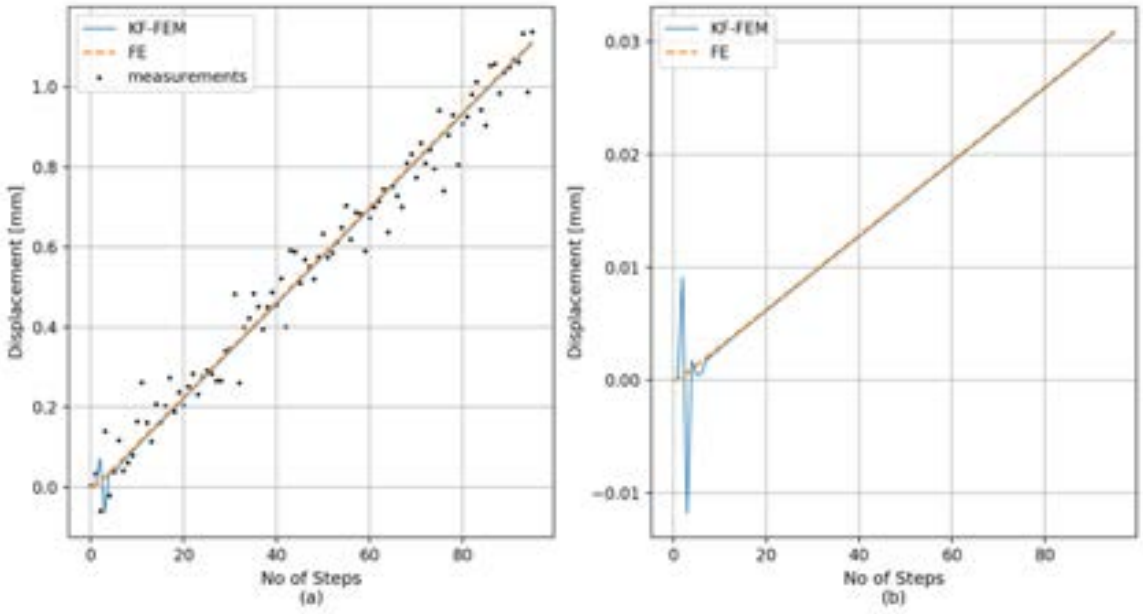

Figure 4: Comparison of the FE and the KF-FEM estimates; (a) at indenter's tip (b) at a random node

As can be seen in Figure 4, the KF-FEM estimates are in good agreement with the FE analysis. At the indenter's tip where the measurements are available (Figure 4(a)), the uncertainty of the system predictions is balanced, hence, smaller fluctuations are observed in estimates compared to the other nodes that there is no access to measure the displacement (Figure 4(b)). It must be noted that the measurement values illustrated in Figure 4(a) are obtained from the least square fit to the observed displacement from the six samples with the computed error. The convergence of the KF-FEM estimates with the FE analysis happens at the time step where the estimation error covariance of the developed

KF-FEM converges towards zero. The root mean squared error of both methods as well as the least square fit to the observed displacement at the indenter's tip of six samples is presented in Table 1.

Table 1: Comparing the RMSE [mm] between methods and samples at indenter's tip

	sample 1	sample 2	sample 3	sample 4	sample 5	sample 6	**Avg. error**
LSTSQR	0.042	0.021	0.027	0.024	0.036	0.025	2.92%
FEM	0.049	0.037	0.041	0.034	0.045	0.039	4.08%
KF-FEM	0.054	0.041	0.045	0.039	0.050	0.044	4.55%

It can be seen from Table 1 that the proposed method shows slightly larger error by average compared to experimental samples. In a system with known model error (Q) and measurement error (R), this value highly depends on the initialization of the algorithm, i.e. $\boldsymbol{u}_0$ the initial state vector and $\hat{p}_0$ the initial estimation error covariance. It means that the more confident about the initial state of the system and the model error, the smaller error in estimates compared to experiments as well as the reference FE model. Due to its one-step recursive algorithm, the developed KF-FEM increases the computational speed significantly. The traditional FE analysis took 36.2 seconds to compute the displacements in 96 time-steps, but the KF-FEM method took only 659 milliseconds to complete the computation under the identical boundary conditions. Update frequency of both methods is presented in Table 2.

Table 2: Computational speed of the KF-FEM and the FEM

	FEM	**KF-FEM**
Computation time [s]	36.2	0.659
Frequency [Hz]	2.7	145.7

It should be noted that while the measurements are only available at certain points of the geometrical domain, the proposed method is able to get advantage of partial observations as well as the model and expand the estimates in the spatial domain. It is also able to achieve the computational frequencies of higher than 25 Hz, proven its ability to be employed in real-time applications. The geometrical model estimated deformation by the KF-FEM is illustrated in Figure 5.

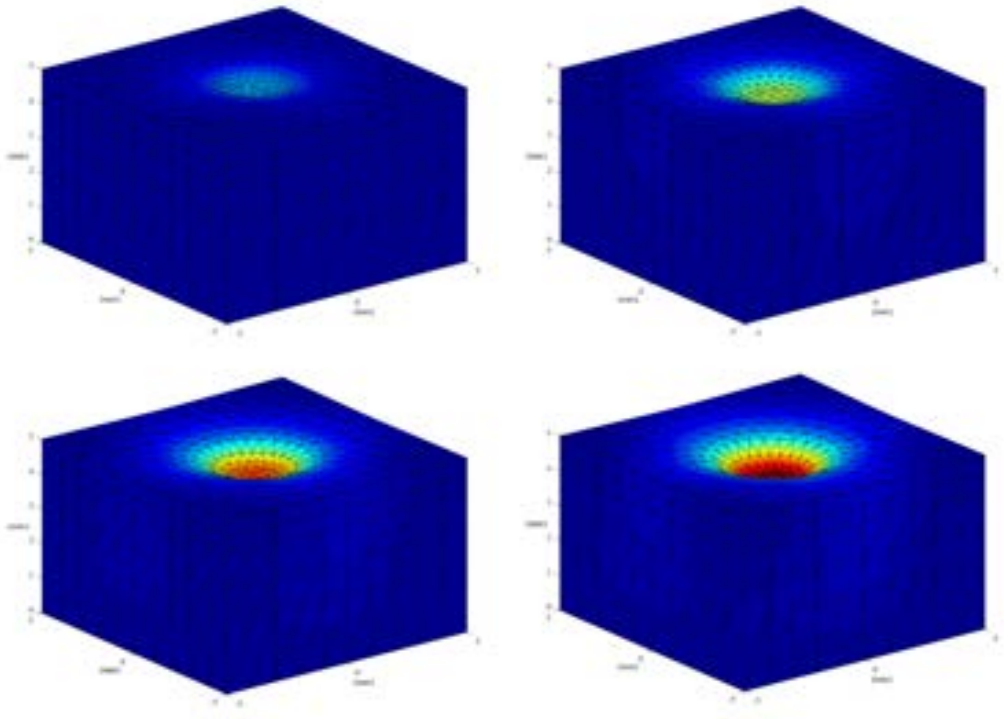

Figure 5: The deformed phantom tissue estimated by KF-FEM

4 Conclusions

The proposed KF-FEM method is validated through a set of experiments on silicone phantom tissue. The simulation results confirm that the developed algorithm achieves high frequency update rate by adopting the recursive process of the Kalman filter. It is also demonstrated that the developed algorithm achieves high accuracy through the associated FEM-based state equation. The proposed novel approach gets advantage of direct measurements available only at some geometrical points of the state vector and extends the estimates in the whole domain through the meshes.

Further work will focus on the recognition of the system noise compared to the experiments. Updating the initial system noise according to the behaviour of the soft tissue during the deformation can result in smaller error in estimates by improving the model priori estimates. In addition, a nonlinear spatio-temporal algorithm is being developed by our research group to correspond to the nonlinearity of the soft tissue in large deformations.

References

[1] S. Niroomandi, I. Alfaro, E. Cueto, F. Chinesta, Real-time deformable models of non-linear tissues by model reduction techniques, Comput. Meth. Programs Biomed. 91 (2008) 223–231. doi:10.1016/j.cmpb.2008.04.008.

[2] M. Freutel, H. Schmidt, L. Dürselen, A. Ignatius, F. Galbusera, Finite element modeling of soft tissues: Material models, tissue interaction and challenges, Clin. Biomech. (2014) 363–372. doi:10.1016/j.clinbiomech.2014.01.006.

[3] B. Zhu, L. Gu, A hybrid deformable model for real-time surgical simulation, Comput. Med. Imaging Graph. 36 (2012) 356–365. doi:http://dx.doi.org/10.1016/j.compmedimag.2012.03.001.

[4] G. San-Vicente, I. Aguinaga, J.T. Celigueta, Cubical Mass-Spring Model Design Based on a Tensile Deformation Test and Nonlinear Material Model, Vis. Comput. Graph. IEEE Trans. 18 (2012) 228–241. doi:10.1109/TVCG.2011.32.

[5] A. Horton, A. Wittek, G.R. Joldes, K. Miller, A meshless Total Lagrangian explicit dynamics algorithm for surgical simulation, Int. j. Numer. Method. Biomed. Eng. 26 (2010) 977–998. doi:10.1002/cnm.1374.

[6] N. Zeng, Z. Wang, Y. Li, M. Du, X. Liu, A Hybrid EKF and Switching PSO Algorithm for Joint State and Parameter Estimation of Lateral Flow Immunoassay Models, Ieee-Acm Trans. Comput. Biol. Bioinforma. 9 (2012) 321–329. doi:10.1109/tcbb.2011.140.

[7] A. Delalleau, G. Josse, J.M. Lagarde, H. Zahouani, J.M. Bergheau, Characterization of the mechanical properties of skin by inverse analysis combined with an extensometry test, Wear. 264 (2008) 405–410. doi:http://dx.doi.org/10.1016/j.wear.2006.08.033.

[8] B. Zwick, G.R. Joldes, A. Wittek, K. Miller, Numerical algorithm for simulation of soft tissue swelling and shrinking in a total lagrangian explicit dynamics framework, in: Comput. Biomech. Med. New Approaches New Appl., 2015: pp. 37–46. doi:10.1007/978-3-319-15503-6_4.

[9] H. Courtecuisse, H. Jung, J. Allard, C. Duriez, D.Y. Lee, S. Cotin, GPU-based real-time soft tissue deformation with cutting and haptic feedback, Prog Biophys Mol Biol. 103 (2010) 159–168. doi:10.1016/j.pbiomolbio.2010.09.016.

[10] Z.A. Taylor, M. Cheng, S. Ourselin, High-speed nonlinear finite element analysis for surgical simulation using graphics processing units, IEEE Trans. Med. Imaging. 27 (2008) 650–663. doi:10.1109/TMI.2007.913112.

[11] M. Yarahmadian, Y. Zhong, C. Gu, J. Shin, Soft tissue deformation estimation by spatio-temporal Kalman filter finite element method, Technol. Heal. Care. 26 (2018) 317–325. doi:10.3233/THC-174640.

[12] O.C. author Zienkiewicz, R.L. Taylor, J.Z. Zhu, The finite element method : its basis and fundamentals, Seventh ed, Elsevier, Butterworth-Heinemann, 2013.

[13] G. Lamouche, B.F. Kennedy, K.M. Kennedy, C.-E. Bisaillon, A. Curatolo, G. Campbell, V. Pazos, D.D. Sampson, Review of tissue simulating phantoms with controllable optical, mechanical and structural properties for use in optical coherence tomography, Biomed. Opt. Express. (2012). doi:10.1364/BOE.3.001381.

[14] Y.B. Fu, C.K. Chui, Modelling and simulation of porcine liver tissue indentation using finite element method and uniaxial stress-strain data, J. Biomech. 47 (2014) 2430–2435. doi:10.1016/j.jbiomech.2014.04.009.

DECEMBER 2019